

## **Chapter 2**

### **Results of Flight Scientific Programmes, Research and Observation Realized in 2016 – 2017**

#### **CONTENT**

1. Skobeltsyn Institute of Nuclear Physics of Lomonosov Moscow State University
2. Russian Academy of Sciences, Pushkov Institute of Terrestrial Magnetism, Ionosphere and Radio Wave Propagation
3. Russian Academy of Sciences, Lebedev Physical Institute
4. Russian Academy of Sciences, Keldysh Institute for Applied Mathematics

## Basic Space Projects Realized in 2016 - 2017

### 2.1. LOMONOSOV satellite - astrophysical observatory

(Skobeltsyn Institute of Nuclear Physics of Lomonosov Moscow State University)



The main objectives of the LOMONOSOV satellite experiments are the fundamental problems of astrophysics - the study of extreme physical phenomena in the atmosphere, near space and in the Universe, as well as the solution of important applied problems associated with the existence of potentially dangerous phenomena in near - earth space for both man and space and aviation technology.

#### *a. Ultra-High Energy Cosmic Rays (UHECR)*

Natural accelerators, which are not in our Galaxy, and beyond it create a stream of particles – UHECR(Ultra-High Energy Cosmic Rays) at energies of  $10^{19}$  eV and over. The power of such accelerators outside our Galaxy is incomparably greater than that of the particle accelerators that exist within our Galaxy.

However, back in 1966, immediately after the discovery of the "background cosmic relic radiation" with a temperature of about  $2.7^{\circ}\text{C}$ , which remained after the Big Bang that gave rise to the beginning of the existence of our Universe, in the works of the American scientist K. Greisen, and Soviet ones -G. Zatsepin (MSU' Professor)and V. Kuzmin - have been shown that at the energy of  $5 \cdot 10^{19}$  eV the energy spectrum of cosmic rays can be cut off due to the interaction of protons and cosmic ray nuclei with photons of "relic" radiation. Detection of such a "cut-off" of the spectrum would indicate that the sources of cosmic rays of such high energies are at cosmological distances  $\gg 100$  megaparsecs. Experimental confirmation or refutation of this theoretical prediction is of great importance to determine the nature of UHECR. Orbiting ultraviolet (UV) transients telescope TUS installed on board the LOMONOSOV satellite, became the world's first experiment to study UHECR from space.

*b. Transient luminous events in the atmosphere.*

Recent studies of ultraviolet transients (UV) in the upper atmosphere lead to the conclusion that this is a special kind of electrical discharges occurring between the clouds and the ionosphere, in which huge energy (sometimes up to hundreds of gigajoules) can be concentrated. This energy is released in the form of electromagnetic radiation with different frequencies from radio range to gamma radiation, relativistic electrons, and possibly neutron fluxes. The nature of this remarkable events is not fully understandable yet.

*c. Gamma-ray bursts.*

"Gamma-ray bursts" – the phenomenon of generation of short-term bursts of cosmic radiation in a wide frequency range - from ultraviolet to gamma-radiation – are one of the most mysterious phenomena of nature today. Despite clear progress in understanding this phenomenon, their study remains one of the priorities of modern astrophysics. This is due to the fact that there is still no complete clarity regarding the mechanisms of their generation in the source (as well as in the problem of cosmic rays of extremely high energies, the main thing here is the identification of the source-the accelerator that generates photons). The huge variation of photon flux estimation in the source-more than 6 orders, as well as the formation of a narrow cone of radiation in space, greatly complicates the solution of this problem.

For the first time, the LOMONOSOV satellite will conduct simultaneous observations of gamma-ray bursts in different ranges of the electromagnetic spectrum - in the visible, ultraviolet and gamma-ray ranges, using wide-field optical cameras and detectors of x-ray, ultraviolet and gamma-ray radiation. It should be noted that such complex experimental studies of this natural phenomenon will be conducted for the first time.

*d. Monitoring of potentially dangerous objects in space.*

The complex of instruments for studying GRBs at LOMONOSOV, along with the solution of an important fundamental problem of astrophysics, will also be aimed at solving the urgent problem of an applied nature – the creation of a system of global monitoring of potentially dangerous objects in outer space. For the first time wide - angle optical cameras SHOCK installed on board the LOMONOSOV satellite, developed at MSU, will become the basis of a system for tracking dangerous space objects in near-earth space, among which, of course, asteroids and large meteorites.

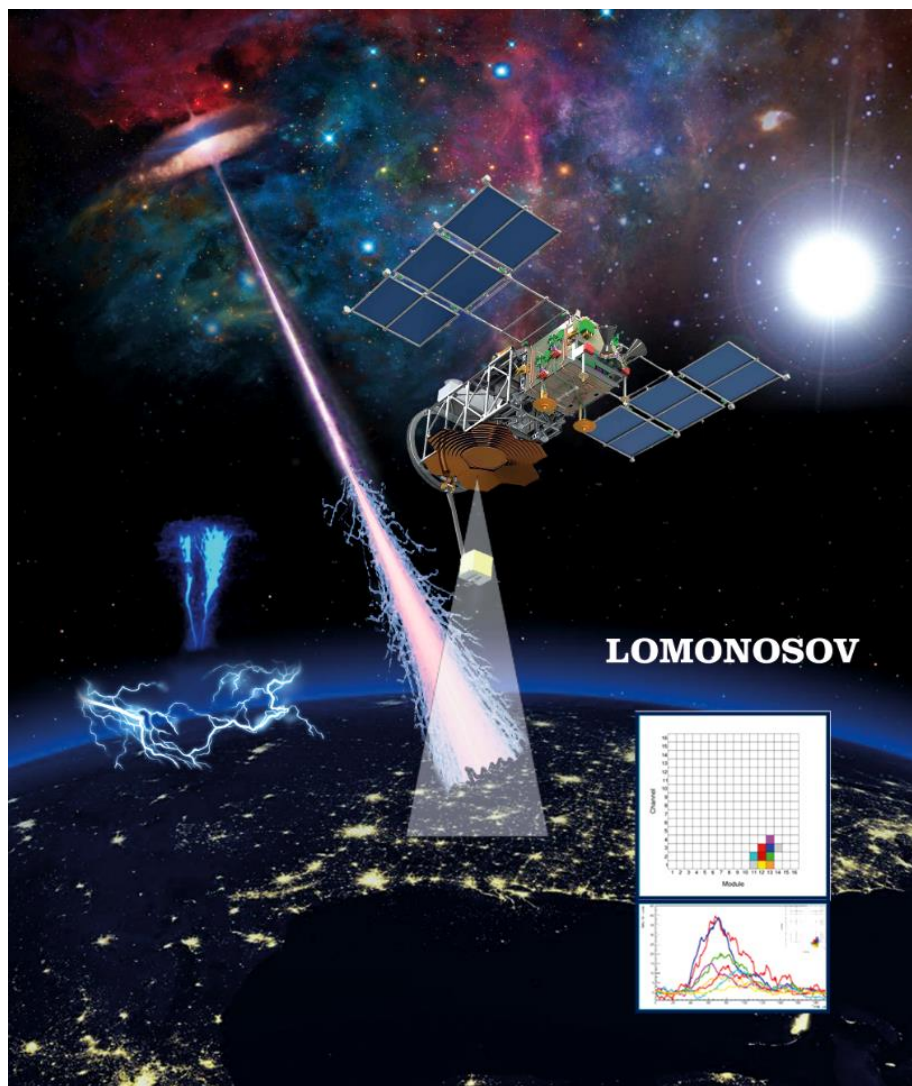
It should be noted that this system of observation of dangerous objects will be a space segment of global monitoring, including also the ground-based system of optical telescopes "Master" - analogues of SHOCK, also created at MSU and located both in Russia and abroad.

*e. Studies of the Earth's radiation environment.*

Within the frames of the LOMONOSOV project, it was decided to focus on studying mainly energetic radiation and, in particular, relativistic electrons. The

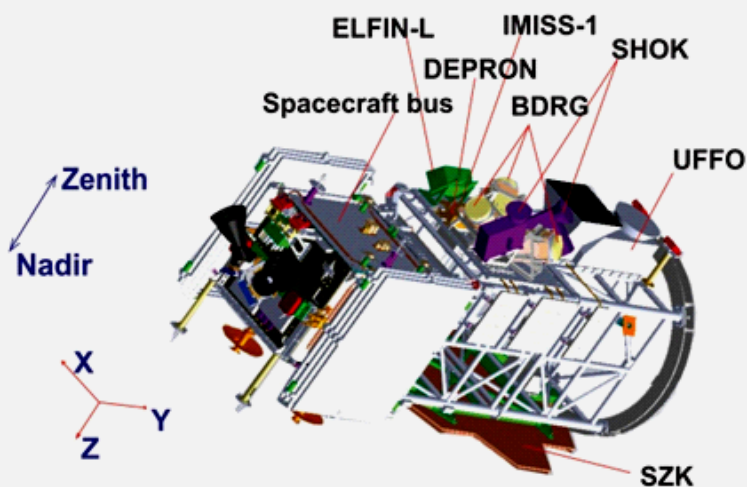
problem of generation of relativistic electrons continues to be relevant both from the fundamental point of view (sources, acceleration mechanisms) and from the applied point of view (prediction of the impact of these particles on the onboard electronics and spacecraft materials). In addition, there is another important aspect of this problem of near-earth space physics: their impact on the Earth's atmosphere, which is associated with the precipitation of particles from the geomagnetic trap – radiation belts. This phenomenon becomes central for the studies onboard the LOMONOSOV spacecraft. Radiation monitoring of the surrounding outer space from the LOMONOSOV satellite became a part of the international system of space radiation research and monitoring currently being established under the auspices of space agencies of different countries.

LOMONOSOV satellite was launched on April 28, 2016 from VOSTOCHNY COSMODROME.





## General configuration of the “Lomonosov” scientific complex.

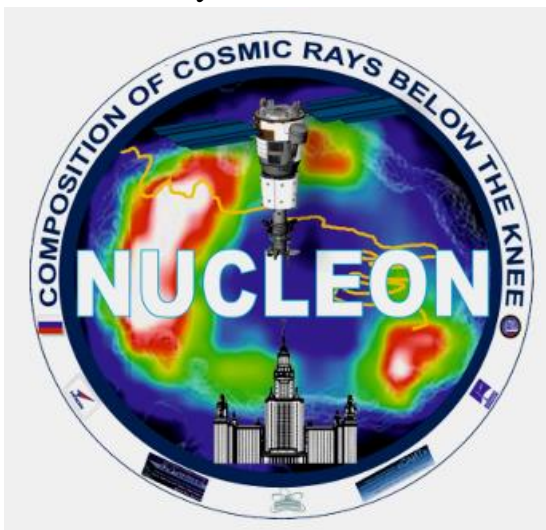


Technical characteristics of satellite

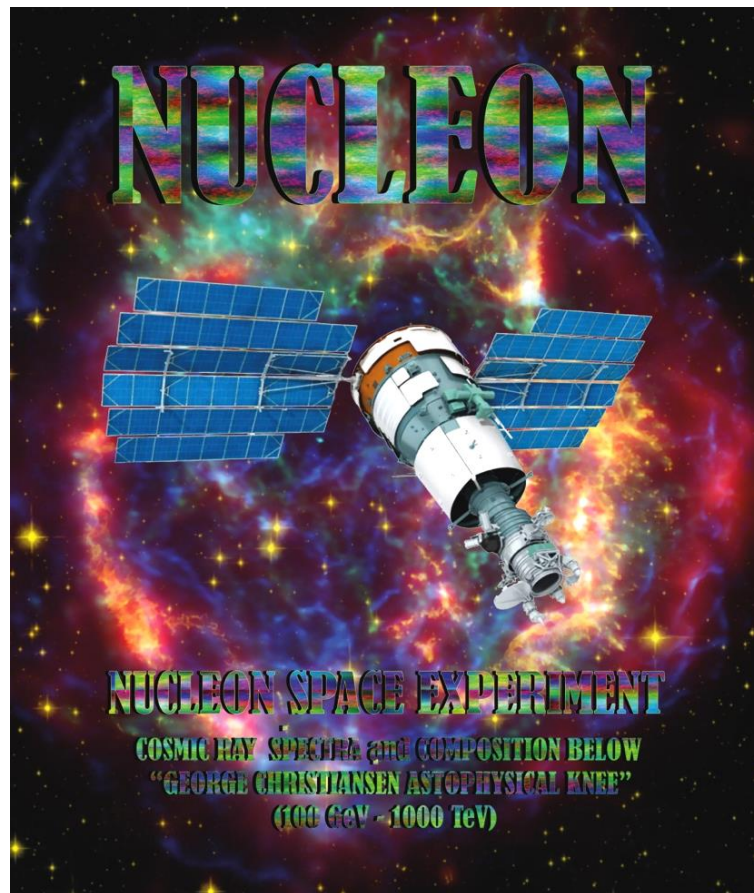
Platform mass , kg	250
Payload mass (TUS telescope , etc .), kg	150
Spacecraft mass , kg	400
Platform power consumption averaged during the orbit pass , W	200
Spacecraft power consumption averaged during the orbit pass , W	300
Scientific information traffic , Gbyte / day	Not more than 8

## 2.2. NUCLEON Space project

(Skobeltsyn Institute of Nuclear Physics of Lomonosov Moscow State University)






The NUCLEON instrument designed at MSU is a modern detector for the studies of the energy spectra and nuclear composition of cosmic rays at energy less than  $10^{15}$ eV generated within our Galaxy. Namely these parameters of Galactic cosmic rays(GCR) have the principal role in understanding their origin in our Universe. The project is aimed at solving the urgent problem of modern astrophysics - identification of the mechanism of acceleration of these particles. Among the most probable mechanisms of acceleration by a shock wave – the remnants of supernova explosions. The facility is based on the most modern technologies of nuclear radiation detectors and electronics.



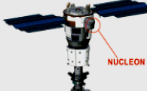
*Fig.3. NUCLEON space instrument onboard "RESOURS-P" satellite.*

NUCLEON was launched in December 2014 as a secondary payload on the spacecraft "RESOURS –P".

## NUCLEON

**apparatus as a monoblock inside of vessel, on regular serial Russian satellite "Resurs-P" N2**  
**Main addition payload parameters for NUCLEON:**



**Mass** ~300kg; in the pressurized container less than 300kg;  
**Energy consumption** ~ 180 W;  
**Daily telemetry volume** ~ 70 GB/bytes;  
**Number of independent sensors** ~1150;  
**Operational period** > 5 years.

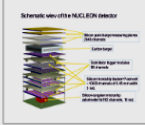
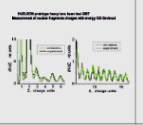
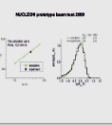
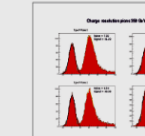
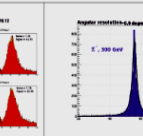
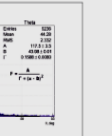
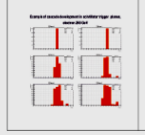
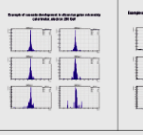
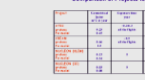
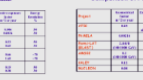
**Launching end 2013**

**Exposure Factor** in 60 days:  
 Protons KLEM ~ 140  
 Protons Calorimeter ~ 55  
 Nuclei Fe KLEM ~ 600  
 Nuclei Fe Calorimeter ~ 140  
 Electrons Calorimeter ~ 150

**Energy Resolution %:**  
 Protons KLEM 70-80  
 Protons Calorimeter ~30  
 Nuclei Fe KLEM 70-80  
 Nuclei Fe Calorimeter ~30  
 Electrons Calorimeter ~10

**Charge resolution**  $\sigma_{ch} < 0.2$   
 Protons rejection  $> 10^7$

### Beam tests results

Cosmic rays are one of the most important components of the visible part of the matter in the Universe, therefore studies of cosmic rays across the board is one of the fundamental problems of natural sciences. The basic parameters of cosmic rays are the particle type and kinetic energy. Based on these characteristics and taking into account astronomical data at all ranges along with present-day conceptions in the field of elementary particles the scientists develop models of the Galaxy and of the Universe as a whole, search exotic phenomena, which can provide experimental demonstration of the existence of dark matter particles, and discover strange matter particles.

The basic difficulty of the movement spread along the energy range during the direct studies of the cosmic rays components is extremely high expenses for the production of a spectrometer for measuring of the primary energy outside the atmosphere. Currently, the only method is the development of the universal spectrometer is a method of ionization calorimeter, developed by SNP scientists in 1950s. It is reliable and thoroughly studied method, but it has one significant drawback - need for a large amount of condensed matter. This requirement becomes critical concerning the mass limits for the space experiments on the studies of cosmic rays with energy  $> 10^7$  eV.

In order to continue the studies with minimum costs the basic conception of the NUCLEON experiment was determined as following: development of the scientific equipment of relatively small weight and size, which is able to solve currently important of the experimental physics of cosmic rays within wide energy range  $10^7 - 10^{10}$  eV. The approach does not need an individual center of the equipment. In order to expose the instrument it is possible to use supplementary reserves, which regularly appear onboard the Russian spacecrafts during the realization of the long-term target.

Innovative approach to the studies of high-energy cosmic rays KLEM (Kinematic Lightweight Energy Meter) is based on determination of the energy of the primary particles with respect to the spatial density of the secondary particles produced in the target during the first inelastic process and manifested in the long-range converter.

The radical departure of the suggested method from the ionization calorimeter in absence of the massive absorber material for the cascade propagation. It makes possible to develop scientific instruments with unique "apertures/mass" ratio.

**The scientific equipment consists of four basic systems (see Figure):**

- a system for measurements of the primary particle's charge (or deriving of its absence) - four layers of pad silicon detectors (1);
- the KLEM spectrometer - granite target (2) and six thin (~2 mm) layers of tungsten with a layer of microstrip (strip step is ~0.5 mm) silicon detectors above each of them (3);
- a scintillation system of fast trigger in order to separate an "interesting" event from the background - six layers of scintillator (4);
- a small long-range-ionization calorimeter (SIC) intended for in-flight calibration of the KLEM spectrometer and for separation of electromagnetic component (high-energy photons and electrons) from the cosmic rays - six layers of 6 mm thick tungsten with a layer of microstrip (strip step is 1.0 mm) silicon detectors above each of them (5).

**The basic characteristics of the scientific equipment:**

- configuration (geometric) factor is  $\sim 0.3$  sr (one for SIC is  $\sim 0.08$  sr);
- charge resolution is not less than 0.2 charge units;
- energy resolution is not less than 70% (in case of using with SIC is not less than 50%) for all types of nuclei;
- energy resolution of electromagnetic component is not less than 8-10%.

The declared characteristics were experimentally proved during the accelerator tests with SPN CERN extracted beams of hadrons, nuclei and electrons within energy range of 50-350 GeV and charge range of Z=1-30 (see Figures).

In spite of limited resources, such as mass, overall size, energy consumption, etc., the NUCLEON experiment will twice increase global statistics collected during the previous 50 years. Moreover, it will provide qualitatively new material for the first time cosmic rays will be studied within unprecedentedly wide energy range by means of uniform method during a long-term (not than 5 years) orbital experiment.

## 2.3. RELEC Space project on board the VERNOV satellite (Skobeltsyn Institute of Nuclear Physics of Lomonosov Moscow State University)



The project is aimed at solving fundamental and applied problems related to the impact of cosmic radiation – radiation belts relativistic electrons - on the Earth's atmosphere and ionosphere. Among the possible effects is the modification of the physical properties of the upper atmosphere and, as a consequence, the generation of both transient and long-term phenomena in the form of ultraviolet and red candles with significant energy release. Simultaneously, the companion explores the gamma radiation associated with the strengthening of the electric field during thunderstorm activity, and the measurement of electromagnetic waves in a wide frequency range, providing the precipitation of energetic particles from the radiation belts into the atmosphere. The satellite was launched on June 19, 2014.



## 2.4. Radiation monitoring in the near-Earth space

(Skobel'syn Institute of Nuclear Physics of Lomonosov Moscow State University)

Numerous instruments for measurements of plasma and energetic radiation have been developed in SSD. These instruments were designed for separate registration of charged particle fluxes in near-Earth space in the energy ranges:

0.05–20 Kev (electrons and protons), 0.15–10 MeV (electrons) and 2-150 MeV (protons). The particles of the first range are registered by means of an electrostatic analyzer, and the second – by a spectrometer of the vigorous radiation created on the basis of three semiconductor and scintillation detectors (Fig.4).



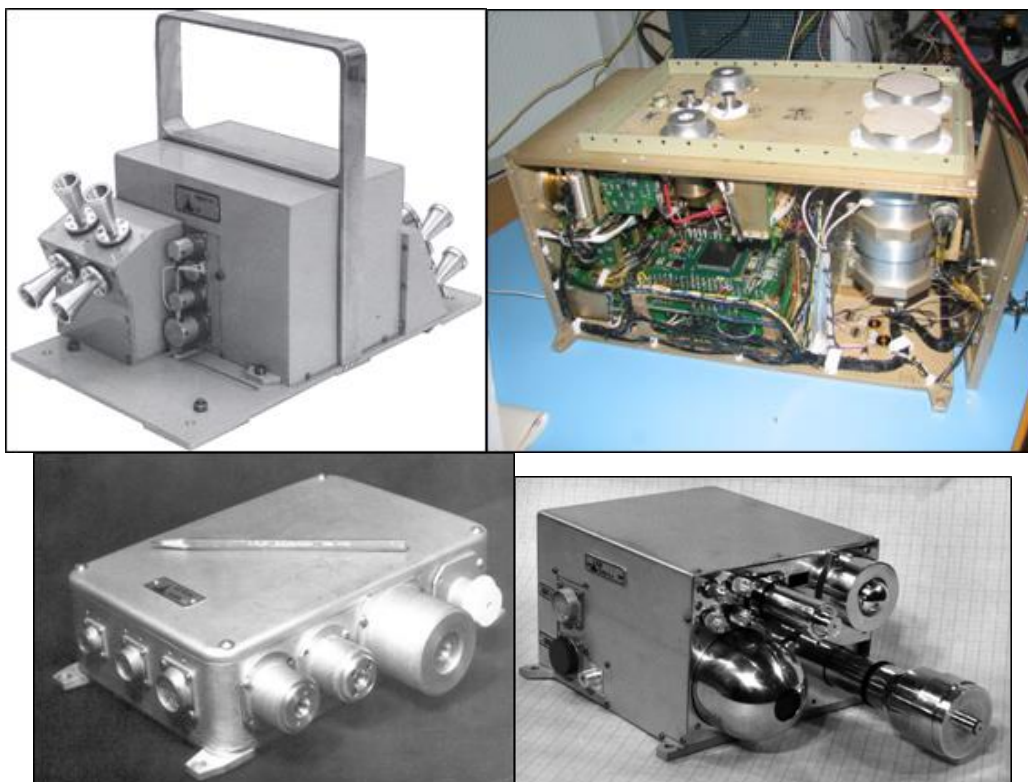


*Fig.4. Examples of instruments designed in SSD.*

Currently SSD carries out experiments on board several satellites: Meteor-M №2 (polar sun-synchronous LEO orbit with altitude ~ 820 km), GLONASS (GPS orbit altitude - 40000 km), Electro-L №2 (GEO orbit with altitude of 36 thousand km) and on board the ISS (400 km). Radiation spectrometers for measuring magnetospheric plasma, particles of radiation belts and solar cosmic rays perform continuous monitoring of radiation fields with a resolution of energy and time sufficient to identify dynamic processes in near-Earth space.

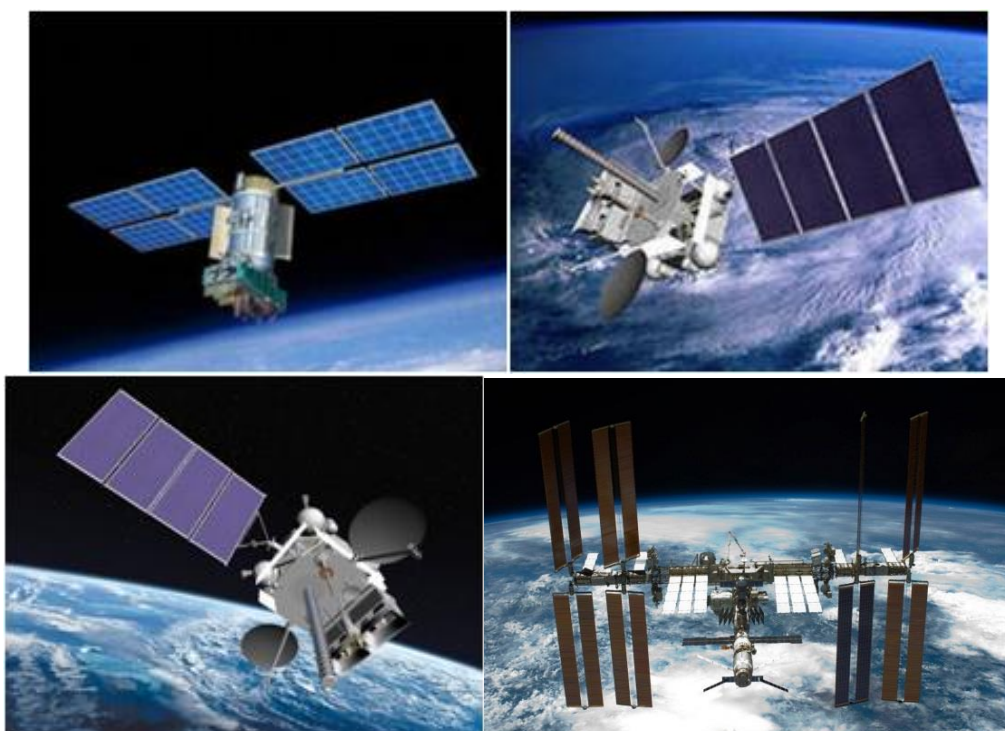


*Fig.5. Radiation instruments designed and manufactured in SSD/SINP/MSU are installed now onboard Meteor, Glonass, Electro satellites and ISS.*

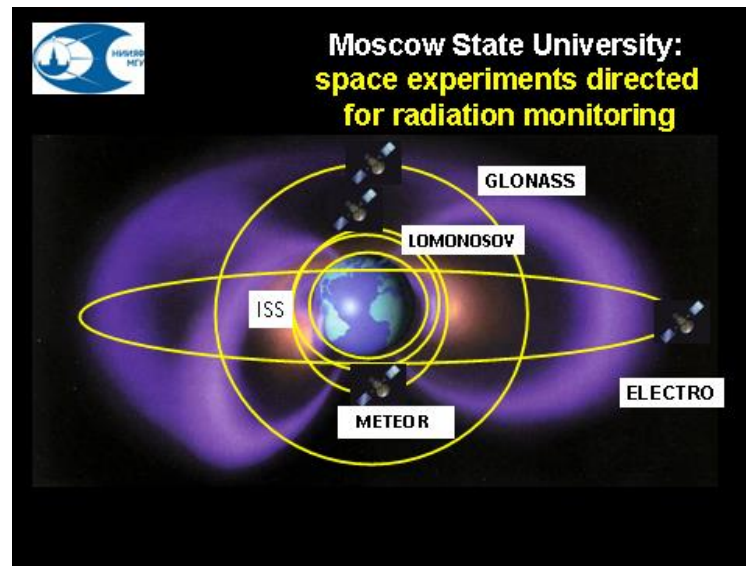


*Fig. 6. Radiation instruments designed and manufactured in SSD/SINP/MSU are installed now onboard LEO, GPS, GEO satellites and provided radiation monitoring in the Near-Space environment.*

## **The Results of Space Experiments Realized in 2016 - 2017**

### **2.5. NUCLEON SPACE EXPERIMENT**

(Skobeltsyn Institute of Nuclear Physics of Lomonosov Moscow State University)

The cosmic-rays spectrometer NUCLEON is being operated on the Earth's orbit since the beginning of 2015. The main purpose of the spectrometer is to measure the spectra of cosmic-ray nuclei with elemental charge resolution in the energy range from approximately 1 TeV ( $10^{14}$  eV) to 1 PeV ( $10^{15}$  eV) per particle. With the use of spectrometer equipment, the spectra of the main abundant cosmic ray nuclei and some interesting ratios of secondary cosmic ray fluxes to primary ones have already been measured. The results obtained should be regarded as preliminary, since the spectrometer has worked in orbit for not more than a half of the expected time. Nevertheless, very interesting results have already been obtained. The measured spectra and the ratios of spectra demonstrate a number of unexpected features, among which we note here the following two new phenomena.

1. A break in the region of about 10 TB (Fig.7.) is detected in the magnetic rigidity spectra of all abundant nuclei. The existence of such a break in the groups of different nuclei is an evidence of the universality of this phenomenon. This break

is similar to the famous cosmic-ray knee - the break of the all particles spectrum near the energy per particle of about  $3 \times 10^{15}$  eV per particle, but this new break could not be detected earlier, since none of the previous experiments gave the necessary statistics in the required energy range simultaneously with the elemental resolution of the charges of the cosmic rays nuclei. The existence of a universal break at 10 TV can be important for astrophysics, since it can indicate a certain type of supernovae explosions in which the limiting energy to which cosmic rays can be accelerated corresponds to magnetic rigidity of about 10 TV.

2. The primary nuclei of cosmic rays are those that are accelerated directly in the sources (remnants of supernovae explosions). On the contrary, the secondary nuclei of cosmic rays arise during the spallation of the primary nuclei when they interact with interstellar gas. It is expected that the ratio of the fluxes of secondary nuclei to the corresponding parent primary nuclei should be a decreasing function of energy, since the number of secondary nuclei is proportional to the time that primary nuclei spend in the galaxy and which should decrease with increasing primary nucleus energy. It is assumed that the nuclei of boron of cosmic rays have a purely secondary origin, while in the flow of nitrogen nuclei the fraction of secondary nuclei is large or predominant. Fig. 8. shows the ratios of the B/C and N/O (C and O nuclei are primary) measured by the NUCLEON spectrometer. It can be seen that the results of NUCLEON correspond well to the measurements of other experiments at low energies, but at the highest energies attained in the NUCLEON experiment, the dependencies do not demonstrate the tendency to fall. It may indicate the limitations of existing ideas about the origin of the secondary nuclei. For example, secondary nuclei can arise not only in the process of propagation of cosmic rays in the Galaxy, but already at the stage of particle acceleration, therefore part of the secondary nuclei can be accelerated in the sources, which creates an abnormally high number of high-energy secondary nuclei.

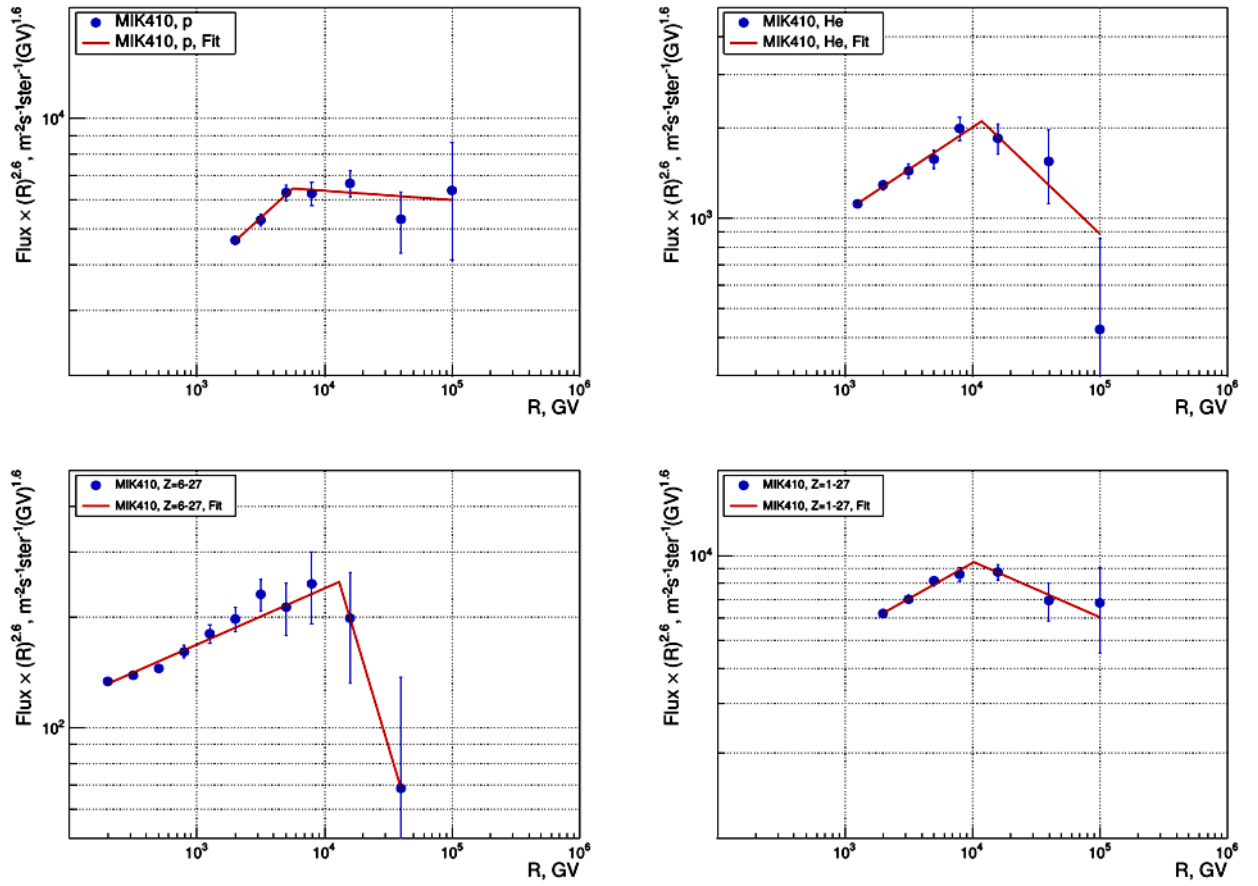


Fig. 7. Universal break near  $R=10$  TV: rigidity spectra of protons, helium, all nuclei  $Z=6-27$ , and all-particle spectrum.

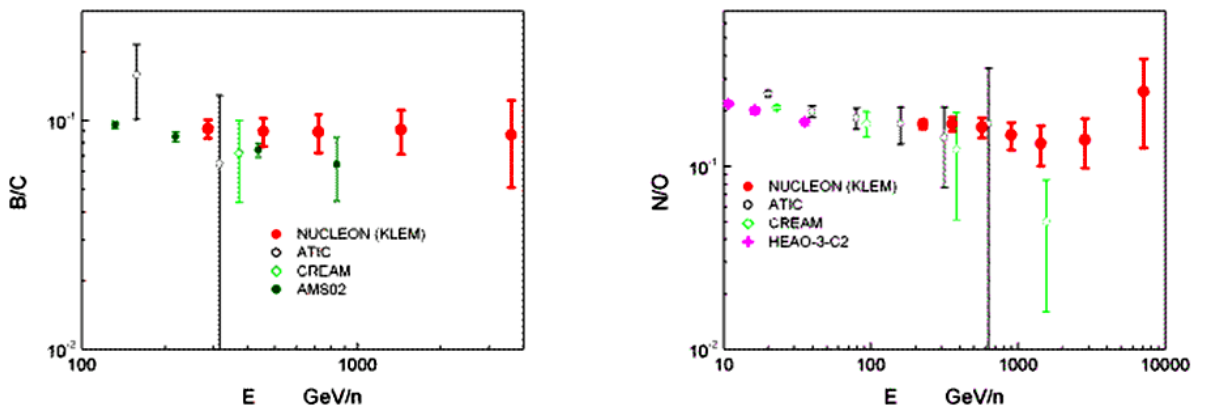


Fig. 8.  $B/C$  and  $N/O$  ratios.

## Selected publications

2017 First results of the cosmic ray NUCLEON experiment  
 Atkin E., Bulatov V., Dorokhov V., Gorbunov N., Filippov S., Grebenyuk V.,  
 Karmanov D., Kovalev I., Kudryashov I., Kurganov A., Merkin M., Panov A.,

*Podorozhny D., Polkov D., Porokhovoy S., Shumikhin V., Sveshnikova L., Tkachenko A., Tkachev L., Turundaevskiy A., Vasiliev O., Voronin A.*  
*in Journal of Cosmology and Astroparticle Physics, publisher Institute of Physics (United Kingdom), tom 2017, № 7, p. 20 DOI*

*2017 The NUCLEON experiment. Results of the first year of data acquisition*  
*Atkin E., Bulatov V., Dorokhov V., Filippov S., Gorbunov N., Grebenyuk V., Karmanov D., Kovalev I., Kudryashov I., Kurganov A., Merkin M., Panov A., Podorozhny D., Polkov D., Porokhovoy S., Shumikhin V., Sveshnikova L., Tkachenko A., Tkachev L., Turundaevskiy A., Vasiliev O., Voronin A.*

## **2.6. TUS EXPERIMENT ONBOARD LOMONOSOV SATELLITE**

(Skobeltsyn Institute of Nuclear Physics of Lomonosov Moscow State University)

The TUS detector is accommodated on board of the LOMONOSOV satellite (international designation MVL 300, or 2016-026A). It was launched on April 28, 2016, on a polar sun-synchronous orbit with inclination of  $97^{\circ}.3$ , a period of  $\sim 94$  min, and an altitude of about 500 km.

The TUS detector consists of two main parts: a parabolic mirror-concentrator of the Fresnel type and a square-shaped 256-pixel photodetector in the focal plane of the mirror. The mirror has an area of about  $2 \text{ m}^2$  with a focal distance of 1.5 m. A pixel field of view (FOV) is equal to 10 mrad, which results in space resolution at the atmosphere 5 km with the area of TUS FOV approximately  $80 \text{ km} \times 80 \text{ km}$  at sea level. Pixels of the TUS photodetector are photomultiplier tubes Hamamatsu R1463 with multialkali cathode of 13 mm diameter. The pixel wavelength band 240-400 nm is limited by a UV filter and by PMT quantum efficiency. The pixels are grouped in 16 identical photodetector modules. Each cluster has its own digital data processing system for the first-level trigger, based on a Xilinx field-programmable gate array (FPGA), and a high voltage power supply, controlled by the FPGA. The central processor board gathers information from all modules, controls their operation, and implements the second-level trigger algorithm.

The TUS electronics can be operated in four modes intended for detecting various fast optical phenomena in the atmosphere at different time scales with different time sampling. The main mode is aimed at registering extensive air showers (EASs) born by ultra high energy cosmic rays and has a time sampling of  $0.8 \mu\text{s}$ . This mode is also efficient for detection of elves – the most common type of transient luminous events (TLEs). Three other modes have time sampling of  $25.6 \mu\text{s}$  and  $0.4 \text{ ms}$  for studying TLEs of different kinds slower than elves: sprites, blue jets, gigantic jets, etc., and  $6.6 \text{ ms}$  for detecting micro-meteors, space debris and thunderstorm activity at a longer time scale ( $\sim 1.7 \text{ s}$ ). Waveforms in each mode (a “record”) consist of 256 time samples.

TUS on board the LOMONOSOV satellite and during preflight preparations at COSMODROME VOSTOCHNY is shown in Fig.14.

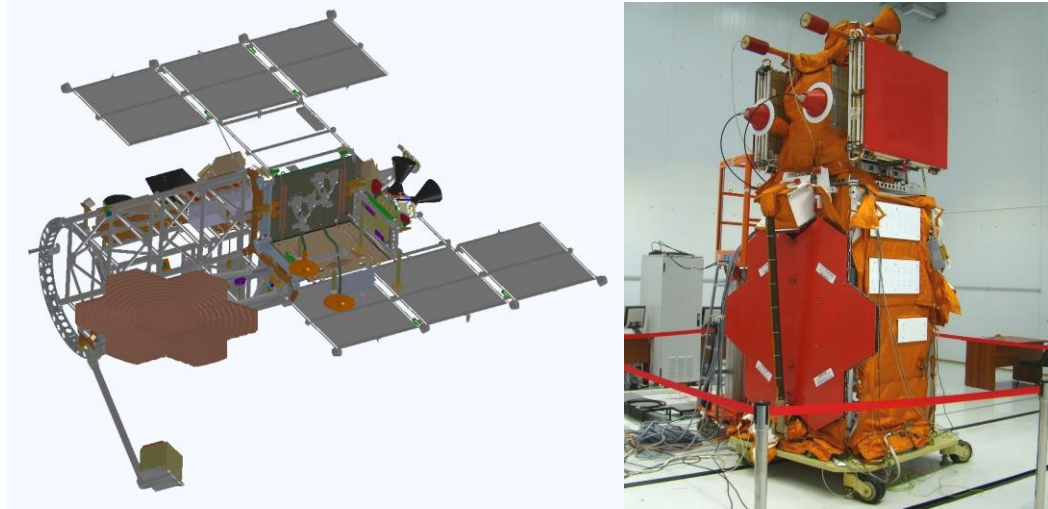


*Fig.14. Artist's view of the TUS detector onboard the LOMONOSOV satellite (upper panel). TUS onboard the LOMONOSOV satellite covered with a protective cover during preflight preparations at COSMODROME VOSTOCHNY (lower panel).*

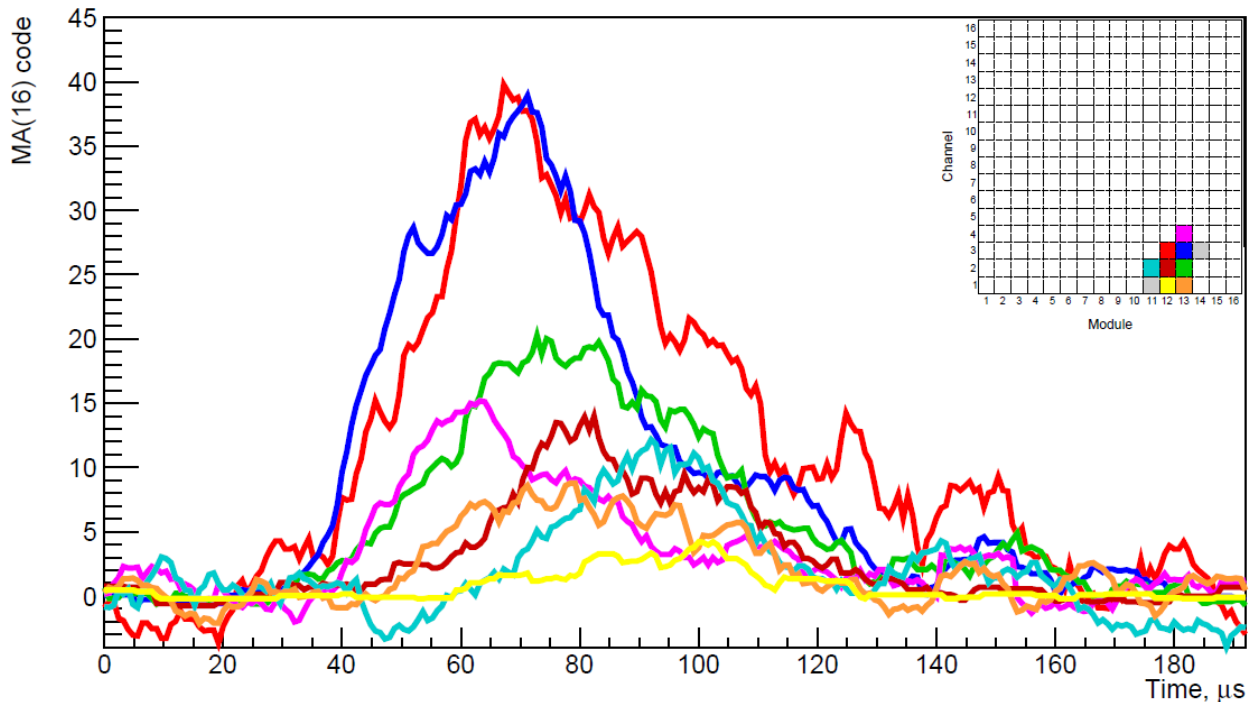
TUS began measurements in space on May 19, 2016. Continuous measurements were started in September 2016 with several gaps for the satellite technical service. During one year of measurements, TUS registered around 35,000 events at nocturnal parts of its orbit in the EAS mode. The total exposure is approximately  $530 \text{ km}^2 \text{ yr sr}$ . It is small in comparison with that of the largest ground-based arrays but sufficient to look for an EECR above the TUS threshold energy  $E > 70 \text{ EeV}$ .

During the search for possible EAS candidates, approximately 10,000 events registered in the conditions of the minimal background radiation were analyzed and considered. A list of various criteria was developed basing on simulations of a few thousand EECRs with different parameters of primary particles and an analysis of different types of “noise” events in the data set. The procedure led us to a list of 13 events. The next step of the analysis is an event by event study of the temporal and spatial dynamics of the signal. This analysis is aimed to search for typical EAS signatures taking into account the characteristic temporal parameters, signal amplitudes and image structure. The majority of EAS-like events can be related to fast anthropogenic signals (for example, airports).

The first candidate is presented in Fig.15. – event measured on October 03, 2016. It has the most interesting spatial-temporal dynamics similar to what is expected for EAS (in order to minimize statistical fluctuations we express signal as moving average with width parameter  $M=16$ ). Active pixels are grouped in an oblong spot. The moment of the maximum of the signal in each pixel has some shift from one pixel to another which can be interpreted as EAS image movement. A possible thunderstorm activity was studied in the region of this event measurements. The Vaisala GLD360 ground based lightning location network did not register any lightning strikes in a region with radius of  $\sim 930 \text{ km}$  and during  $\sim 10 \text{ s}$  period around

the time of the TUS event. It provides a strong support for a non-thunderstorm origin of the event.

*Fig.15. EAS candidate measured on October 03, 2016: moving average of ADC counts for active pixels (individual base levels are subtracted) and corresponding pixel map.*



#### *Selected publications*

*P. A. Klimov, M. I. Panasyuk, B. A. Khrenov, G. K. Garipov, N. N. Kalmykov, V. L. Petrov, S. A. Sharakin, A. V. Shirokov, I. V. Yashin, M. Y. Zotov, S. V. Biktemerova, A. A. Grinyuk, V. M. Grebenyuk, M. V. Lavrova, L. G. Tkachev, A. V. Tkachenko, I. H. Park, J. Lee, S. Jeong, O. Martinez, H. Salazar, E. Ponce, O. A. Saprykin, A. A. Botvinko, A. N. Senkovsky, and A. E. Puchkov. The TUS detector of extreme energy cosmic rays on board the Lomonosov satellite. Space Science Reviews, p. 1–17, 2017.*

*B. A. Khrenov, P. A. Klimov, M. I. Panasyuk, S. A. Sharakin, L. G. Tkachev, M. Yu Zotov, S. V. Biktemerova, A. A. Botvinko, N. P. Chirskaya, V. E. Ereemeev, G. K. Garipov, V. M. Grebenyuk, A. A. Grinyuk, S. Jeong, N. N. Kalmykov, M. Kim, M. V. Lavrova, J. Lee, O. Martinez, I. H. Park, V. L. Petrov, E. Ponce, A. E. Puchkov, H. Salazar, O. A. Saprykin, A. N. Senkovsky, A. V. Shirokov, A. V. Tkachenko, and I. V. Yashin. First results from the tus orbital detector in the extensive air shower mode. Journal of Cosmology and Astroparticle Physics, 2017.*

*A. Grinyuk, V. Grebenyuk, B. Khrenov, P. Klimov, M. Lavrova, M. Panasyuk, S. Sharakin, A. Shirokov, A. Tkachenko, L. Tkachev, I. Yashin, The orbital TUS detector simulation, Astroparticle Physics, <http://dx.doi.org/10.1016/j.astropartphys.2016.09.003>.*

*P. A. Klimov, M. Yu Zotov, N. P. Chirskaya, B. A. Khrenov, G. K. Garipov, M. I. Panasyuk, S. A. Sharakin, A. V. Shirokov, I. V. Yashin, A. A. Grinyuk, A. V. Tkachenko, and L. G. Tkachev. Preliminary results from the TUS ultra-high energy cosmic ray*

*orbital telescope: Registration of low-energy particles passing through the photodetector. Bulletin of the Russian Academy of Sciences: Physics, 81(4):407–409, 2017.*

## **2.7. Gamma- ray bursts observations onboard VERNOV and LOMONOSOV satellites**

(Skobeltsyn Institute of Nuclear Physics of Lomonosov Moscow State University)

The gamma ray and electron spectrometer BDRG was the part of the complex of RELEC scientific instrument onboard VERNOV spacecraft launched on July 8, 2014. This instrument includes a set of scintillator phoswich detectors consisted of four identical X- and gamma- ray detectors for the range from 10 keV to 3 MeV, with total area of about 500 cm<sup>2</sup> directed to the nadir and electron spectrometer consisted of three mutually orthogonal detectors each with the geometric factor of  $\sim 2$  cm<sup>2</sup>sr, sensitive also to X- and gamma-rays.

The aim of space experiment with DRGE instrument was to study the phenomena with fast temporal variability, in particular, Terrestrial gamma-ray flashes (TGF) and precipitated magnetosphere electrons. However, the DRGE instrument was also able to detect cosmic gamma-ray bursts and allowed not only to carry out a detailed analysis of the variability in the gamma range, but also to compare the time profiles with measurements of the other RELEC instruments (detector of optical and ultraviolet flashes, radio-frequency and low-frequency analyzers of electromagnetic fields).

At least two cosmic gamma-ray bursts GRB141011A, GRB141104A were detected in RELEC experiment (Fig. 22.). Their spectral and temporal parameters were estimated and compared with the parameters obtained in the GBM/Fermi and KONUS-Wind experiments. The red shift and  $E_{\text{iso}}$  of these gamma-ray burst sources were estimated. The detection ability and good agreement between independent estimates of the gamma-ray burst parameters obtained in different experiments is an important factor in the successful operation of similar detectors installed onboard of the LOMONOSOV spacecraft.



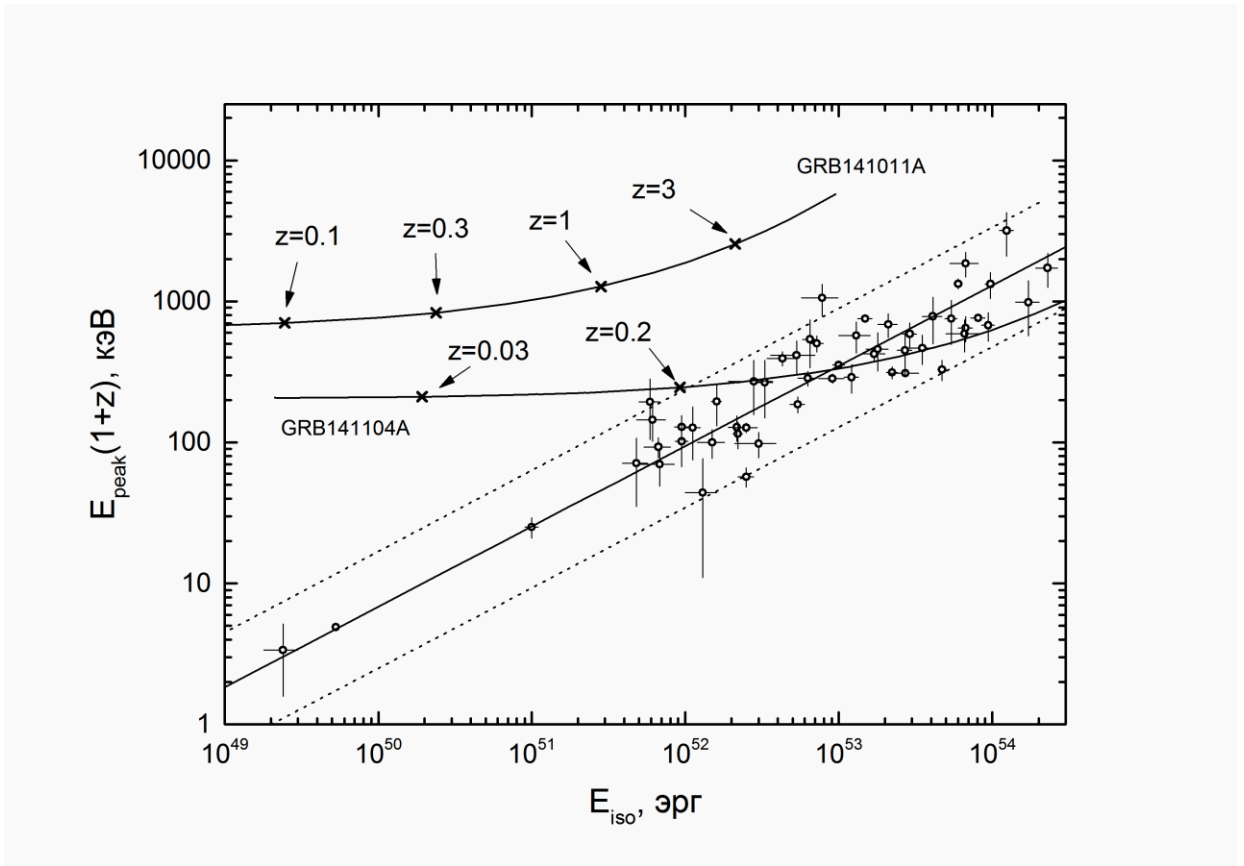


Fig.22. Amati diagram - the dependence of the equivalent isotropic energy emitted in the gamma range,  $E_{iso}$  on the parameter  $E_{peak}(1+z)$  in the source reference frame for long bursts according to the data of the KONUS-Wind experiment. The continuous straight line shows the approximation of the dependence by the power function, the dashed lines are bounded by the correlation region. The trajectories GRB 141011A and GRB141104A are plotted as a function of the assumed redshift  $z$ .

The study of GRB prompt emissions (PE) is one of the main goals of the LOMONOSOV space mission. The payloads of the GRB monitor (BDRG) with the wide-field optical cameras (SHOK) and the ultra-fast flash observatory (UFFO) onboard the LOMONOSOV satellite are intended for the observation of GRBs, and in particular, their prompt emissions. The BDRG gamma-ray spectrometer is designed to obtain the temporal and spectral information of GRBs in the energy range of 10-3000 keV as well as to provide GRB triggers on several time scales (10ms, 1s and 20s) for ground and space telescopes, including the UFFO and SHOK. The BDRG instrument consists of three identical detector boxes with axes shifted by  $90^\circ$  from each other. This configuration allows us to localize a GRB source in the sky with an accuracy of  $\sim 2^\circ$ .

Each BDRG box contains a phoswich NaI(Tl)/CsI(Tl) scintillator detector. A thick CsI(Tl) crystal in size of 130 x 17 mm is placed underneath the NaI(Tl) as an active shield in the soft energy range and as the main detector in the hard energy range. The ratio of the CsI(Tl) to NaI(Tl) event rates at varying energies can be

employed as an independent metric to distinguish legitimate GRB signals from false positives originating from electrons in near-Earth vicinities.

The data from three detectors are collected in a BA BDRG information unit, which generates a GRB trigger and a set of data frames in output format. The scientific data output is ~500 Mb per day, including ~180 Mb of continuous data for events with durations in excess of 100ms for 16 channels in each detector, detailed energy spectra, and sets of frames with ~5Mb of detailed information for each burst-like event. A number of pre-flight tests including those for the trigger algorithm and calibration were carried out to confirm the reliability of the BDRG for operation in space. The real time data transfer in the GCN for detected GRB is realized as well as operative control of BDRG data on triggers from ground based facilities including neutrino and gravitation wave detectors. The GRB catalogue contained more than 20 GRBs prepared. The example of GRB detected on LOMONOSOV by BDRG instrument is presented in Fig. 23.

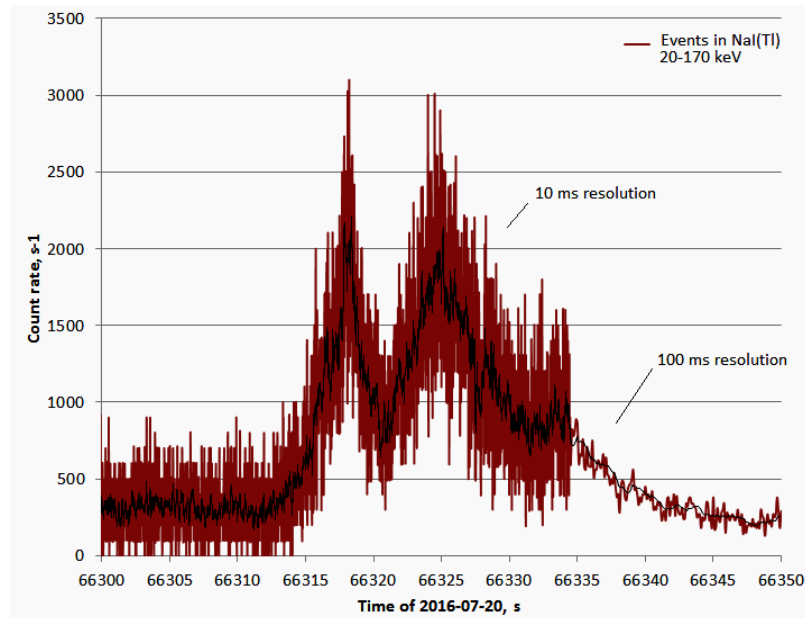


*Fig.23. The time profile of counting rate in the NaI(Tl) 20-170 keV range of the BDRG-2 detector for GRB16.07.20.*

#### *Selected publications*

*Cosmic Gamma-Ray Bursts Detected in the RELEC Experiment Onboard the Vernov Satellite* A.V. Bogomolov, V.V. Bogomolov, A.F. Iyudin et al. *Astron. Lett.* 2017. Vol.43, Iss.8, pp.516–528. DOI: 10.1134/S1063773717080023.

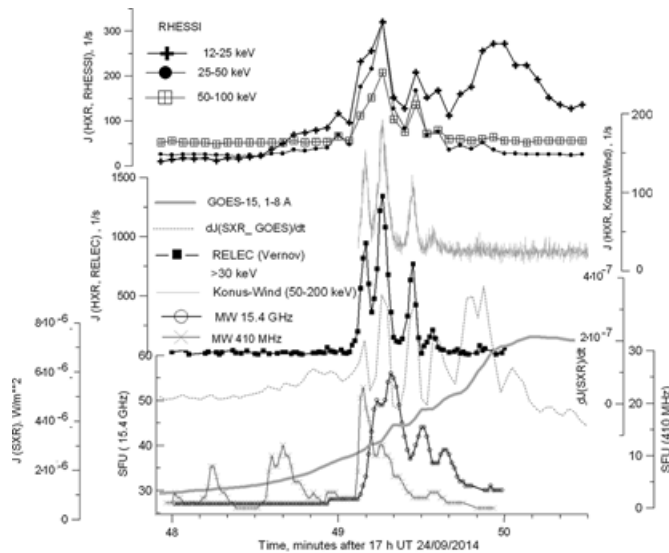
*Wide-Field Gamma-Spectrometer BDRG: GRB Monitor on-board the Lomonosov Mission.* Svertilov S.I., Panasyuk M.I., Bogomolov V.V., et al. *Space Science Reviews*, publ. *Kluwer Academic Publishers* (Netherlands). 2018. V.214, №8, pp.1-22. DOI: 10.1007/s11214-017-0442-9.

SHOK — The Field Optical Vladimir Gorbovs koy, al., Space publ. Kluwer Publishers V.214, №6, pp.1-10.1007/s11214-

The Payload for Early Photons

Bursts. Park I.H., Panasyuk M.I., Reglero V., et al. Space Science Reviews, publ. Kluwer Academic Publishers(Netherlands). 2018. V.214, №14, pp.1-21. DOI 10.1007/s11214-017-0444-7.

UBAT of UFFO/Lomonosov: The X-Ray Space Telescope to Observe Early Photons from Gamma-Ray Bursts. Space Sci Rev publ. Kluwer Academic Publishers (Netherlands). 2018. V.214, №16, pp.1-25. DOI 10.1007/s11214-017-0454-5.



first Russian Wide-Camera in Space. Lipunov, Evgeny Victor Kornilov et Science Reviews, Academic (Netherlands). 2018. 16.DOI: 017-0441-x.

UFFO/Lomonosov: the Observation of from Gamma Ray

## 2.8. Solar X-ray Emission Measured by VERNOV Mission During September - October 2014

(Skobeltsyn Institute of Nuclear Physics of Lomonosov Moscow State University)

X-ray and  $\gamma$ -ray emissions were measured by the Detector of the Roentgen and Gamma-ray Emissions (DRGE) instrument, which is part of the RELEC set of instruments operated onboard VERNOV spacecraft, from July 8, 2014 until December 10, 2014 (on a solar-synchronous orbit with an apogee of 830 km, perigee of 640 km, and an inclination of  $98.4^\circ$ ). RELEC measurements of 18 flares with X-ray energy  $> 30$  keV, taken in September – October 2014, were connected with the same active region with the number AR 12172 during the first rotation and AR 12192 during the next one. These measurements were compared to the data obtained with RHESSI, Konus-Wind, Fermi Observatory, Radio Solar Telescope Net (RSTN), and the Nobeyama Radioheliograph (NoRH) operated at the same time. Quasi-periodicities with similar periods of  $7 \pm 2$  s were found in about one third of all flares measured by RELEC (VERNOV) from September 24 until October 30, 2014.

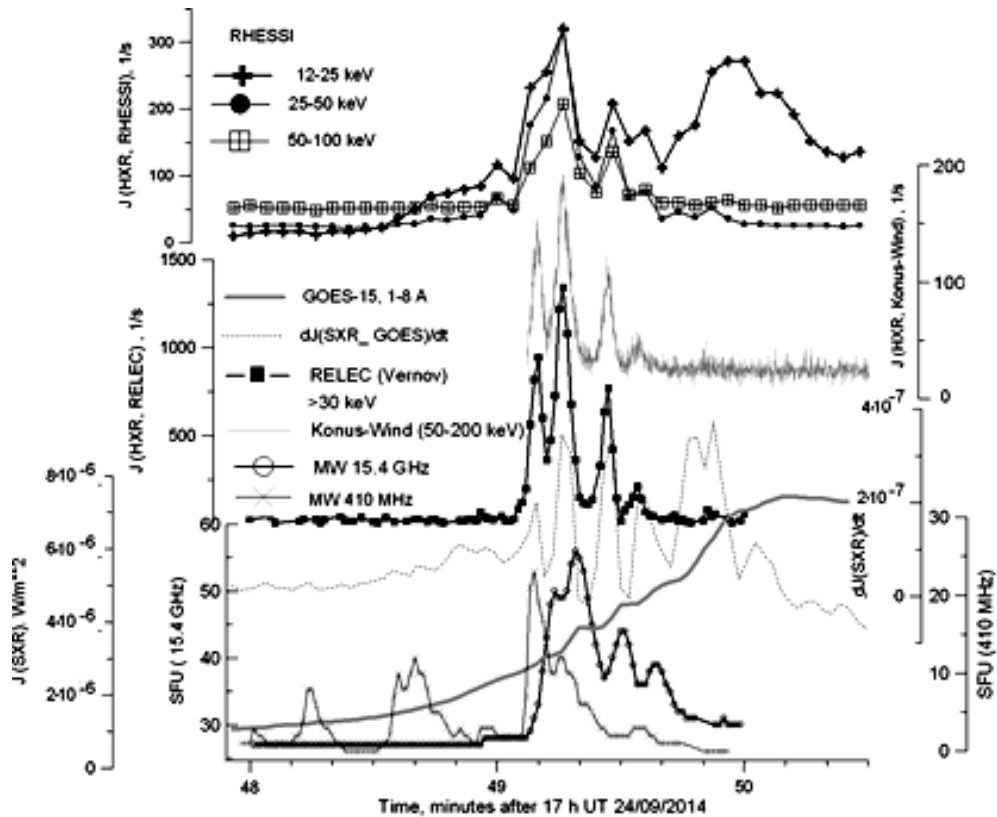


Fig. 35. Time profiles of the HXR emission measured during a C7.0 solar flare at about 17:49 UT on September 24, 2014 by RELEC (VERNOV), Konus-Wind and RHESSI experiments, and the SXR emission by GOES, the MW emission (RSTN).

#### Selected publications

“Time delays in the nonthermal radiation of solar flares according to observations of the CORONAS-F satellite”, Tsap, Yu. T.; Stepanov, A. V.; Kashapova, L. K.; Myagkova, I. N.; Bogomolov, A. V.; Kopylova, Yu. G.; Goldvarg, T. B., *Cosmic Research, Volume 54, Issue 1, pp.285-289 (01/2016)*

## 2.9. Catalogue of solar flares with registration of hard x-rays onboard LOMONOSOV satellite

(Skobeltsyn Institute of Nuclear Physics of Lomonosov Moscow State University)

The experiment onboard LOMONOSOV satellite has shown that rigid x-ray radiation with energy  $>10$  keV can be observed during weak C and B class flares (GOES classification by soft x-ray radiation), which experimentally confirms the possibility of accelerating particles in the flash without heating solar plasma. As an example of such a weak event in Fig.35.presents the flash time profile of class B5.6 GOES on July 11 (beginning 08:34 - maximum 08:38 - end 08:42), which occurred on July 11, 2016 in the active region AR12574.

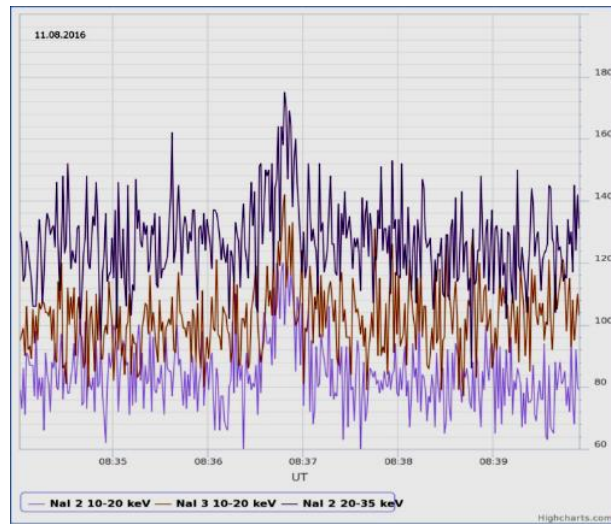


Fig.36. Time profile of solar accelerated particles in different energy ranges.

A catalog of solar flares was created in which rigid x-rays of the Sun were recorded.

№	Day/month of 2016	Time, start-max-end in SXR, hh:mm (GOES)	Class SXR	Time, start- end in HXR, hh:mm:ss (ЛОМОНОСОВ)	QPP	Other experiments	AR
1.	19/06	11:44-11:58-12:08	C1.7	11:44:20-11:57:40	+	dGoes/dt	12558
2.	09/07	09:01-09:05-09:05	B9.8	13:01:15-13:04:00	-	dGoes/dt	12564
3.	10/07	00:53-00:59-01:03	C8.6	00:56:20 - 00:59:40	+	F	12564
4.	18/07	08:09-08:23-08:32	C4.4	08:11:00-08:16:10	+	F	12567
5.	20/07	23:02-23:29-23:55	C5.0	23:04:45-25:05:30	-	F, N	12567
6.	21/07	00:42-00:46-50:00	M1.2	19:00:53-19:01:45	+	F, N	12567
6	07/08	05:28-05:35-05:40	C1.3	05:33:55-05:34:10	+	F	12571
7.	07/08	10:18- 10:24 -10:29	C1.6	10:22:15-10:24:50	-	F	-
9.	11/08	08:34- 08:38 -08:42	B5.6	08:36:20-08:37:30	-	R	12574
10.	14/08	19:29-19:36-19:39	C1.1	19:34:00-19:35:15	-	R	12578
11.	15/08	00:17-00:23-00:29	C1.1	00:19:20-00:22:52	+	R	12578

Fig. 37. An example of catalog of X-ray solar flares according to LOMONOSOV satellite measurements.

#### Selected publication

Chloe E. Pugh, V. M. Nakariakov, Anne-Marie Broomhall, Andrey V. Bogomolov, Irina N. Myagkova «Properties of quasi-periodic pulsations in solar flares from a single active region» Article in *Astronomy and Astrophysics* · September 2017 DOI: 10.1051/0004-6361/201731636

## 2.10. Dynamics of electron fluxes in the gap between the radiation belts of the Earth

(Skobeltsyn Institute of Nuclear Physics of Lomonosov Moscow State University)

The nature of variations in the flux of relativistic electrons in the gap between the radiation belts of the Earth and the polar boundary of the outer radiation belt according to the experiments on the ISS, VERNOV and LOMONOSOV is investigated. It is shown that there is a constant presence of spilling electrons in the high-latitude magnetosphere, presumably associated with pitch-angular diffusion on curved magnetic lines in the plasma layer and scattering on electrostatic waves in the upper hybrid resonance.

### *Selected publication*

1. A. V. Bogomolov, I. N. Myagkova, V. V. Kalegaev, S. I. Svertilov, V. V. Bogomolov, M. I. Panasyuk, V. L. Petrov and I. V. Yashin «Precipitation of Subrelativistic-Energy Electrons near the Polar Boundary of the Earth Radiation Belt according to the Data of Measurements on the Vernov and Lomonosov Satellites» *Cosmic Research (English translation of Kosimicheskije Issledovaniya)*, 55(6):464–468, 2017.
2. M. I. Panasyuk, V. V. Kalegaev, I. N. Myagkova, N. V. Kuznetsov, and M. V. Podzolko. *Radiation environment at the end of active functioning of “vernov” satellite. Cosmic Research (English translation of Kosimicheskije Issledovaniya)*, 55(6):464–468, 2017.
3. *Radiation environment at the end of active functioning of “Vernov” satellite* Panasyuk M.I., Kalegaev V.V., Myagkova I.N., Kuznetsov N.V., Podzolko M.V. *Cosmic Research (English translation of Kosimicheskije Issledovaniya)*, *Maik Nauka/Interperiodica Publishing (Russian Federation)*, 55, № 6, c. 464-468, 2017

## 2.11. Prediction of variations in the flux of relativistic electrons in the outer radiation belt of the Earth

(Skobeltsyn Institute of Nuclear Physics of Lomonosov Moscow State University)

Short-term and medium-term methods have been developed for predicting the radiation state of Near-Earth space-variations in the flows of relativistic electrons in the outer radiation belt of the Earth, and geomagnetic indices Dst, Kp, Ap, carried out using artificial neural networks. The comparison of the quality of predicting of fluxes of relativistic electrons of the outer radiation belt for various adaptive methods - artificial neural networks, method of group account of arguments and the method of projection on latent structures, it is shown that the best result are shown the neural network.

### *Selected publication*

1. I. N. Myagkova, S. A. Dolenko, A. O. Eitarou, V. R. Broad, and N. S. Sentemova. *Prediction of the flow of relativistic electrons of the outer radiation belt Of the earth in*

*the geostationary orbit by means of adaptive methods. Geomagnetism and Aeronomy, 57(1):10-18, 2017.*

2. I.Myagkova, S.Dolenko. *Confirmation of the Effect of Simultaneous Time Series Prediction with Multiple Horizons at the Example of Electron Daily Fluence in Near-Earth Space. A.Lintas et al. (Eds.): ICANN-2017, Part II, Lecture Notes in Computer Science, V.10614, pp.774-775. 2017*

## 2.12. Dynamics of the Ring Current Relative to Magnetotail Currents

(Skobeltsyn Institute of Nuclear Physics of Lomonosov Moscow State University)

As a result of studying the 30–80-keV ion fluxes from data of the NOAA polar spacecrafts (POES), the dependences of maximum flux values (as measured by the  $0^\circ$  detector (orthogonal to the spacecraft orbit) at high latitudes and in the near-equatorial region) on the power of 15 geomagnetic storms have been studied. It is shown that, while in the near-equatorial region, the maximum ion fluxes normalized to  $|Dst|$  (here the  $0^\circ$  detector measures fluxes of trapped particles) increase with the storm power, and the high-latitude maximum ion fluxes, normalized to  $|Dst|$ , decrease (the  $0^\circ$  detector measures fluxes of precipitating particles). Considering the near-equatorial particle fluxes as a “reflection” of the ring current and associating the high-latitude fluxes with the particle injection from the plasma sheet, which characterizes the magnetotail current system, we find that the importance of RC becomes dominant with growth in the intensity of magnetic storms when compared to the one of tail currents. Our experimental results confirm similar dependences calculated on the basis of the A2000 paraboloid model, and the conclusion that the relative contribution of the ring current to  $Dst$  increases in comparison with the contribution from tail currents with growth in  $|Dst|_{\max}$ .

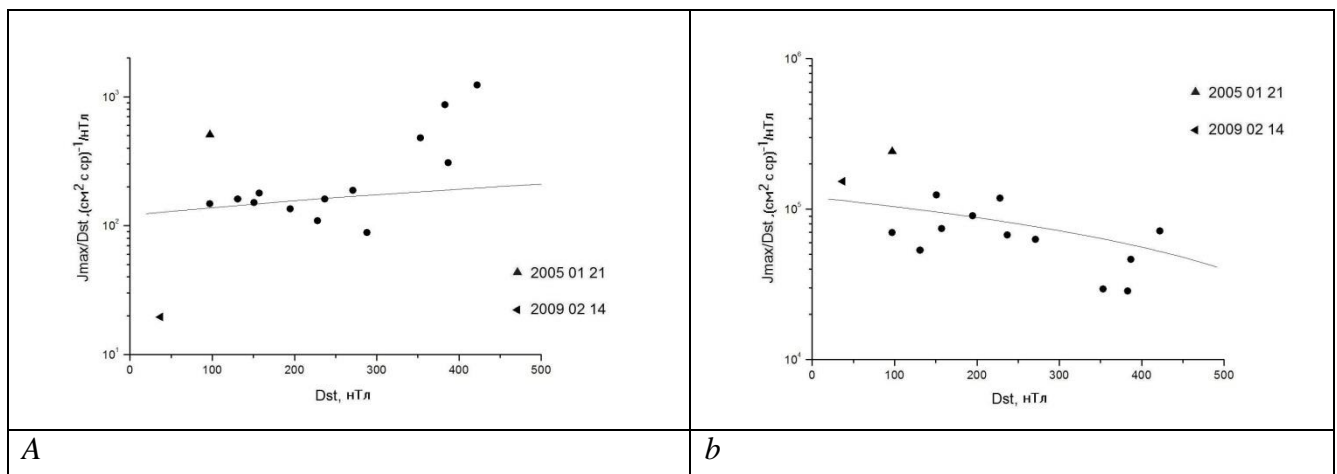


*Fig.39. Ratio of the maximum flux of trapped ions (a) and of precipitating ions (b) to the minimum value of Dst variation ( $J_{\max}/|Dst|_{\min}$ ) as a function of  $|Dst|_{\max}$ .*

*Selected publication*

V. V. Kalegaev and N. A. Vlasova. *Dynamics of the Ring Current Relative to Magnetotail Currents during Geomagnetic Storms of Different Intensity // Geomagnetism and Aeronomy, 2017, Vol. 57, No. 5, pp. 529–534.*

### 2.13. Auroral oval and the role of the ring current in the creation of the Dst / SYM-H variation

(Skobeltsyn Institute of Nuclear Physics of Lomonosov Moscow State University)

The structures of the main magnetospheric current systems are interesting to researchers because of their key role in magnetospheric physics, including the generation of geomagnetic storms and substorms. Ring current and tail current are usually considered as main sources of geomagnetic activity. The ring current is assumed to be divided into the inner part located from  $\sim 3$  to  $\sim < 7 R_E$  and the outer part located from  $7 R_E$  to the magnetopause near noon and to  $\sim 10-13 R_E$  near midnight. The outer part of the ring current is named as the cut ring current (CRC). Due to compression of the geomagnetic field by the solar wind, the CRC is not concentrated near the equatorial plane at the noon sector, it spreads along field lines. The main properties of CRC and its role in the generation of field-aligned currents is discussed. A method - based on the conservation of plasma pressure along a current line - that enables us to determine the position of the boundary between the ring and tail currents, and to determine the configuration of current lines which cross the magnetopause is proposed. At the same time, conservation of plasma pressure along a field line for plasmas in magnetostatic equilibrium enables the analysis of the auroral oval mapping into the equatorial plane regardless of any magnetic field model. It is well known that the auroral oval has a thick ring-like shape. It is discussed that it is topologically impossible to map such a structure to a sheet band like structure in the tail. This analysis has shown that most of the auroral oval is mapped to the CRC region. It is shown that including CRC as a part of the ring current allows to re-establish the traditional point of view, in which the ring current has a dominant role in Dst/SYM-H variations.

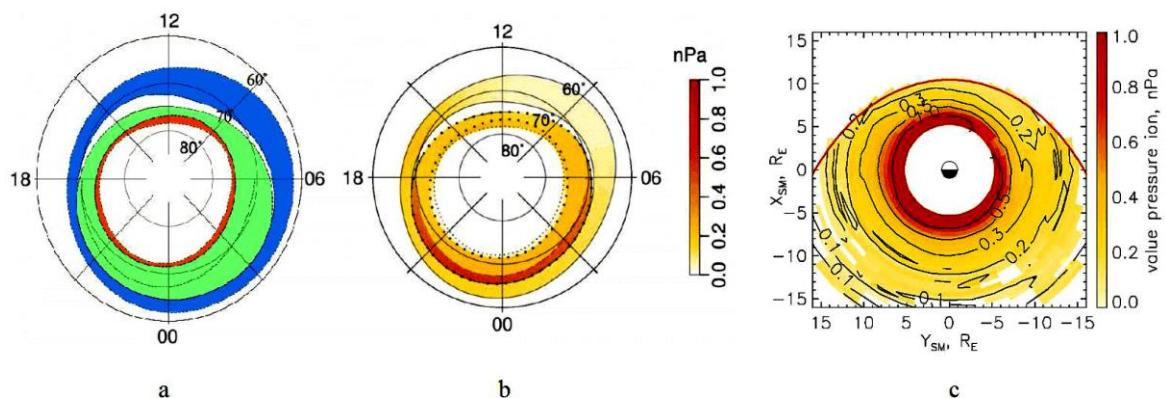




Fig. 40. Auroral regions in accordance with APL model (a) and comparison of the ion pressure distribution at ionospheric altitudes (b) and at the equatorial plane (c).

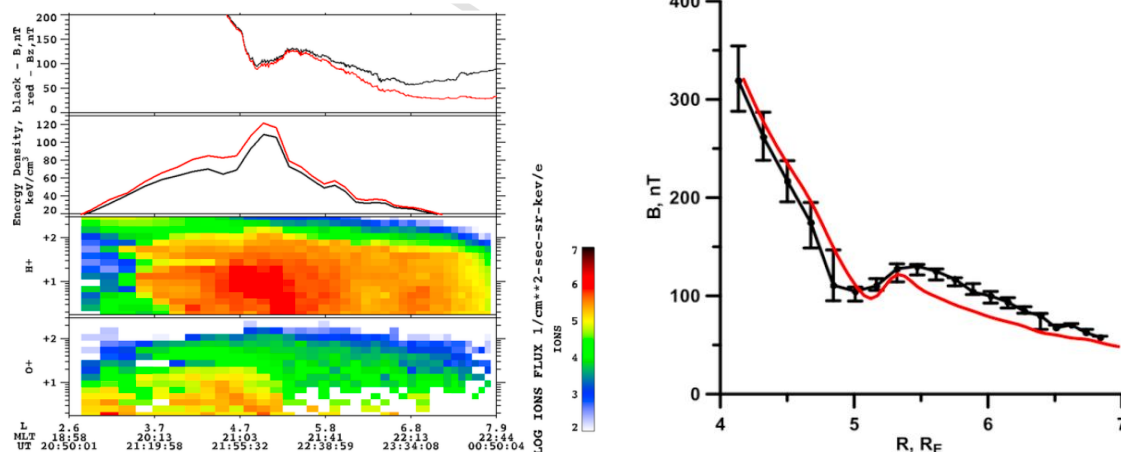
### Selected publication

Antonova E. E., M. Stepanova, I. P. Kirpichev, I. L. Ovchinnikov, V. G. Vorobjev, O. I. Yagodkina, M. O. Riazanseva, V. V. Vovchenko, M. S. Pulinets, S. S. Znatkova, N. V. Sotnikov, Structure of magnetospheric current systems and mapping of high latitude magnetospheric regions to the ionosphere, *Journal of Atmospheric and Solar-Terrestrial Physics* (2017), doi: 10.1016/j.jastp.2017.10.013.

## 2.14. Local magnetic field decreases in the region of Ring current

(Skobeltsyn Institute of Nuclear Physics of Lomonosov Moscow State University)

Using data from the AMPTE/CCE satellite inside the ring current region, the local reductions of the  $B_z$  component of the geomagnetic field were studied. The AMPTE/CCE satellite was chosen due to the good stable characteristics of the instruments and, more importantly, the ion composition measurements (for example, in the THEMIS experiment, the ion composition was not determined). The  $B_z$  reductions were followed by subsequent enhancements, as a function of geocentric distance. 102 comparatively large-scale and quasi-stable reduction/enhancement events were selected and their radial and magnetic local time (MLT) distribution was obtained. It was found out that these structures were observed for all MLT in the ring current region. Moreover, the probability to observe reduction/enhancement structures increases with the increase of geomagnetic activity, as measured by the Dst, AE, and PC indexes, and with the increase of the interplanetary magnetic field  $B_z$  component and the solar wind velocity. Detailed analyses of some of the events show that reduction/enhancement structures might be caused by diamagnetic effects due to local quasi-stationary enhancements of plasma pressure, which are observed to develop simultaneously with the magnetic depressions.



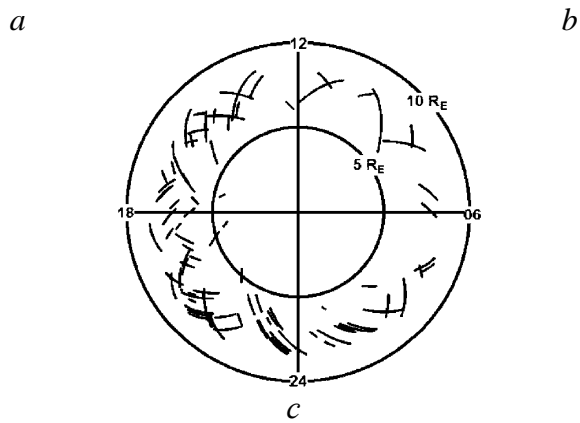


*Fig.41. Magnetic field reduction/enhancement event observed on June 6, 1985 near midnight: from top to bottom: variation of the magnetic field strength (black line) and its  $B_z$  component (red line), plasma pressure distribution obtained from  $H$  (black line) and both  $H^+$  and  $O^+$  (red line) spectrograms of particle fluxes (AMPTE/CCE observations) (a); Observed (black line) and calculated (red line) variation of the magnetic field with geocentric distance. (For interpretation of the references to colour in this figure legend (b); and Location of the magnetic depression events at the equatorial plane (c).*

#### *Selected publication*

*Vovchenko V.V., E.E. Antonova, M. Stepanova, Magnetic holes observed in the ring current region near the equatorial plane, Journal of Atmospheric and Solar-Terrestrial Physics (2017), doi:10.1016/j.jastp.2017.08.024*

*V. V. Vovchenko, E. E. Antonova, Perturbation of the magnetic field in the Earth's magnetosphere due to plateau creation in the radial distribution of plasma pressure, Geomagnetism and Aeronomy, 2017, Volume 57, Issue 3, pp 257–265, doi:10.7868/S0016794017030178*

### **2.15. The change in the position of subsolar magnetopause**

(Skobeltsyn Institute of Nuclear Physics of Lomonosov Moscow State University)

Measurements of the plasma parameters and magnetic field upon magnetopause crossings by the THEMIS-A satellite during the large magnetic storm of November 14, 2012, are analyzed. The main specific feature of this event is the magnetopause crossing at the time of the magnetic-storm maximum. An imbalance of total pressure on the magnetopause reaching up to ~40% has been observed. An abrupt turn of the magnetic field immediately on the magnetopause is recorded. Inside the magnetosphere, plasma motions have been observed, both along the magnetopause and inward, at velocities of ~100–300 km/s. Variations in geomagnetic parameters are analyzed before and after the crossing. It is shown that specific features of the observed crossing may be associated with a sharp change in the magnetospheric current systems during the magnetospheric substorm. A

change in the position of the subsolar magnetopause as a result of changes in current systems within the magnetosphere is demonstrated.

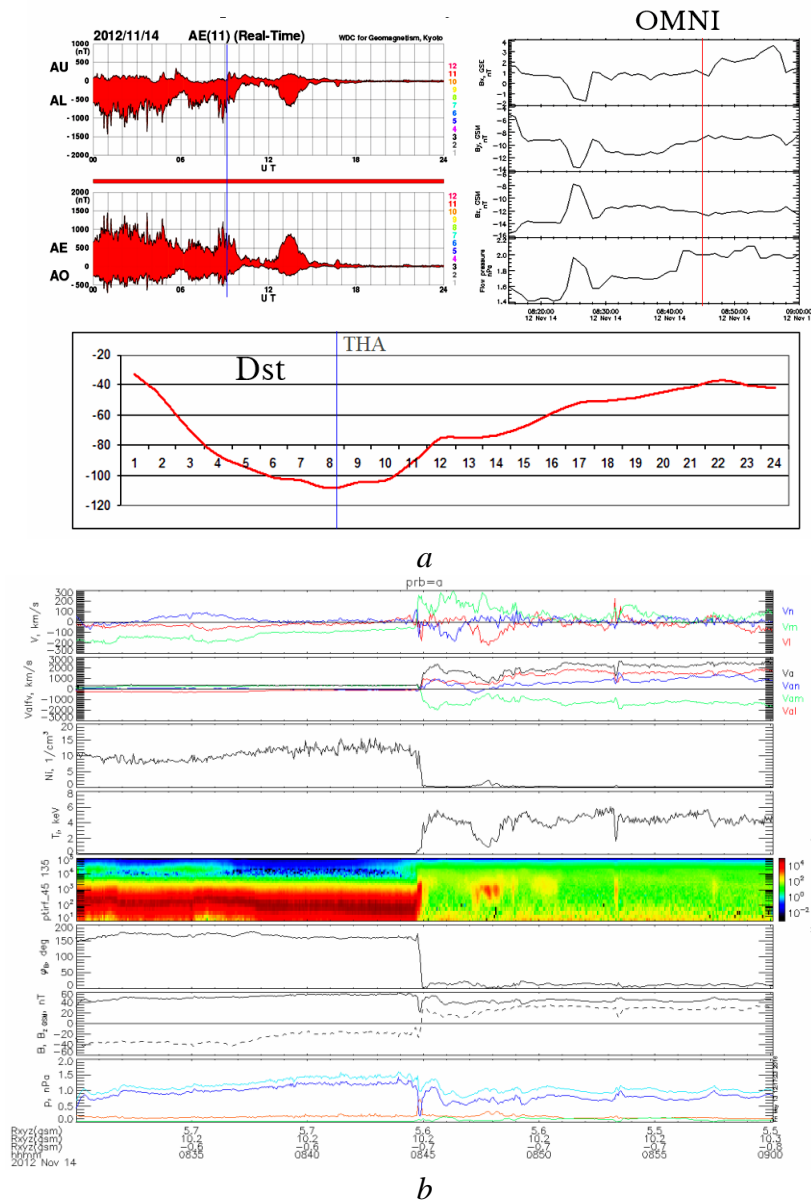


Fig.42. Variations in the geomagnetic indices AU, AL, AE, AO and Dst during the storm of November 14, 2012 (a); Changes in the plasma parameters and magnetic field at the half-hour interval near the maximum of the magnetic storm of November 14, 2012, from top to bottom: plasma flow velocity  $V$  along the LMN vectors (in km/s); local Alfvén velocity  $V_{alfv}$  along the LMN vectors (in km/s); ion density  $N_i$  (in  $1/cm^3$ ); ion temperature  $T_i$  (in keV); ion spectrogram (along the vertical scale, the ion energy  $E_i$ , in eV); angle of turning of the magnetic field  $\phi_B$  (in degrees); magnetic field magnitude  $B$  and the magnetic field component  $B_z$  in the GSM system of coordinates (in nT); pressure of the plasma and magnetic field and the integrated pressure  $P$  (in nPa) (b).

Selected publication

M. S. Pulinets, I. P. Kirpichev, E. E. Antonova, Variations in plasma parameters and magnetic field upon magnetopause crossing at the main phase maximum of the magnetic

## 2.16. Studies of the low-latitude boundary layer of the Earth's magnetosphere (Skobeltsyn Institute of Nuclear Physics of Lomonosov Moscow State University)

The thickness of the low latitude boundary layer (LLBL) is studied as a function of interplanetary magnetic field (IMF) using the data of THEMIS mission. The data from intersections of LLBL by Themis-A and -C satellites are analyzed. Solar wind parameters are provided by Themis-B satellite located before the bow shock. The earlier developed method of LLBL thickness determination based on the analysis of the variation of plasma velocity in the layer perpendicular to the magnetopause is used. The database for the present analysis consists of 109 single satellite LLBL crossings where the values of LLBL thickness are obtained. The time shift of solar wind propagation from the spacecraft performing measurements outside the bow shock to the LLBL is taken into account. The dependence of LLBL thickness on IMF  $B_z$  and  $B_y$  is analyzed using data of IMF measurements with 3 s resolution and produce the 180 s averaging of these data. Large scattering of the values of LLBL thickness and the weak dependence on IMF is demonstrated. Dawn–dusk asymmetry of LLBL thickness is not observed. The dependence of LLBL thickness on IMF clock angle  $\theta_{Bn} = \tan^{-1}(B_y/B_z)$  is analyzed. A tendency to increase the thickness of the LLBL behind a quasi-parallel shock wave in the daytime part of the magnetosphere is observed.

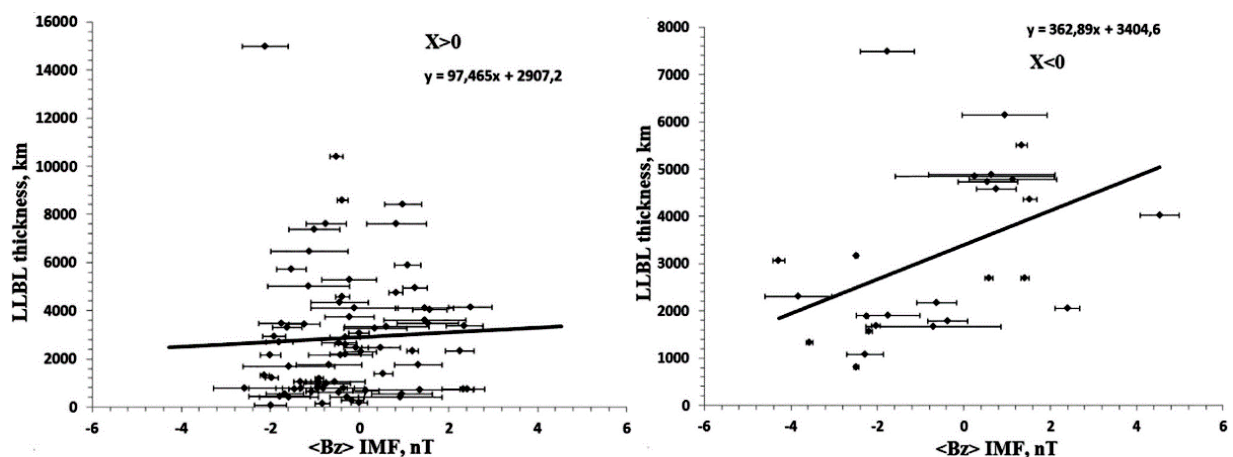


Fig.43. The dependence of LLBL thickness on IMF  $\langle B_z \rangle$  for the dayside and tail LLBL.

### Selected publication

Znatkova S. S., E. E. Antonova, M. S. Pulinets, I. P. Kirpichev, M. O. Riazantseva, The dependence of the LLBL thickness on IMF  $B_z$  and  $B_y$  components, *Advances in Space Research*, V. 58, p. 268–275, doi:10.1016/j.asr.2016.01.008, 2016.

## **2.17. The penetration of magnetospheric ions through the magnetopause**

(Skobeltsyn Institute of Nuclear Physics of Lomonosov Moscow State University)

The nature of energetic ions in the magnetosheath of the Earth is studied using the data of the Time History of Events and Macroscale Interactions during Substorms mission. Three intervals of the multiple crossings of the magnetopause during northward orientation of the interplanetary magnetic field and quiet geomagnetic conditions were selected to illustrate the behavior of ion distribution functions near the subsolar region in case of high and low magnetic shears. For all analyzed events, the velocity and thickness of the magnetopause was estimated using the simultaneous measurements in two satellites. The ion spectra in the magnetosphere and magnetosheath were fitted by kappa and bi-kappa distributions, respectively. An example of the results of observations is shown for large and small field shifts on the magnetopause and fitting of the ion spectra at the points indicated by the dotted lines in Fig.43. It was found that during high shear events the energetic part of the ion spectra is practically identical inside and outside the magnetopause. On the other hand, for low shear events the energetic fluxes of ions in the magnetosheath are lower. It is shown that in case of high magnetic shear, the magnetopause becomes transparent when the ion Larmor radii is comparable to or larger than the thickness of the magnetopause.

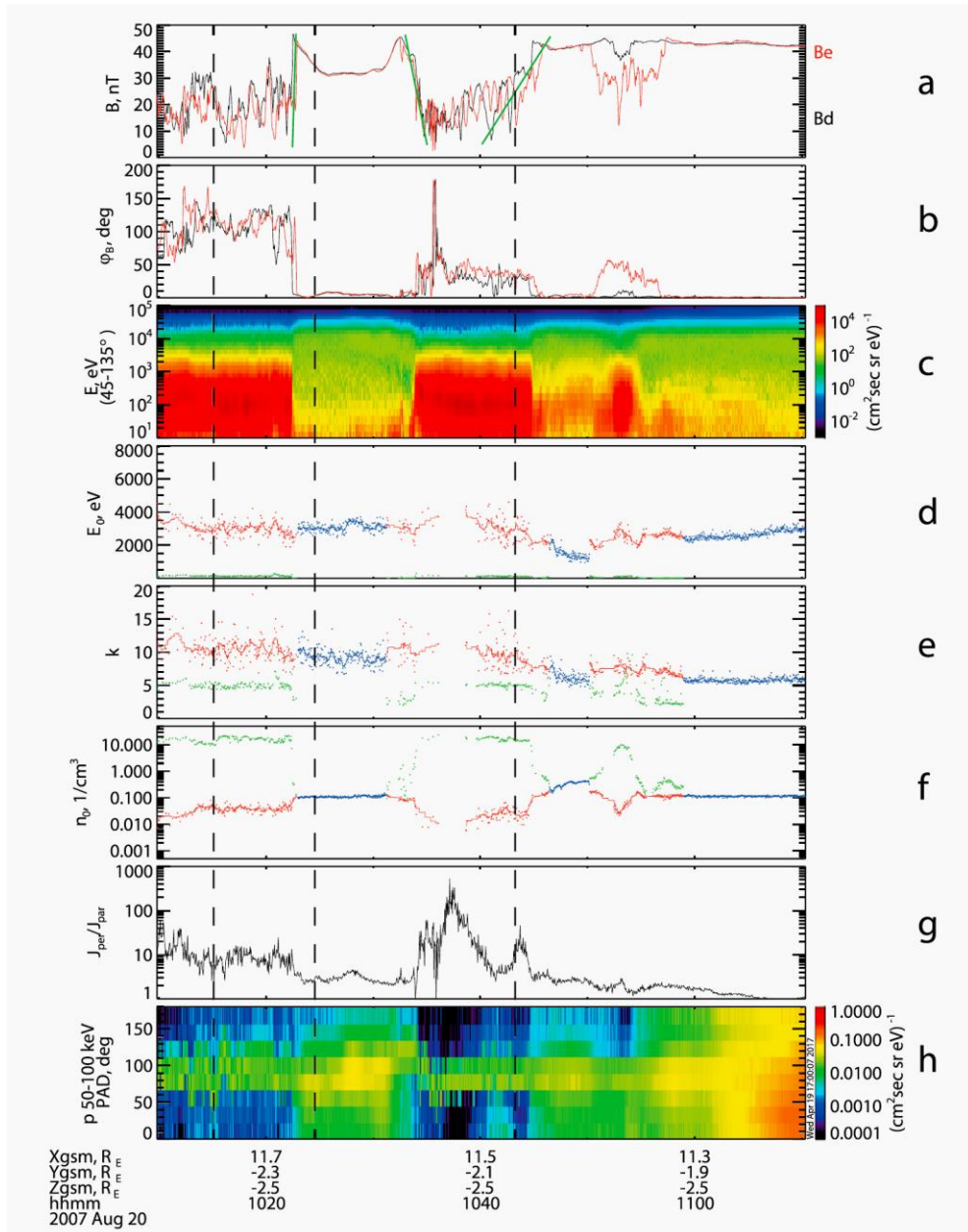


Fig.44. (a) The magnetic field measured by the THEMIS-E (red) and THEMIS-D (black) spacecrafts; (b) the magnetic declination angle of the magnetic field, measured by the THEMIS-E (red) and THEMIS-D (black) spacecrafts; (c) the differential ion fluxes measured in the pitch angle interval 45–135 ° ; (d) the characteristic energy; (e) and (f) ion number density obtained by fitting the differential ion fluxes with kappa (blue) and bi-kappa (red and green) distributions; (g) a ratio between integral fluxes of ions with energies between 50 and 100 keV perpendicular (45–135 ° ) and parallel (0–45 ° and 135–180 ° ) to the magnetic field; and (h) the pitch angle distributions for ions with energies in the range 50–100 keV. All parameters were measured on August 20, 2007. The green lines show linear fits of the magnetic field strength and indicate the main trends during the magnetopause crossings in each case.

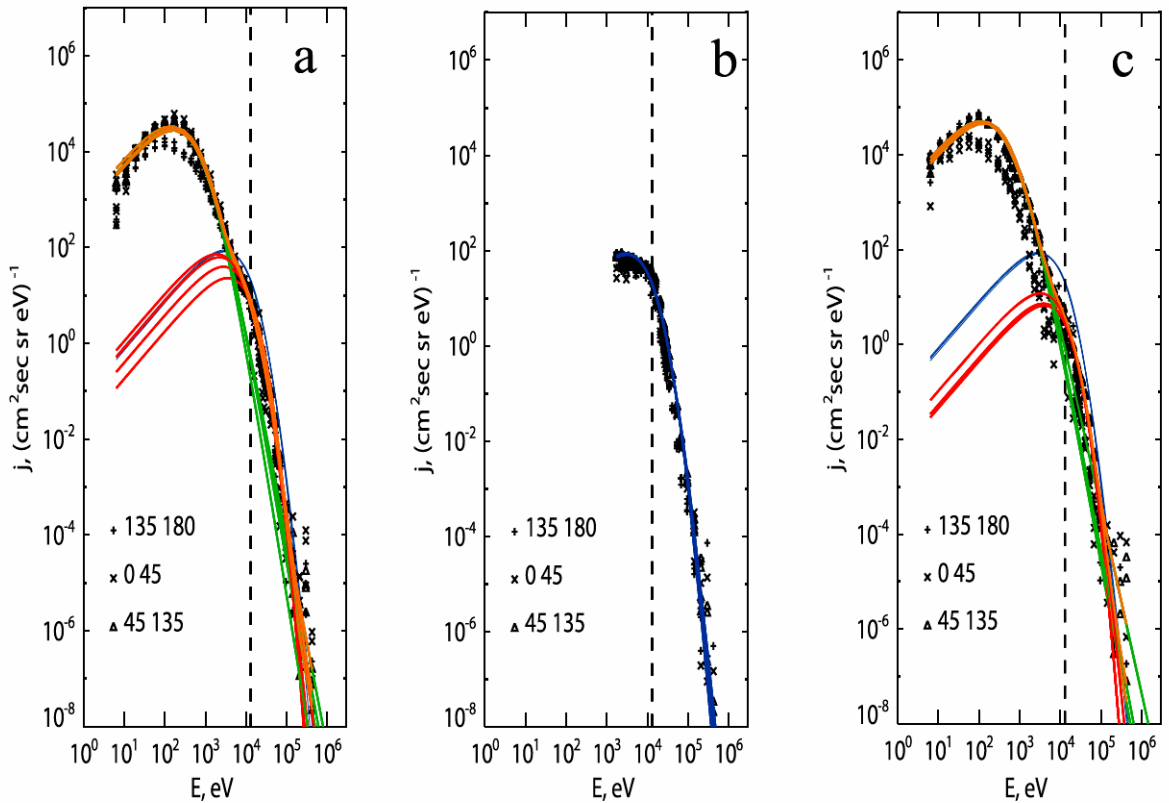


Fig. 45. Ion differential fluxes in three pitch angle intervals, fluxes measured between on August 20, 2007 (a) between 10:15:01 and 10:15:13; (b) between 10:24:14 and 10:24:26 and (c) between 10:43:15 and 10:43:27.

#### Selected publication

Kirpichev, I. P., E. E. Antonova, and M. Stepanova (2017), Ion leakage at dayside magnetopause in case of high and low magnetic shears, *J. Geophys. Res. Space Physics*, 122, doi:10.1002/2016JA023735

## 2.18. Jovian electrons and interplanetary magnetic field structure

(Skobel'syn Institute of Nuclear Physics of Lomonosov Moscow State University)

Jupiter is the source of the electrons of the MeV's energies constantly emitted into the surrounding space and propagating in the inner heliosphere. The propagation of Jupiter's electrons in space is determined by the structure of the magnetic field of the inner heliosphere (in the space between the Earth and Jupiter). The most favorable for their registration moments of optimal magnetic coupling between the Earth and Jupiter, in periods of quiet Sun, in minima of solar activity, when the magnetic field and solar wind retain their structure for a long time. However, sometimes Yu-electrons are recorded near the Earth at each rotation of the Sun, even in the absence of direct communication.

Jupiter, during the minimum of solar activity in 1974-75 Jovian electrons (J-electrons) were observed in 13 successive revolutions of the Sun, in 2007-08 - in 14 revolutions. During these periods, the location of the Earth and Jupiter varies greatly and in order to explain the constant arrival of J-electrons to the Earth, a hypothetical possibility of magnetic traps in the interaction of multi-velocity flows of solar wind was considered. Magnetic traps as they rotate together with the Sun contribute to the transfer of J-electrons from Jupiter to the Earth at different positions of the Earth and Jupiter.

The measurements have shown that the fluxes of these electrons in each solar rotation experienced quasi-27-days variations. The peculiarity of these variations was that their average period did not coincide with the synodic period of the Sun-Earth system, equal to 27.3 days. In 1974-75 the average period of electron flux variations was 26.8 days, and in 2007-08–26.2 days. The explanation of this effect is found by taking into account the changes in the structure of solar wind velocities and associated magnetic traps in time, as well as the influence of the mutual “the Earth – the Jupiter” arrangement in space, and the time of their stay in the magnetic trap.

*Selected publication*

*Daibog E. I., Kecskemeti K., Lazutin L. L., Logachev Yu. I., Surova G. M. 27-day periodicity of the Jupiter electron fluxes in Earth orbit. The astronomical journal, publishing house Nauka (Moscow), vol. 94, no. 12, pp. 1062-1070, 2017.*

## **2.19. Transient luminous events observations on board Lomonosov satellite**

(Skobeltsyn Institute of Nuclear Physics of Lomonosov Moscow State University)

The TUS detector on board Lomonosov satellite measured numerous UV transient flashes in the EAS mode with different temporal dynamics and spatial structure. The most common type of TLEs with a specific geometry - bright expanding ring to a maximum radius of ~300 km - in the ionosphere (altitudes of 80-90 km) are so-called elves. A number of such events were measured by the TUS detector. An arc-like shape of the track made by the brightest PMTs (Fig.49.) and the speed of development support the hypotheses that this was an elve. Waveforms of several pixels and the geographical location of the event are shown in Fig.48.



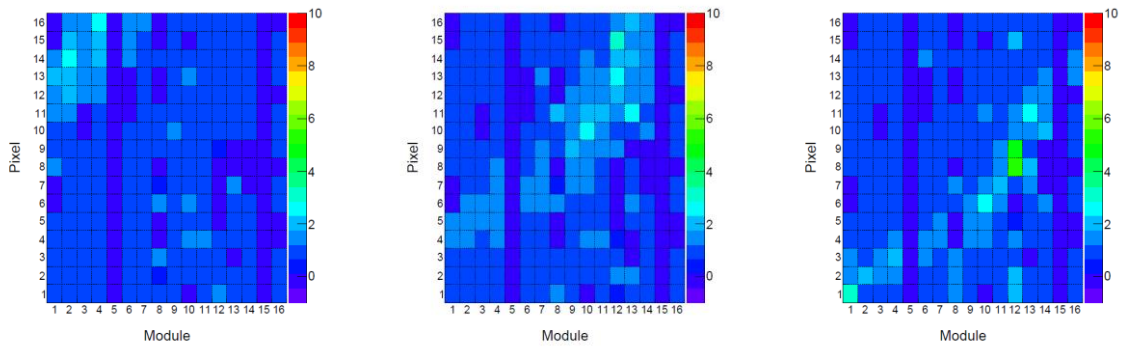


*Fig. 48. Snapshots of the focal plane show arc-like shape and movement of the object through the detector's field of view. The snapshots were taken at  $t = 0.077$  ms,  $0.182$  ms, and  $0.174$  ms from the beginning of the record. Colors denote the signal amplitude in arbitrary units scaled to individual PMT gains.*

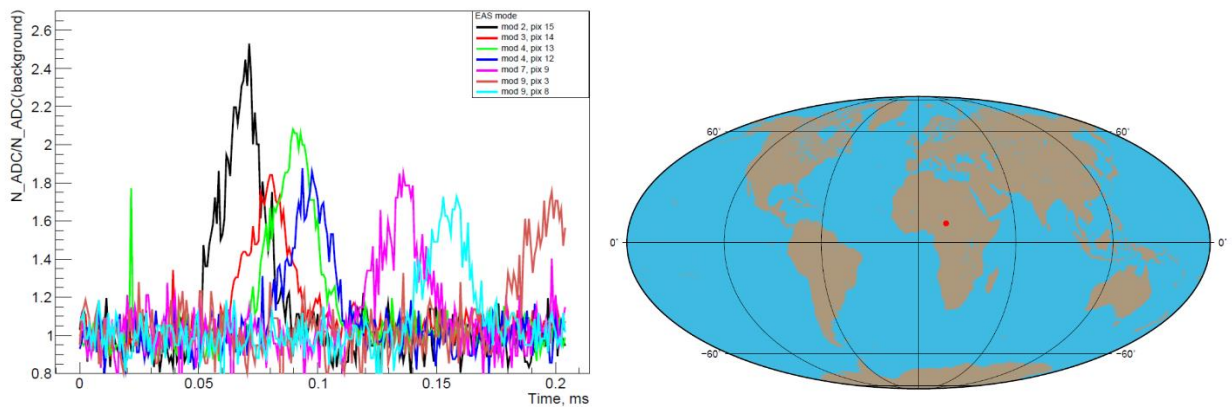


*Fig. 49. Waveforms of several hit pixels and geographical location of the elve event registered on September 18, 2016, above Africa. The Y-axis is a ratio of ADC counts and background signal for each pixel.*

Several hundred of events were measured by the TUS detector in the TLE mode. Most of them represent huge flashes related to thunderstorm activity. an example measured on June 27, 2016, above India is presented here. It occurred in the field of view and produced a huge signal: several pixels in the center of the event are saturated, see Figs. 49 and 50.

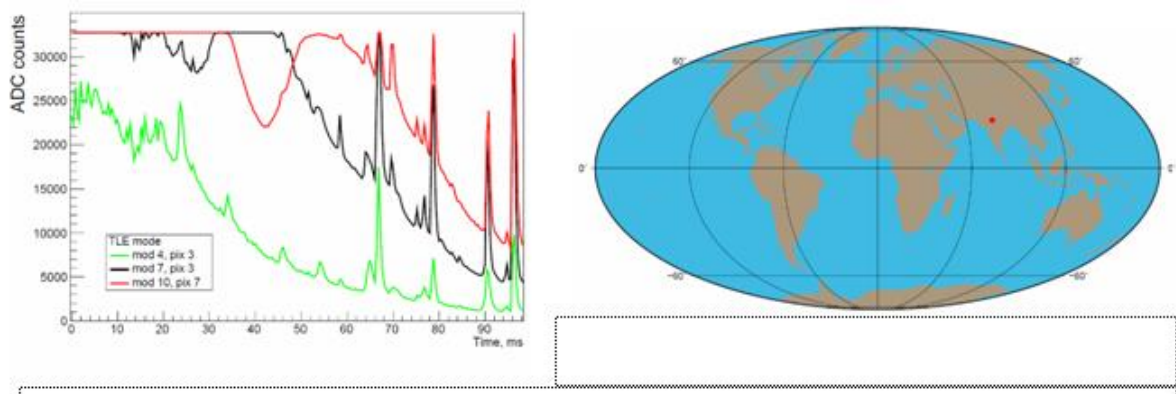


*Fig. 50. Waveforms of three pixels and the geographical location of the event registered on June 27, 2016, above India ( $25^{\circ}.3S$ ,  $77^{\circ}.8E$ ).*

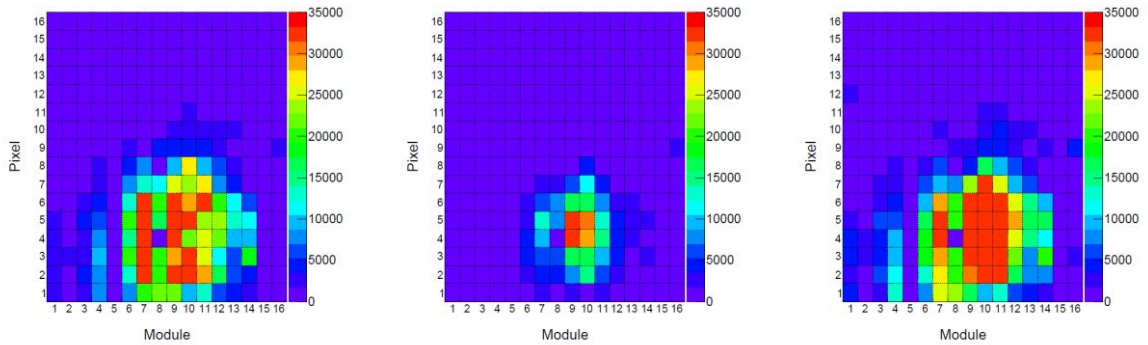


*Fig. 51. Snapshots of the focal plane. Snapshots were made at  $t = 40$  ms, 88 ms, 96.4 ms from the beginning of the record. Colors denote real ADC counts.*

A comparison with Vaisala Global Lightning Dataset GLD360 was made for this event as well. Several lightning strikes were found in this region for the time of the TUS measurements and two of them (negative cloud-to-ground) took place exactly in the FOV. The METEOR mode of the TUS operation has  $\sim 6.6$  ms temporal resolution and it allows to record digital oscillograms of 1.7 s length. This was implemented for measurements of much slower than EASs and TLEs processes and it is suitable for registering of meteors, thunderstorms, atmospheric airglow and city lights.

During the month of operation in this mode a dozen of meteors were measured. One of them is presented in the Fig.51. The speed of the meteor in assumption of its horizontal movement in the TUS FOV is  $\sim 50$ -60 km/s. The meteor was registered on January, 3, 2017, at 14:31:08 UTC. This time is close to the Quadrantids meteor shower peak in 2017.

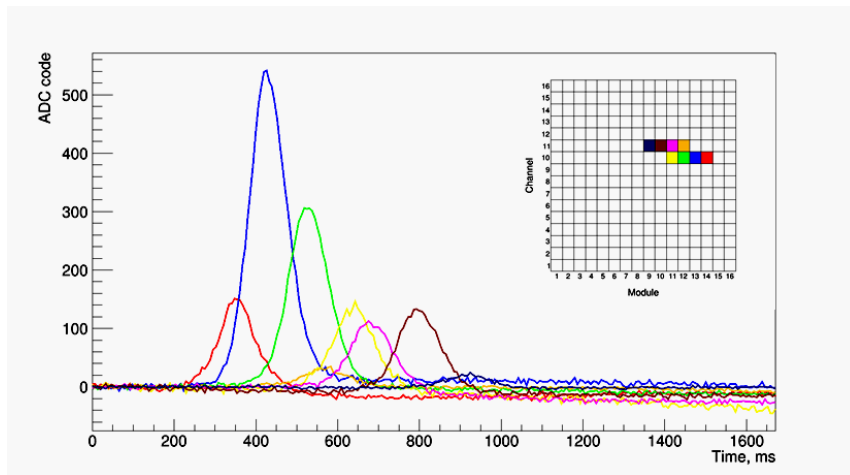


Fig.52. Waveforms  
of active pixels of the meteor event, measured on January 3, 2017 at 14:31:08 UTC.

### Selected publications

*P. Klimov, B. Khrenov, S. Sharakin, M. Zotov, N. Chirskaya, V. Ereemeev, G. Garipov, M. Kaznacheeva, M. Panasyuk, V.L. Petrov, A.V. Shirokov and V. Yashin. First results on transient atmospheric events from tracking ultraviolet setup (TUS) on board the Lomonosov satellite. Proceedings of International Symposium Thunderstorms and Elementary Particle Acceleration (TERA-2016), p. 122-127, 2017.*

*Klimov Pavel and Lomonosov-UHECR/TLE Collaboration the. Ultra-high energy cosmic ray detector TUS: preliminary results of the first year of measurements. In Proceedings of Science (35th International Cosmic Ray Conference), page PoS(ICRC2017)1098, 2017.*

*.P. A. Klimov for the Lomonosov-UHECR/TLE collaboration, UV atmospheric transient events measured by the TUS detector on board Lomonosov satellite with high temporal resolution, Proceedings of VERSIM Workshop, 19-23 March, 2018, Apatity, Russia*

## 2.20. Detection of global phenomena of technogenic and natural ultraviolet and infrared nightglows onboard VERNOV spacecraft

(Skobeltsyn Institute of Nuclear Physics of Lomonosov Moscow State University)

The generation of transients in the Earth's upper atmosphere under the action of electron fluxes and high- and low-frequency electromagnetic waves has been studied onboard the small VERNOV spacecraft (solar synchronous orbit, 98° inclination, altitude of 640–830 km). The studies were carried out with ultraviolet (UV, 240–380 nm), red–infrared (IR, 610–800 nm), gamma-ray (0.01–3 MeV), and electron (0.2–15 MeV) detectors as well as with high-frequency (0.05–15 MHz) and low-frequency (0.1 Hz–40 kHz) radio receivers. A number of UV flashes (lightning discharges and transient luminous events (TLEs)) were observed in thunderstorm regions. Examples of UV flashes with different temporal profiles are presented in Fig.53. Their geographical distribution is shown in Fig. 54.

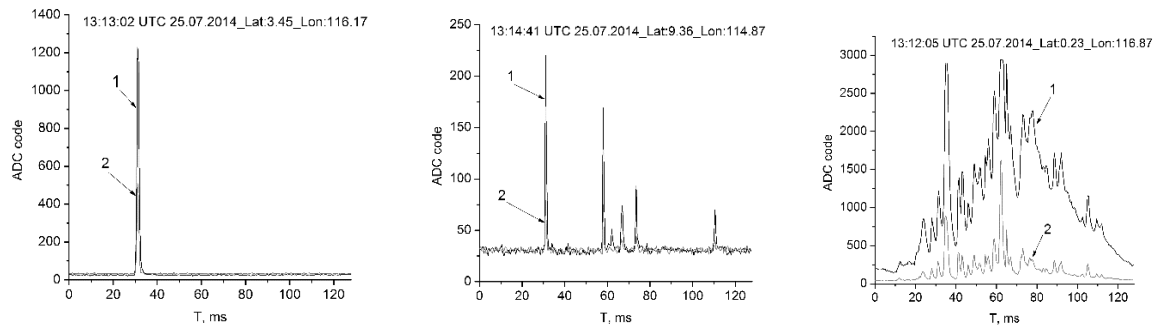


*Fig. 53. Examples of UV flashes time profiles used as typical in the analysis of VERNOV data. Lines 1 are profiles in the UV band, and lines 2 are profiles in the R-IR band.*

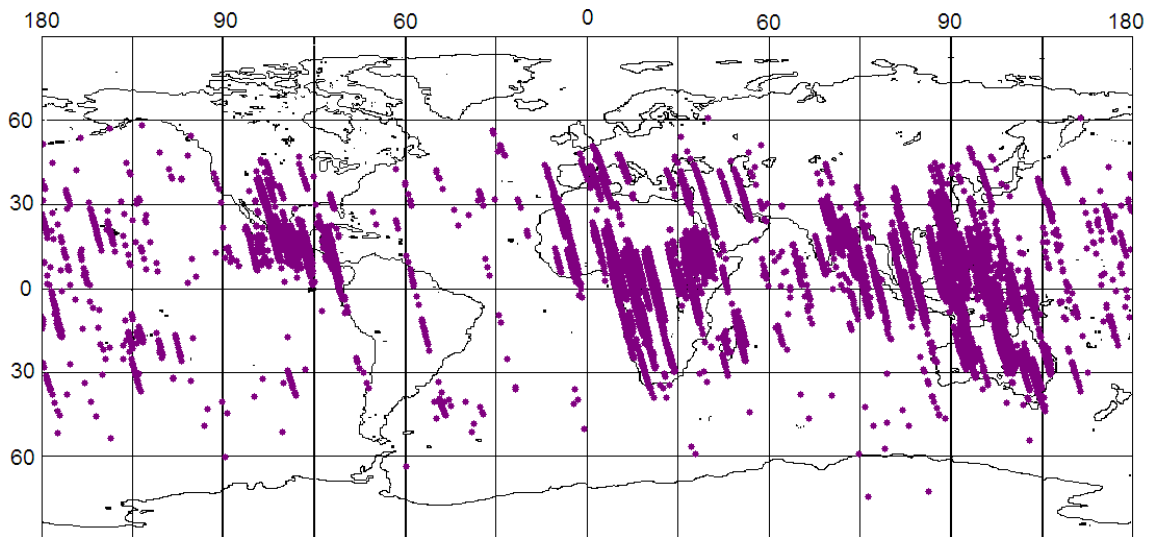


*Fig. 54. Map of UV transient flashes as observed in the VERNOV experiment.*

In an active thunderstorm region, a series of TAEs is expected as events are initiated by independent lightning, which is numerous in such a region. Because from VERNOV data, it became clear that the series are not only long in time (up to 10 min) but are frequent enough for filling a 1-min period with transients, measured every 4.5 s. Example of the TAEs in a series, observed in the VERNOV experiment, are represented in Fig. 55.

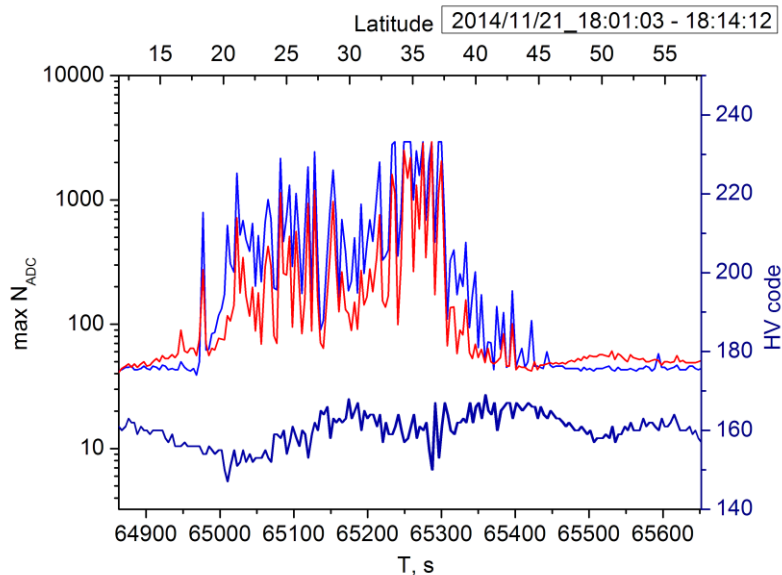


Fig.55. Example of transient series in UV (blue line) and R-IR (red line) radiation as measured by VERNOV. The lines are the result of the measurement in ADC code of the maximum signal obtained in period  $T=4.5$  s in a 0.5 ms time sample. The bottom black line is the high voltage code, which controls the PMTs gain.

Artificial optical signals distributed along the meridian in an extended region of latitudes in the Earth's Northern and Southern Hemispheres modulated by a low frequency were recorded during the nadir observations at nighttime. Examples of the oscillograms of such signals in the UV and IR spectral ranges are presented in Fig. 53. In this case, the modulation frequency changed abruptly approximately from 150 to 250 Hz. The UV and IR emissions are seen to be recorded in antiphase with a time shift of about 3 ms, which may be a consequence of the excitation of IR and UV nitrogen lines in the ionosphere. Source of the technogenic signal is a process in the atmosphere with a luminescence time of less than 1 ms, because the shortest rise and fall time of the oscillation pulses shown in the figures is 1 ms.

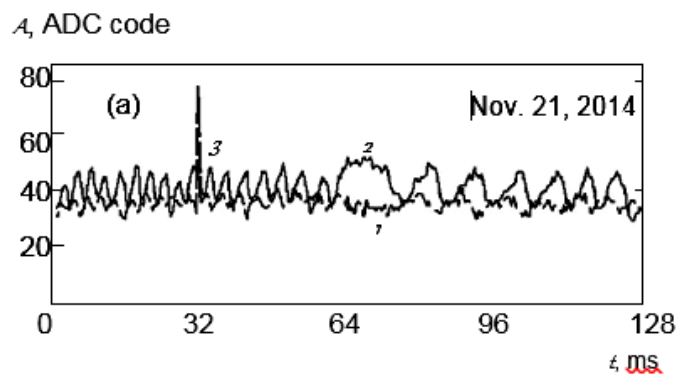


Fig. 56. Example of the oscillogram of a TLE pulse and a technogenic signal as the modulation frequency changes abruptly approximately from 150 to 250 Hz. The IR signal oscillation amplitude exceeds considerably the UV signal modulation.

Fig. 56 present map of the geographic distribution of technogenic glow recorded in one day, on September 5, 2014. The signals were recorded in each turn on the Earth's night side in the entire range of night-sky illuminances, from the South Pole during a southern polar night till the instant the satellite emerged on the sunlit side of the orbit in the Northern Hemisphere for about 28 min. In each 4.5-s time interval, starting from the pulses generated by atmospheric background fluctuations, the brightest flash was selected and recorded in the form of an oscillogram with a duration of 128 ms.

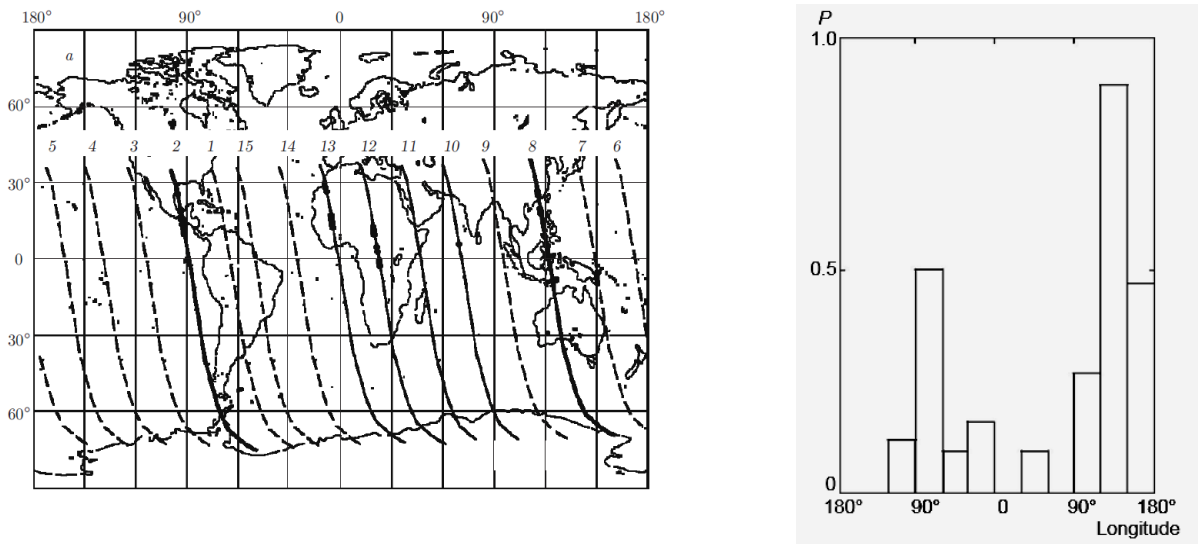


Fig. 57. Left panel. Example of the geographic distribution of satellite trajectories (dashed lines) and technogenic airglow (dots) on the night side of the orbit on September 5. Right panel. Probability of recording a technogenic glow versus longitude.

Right panel of Fig. 57. presents the probability distribution for the observation of technogenic signals as a function of longitude. These signals are seen to have been recorded most frequently at longitudes corresponding to Australia and North America.

Based on the rise and fall times of the recorded signals, one can conclude that the glow of molecular nitrogen ions is mainly recorded. In this case, based on the ratio of the IR and UV emission intensities, we showed the technogenic glow to be observed at nighttime at altitudes above 100 km. There is no transmitter carrier frequency in the recorded signals, although the detector has no detecting properties, and the modulation frequency of the transmitting station may be detected in the ionosphere as a result of nonlinear processes. UV and IR signals are shifted in time and are occasionally recorded in antiphase, which is also caused by the processes in the ionosphere, not by the detector properties. The longitude distribution of technogenic glows was shown to coincide with the distribution of the most powerful LF radio stations in a wide longitude band.

### *Selected publications*

1. «Experiment on the Vernov satellite: Transient energetic processes in the Earth's atmosphere and magnetosphere. Part II. First results», Panasyuk, M. I.; Svertilov, S. I.; Bogomolov, V. V., and 42 co-authors, *Cosmic Research*, Volume 54, Issue 5, pp.343-350 (09/2016)
2. «Experiment on the Vernov satellite: Transient energetic processes in the Earth's atmosphere and magnetosphere. Part I: Description of the experiment », Panasyuk, M. I.; Svertilov, S. I.; Bogomolov, V. V., and 42 co-authors, *Cosmic Research*, Volume 54, Issue 4, pp.261-269 (07/2016)
3. «Observation of TGFs onboard "Vernov" satellite and TGEs in ground-based experiments”, Bogomolov, Vitaly; Panasyuk, Mikhail; Svertilov, Sergey; and 9 co-authors, *EGU General Assembly 2016, held 17-22 April, 2016 in Vienna Austria*, p.8476 (04/2016).
4. «RELEC mission: Relativistic electron precipitation and TLE study on-board small spacecraft”, Panasyuk, M. I.; Svertilov, S. I.; Bogomolov, V. V., and 47 co-authors, *Advances in Space Research*, Volume 57, Issue 3, p. 835-849, (02/2016).
5. “Detection of global phenomena of technogenic ultraviolet and infrared nightglows onboard the Vernov satellite”, Garipov, G. K.; Panasyuk, M. I.; Svertilov, S. I.; Bogomolov, V. V.; Barinova, V. O.; Saleev, K. Yu., *Journal of Experimental and Theoretical Physics*, Volume 123, Issue 3, pp.403-410 (09/2016).
6. P. A. Klimov, G. K. Garipov, B. A. Khrenov, V. S. Morozenko, V. O. Barinova, V. V. Bogomolov, M. A. Kaznacheeva, M. I. Panasyuk, K. Yu Saleev, S. I. Svertilov. *Transient atmospheric events measured by detectors on the Vernov satellite. Izvestiya - Atmospheric and Oceanic Physics*, 53(9):924–933, 2017.
7. Pavel Klimov, Gali Garipov, Boris Khrenov, Violetta Morozenko, Vera Barinova, Vitaly Bogomolov, Margarita Kaznacheeva, Mikhail Panasyuk, Kirill Saleev, and Sergey Svertilov. *Vernov satellite data of transient atmospheric events. Journal of Applied Meteorology and Climatology*, 56(8):2189–2201, 2017.

## **2.21. Terrestrial Gamma-flashes measurements**

(Skobeltsyn Institute of Nuclear Physics of Lomonosov Moscow State University)

The RELEC scientific payload of the VERNOV satellite launched on July 8, 2014 includes the DRGE spectrometer of gamma-rays and electrons. This instrument comprises a set of scintillator phoswich-detectors, including four identical X-ray and gamma-ray detector with an energy range of 10 keV to 3 MeV with a total area of ~500 cm<sup>2</sup> directed to the atmosphere, as well as an electron spectrometer containing three mutually orthogonal detector units with a geometric factor of ~2 Cm<sup>2</sup> sr. The aim of a space experiment with the DRGE instrument is the study of fast phenomena, in particular Terrestrial gamma-ray flashes (TGF) and magnetospheric electron precipitation. In this regard, the instrument provides the transmission of both monitoring data with time resolution of 1s, and data in the event-by-event mode, with a recording of the time of detection of each gamma

quantum or electron to an accuracy of  $\sim 15\mu\text{s}$ . It provides a possibility for detailed analysis of the variability in the gamma-ray range, but also compare the time profiles with the results of measurements with other RELEC instruments (the detector of optical and ultraviolet flares, radio-frequency and low-frequency analysers of electromagnetic field parameters), as well as with the data of ground-based facility for thunderstorm activity. The catalogue of Terrestrial gamma-ray flashes was obtained. The example of time profile and even-by-event diagram for TGF 18.09.2014, 10:15:34 UTC are presented in Fig.58. The criterion for selecting flashes required in order to detect no less than 5 hard quanta in 1ms by at least two independent detectors. The TGF included in the catalogue have a typical duration of  $\sim 400\mu\text{s}$ , during which 10–40 gamma-ray quanta were detected. The time profiles, spectral parameters, and geographic position, as well as a result of a comparison with the output data of other VERNOV instruments, were obtained for each of candidates. One candidate for Terrestrial gamma-ray flash was detected in the near-polar region over Antarctica. Its nature is discussed now.

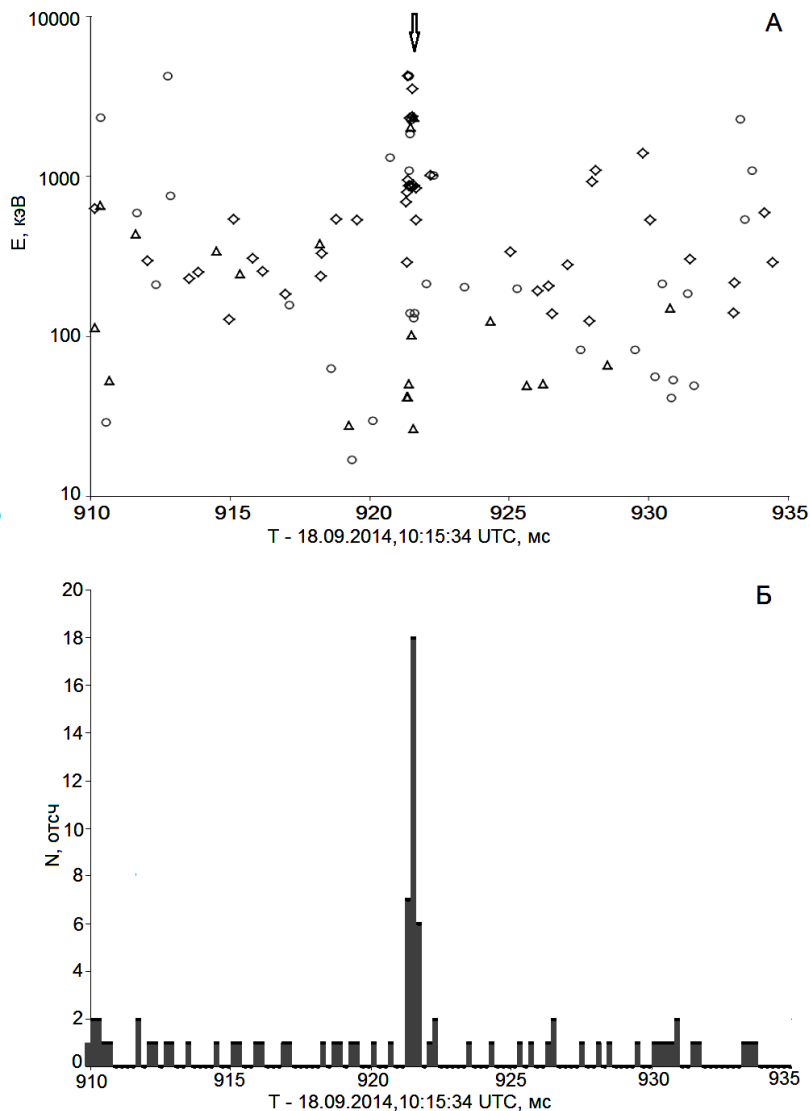


Fig.58. TGF 18.09.2014, 10:15:34 UTC.



*Selected publication*

*Observation of Terrestrial Gamma-Ray Flashes in the RELEC Space Experiment on the VERNOV Satellite. V. V. Bogomolov, M. I. Panasyuka, S. I. Svertilov, ISSN 0010-9525, Cosmic Research, 2017, Vol. 55, No. 3, pp. 159–168. © Pleiades Publishing, Ltd., 2017. DOI : 10.1134/S0010952517030017*

## 2.22. Radiation control of the Earth's environment at Space Monitoring Data Center SINP MSU



(Skobeltsyn Institute of Nuclear Physics of Lomonosov Moscow State University)

Space Monitoring Data Center (SMDC) of Moscow State University provides mission support for Russian satellites and gives operational analysis and forecasting of radiation conditions in space. SMDC Web-sites (<http://smdc.sinp.msu.ru/> and <http://swx.sinp.msu.ru/>) give access to current data about the level of solar activity, geomagnetic and radiation state of Earth's magnetosphere and heliosphere in the near-real time. The scientific models of space environment factors have been converted to operational engineering services. They are implemented as space weather Web-applications that provide forecasts of geomagnetic and radiation condition at given satellite orbits and in the whole magnetosphere:

- the solar wind forecast at L1 point. In this application, the velocities of recurrent high-speed streams are predicted for about of 3-day period based on the coronal holes parameters;
- forecast of the solar wind parameters and Interplanetary magnetic field (IMF) at the Earth's orbit; plasma and magnetic field measurements at L1 point are used as input for simple propagation model;
- the Dst index forecast in term of the perceptron type of artificial neural networks depending on solar wind measurements at L1 point;
- forecast of the fluxes of outer radiation belt relativistic electron with the energy greater than 2 MeV based on perceptron type of artificial neural networks (ANN).

All forecasts use the measurements collected at SMDC integrated database. Data obtained from GOES, ACE, Electro-L1, Electro-L2, Meteor-M1, Meteor-M2

spacecraft as well as images from the SDO satellite are used as inputs for SMDC operational services. Graphical applications (e.g. <http://swx.sinp.msu.ru/current.php?lang=en>) give opportunity to analyze simultaneously data from different sources. Radiation dose and SEE rate control along given spacecraft orbit are of special importance in a practical satellite operation. Satellites are always under the influence of high-energy particle fluxes during their orbital flight. The three main sources of particle fluxes: The Earth's radiation belts, the galactic cosmic rays, and the solar energetic particles, are taken into account by SMDC operational services to estimate the radiation dose caused by high-energy particles to a satellite at LEO orbits taking into account the geomagnetic cut-off depending on geomagnetic activity level. Complex analysis of the data "from Sun to Earth" obtained during disturbed period in the end of February 2014 has been carried out on the base SMDC data and facilities.

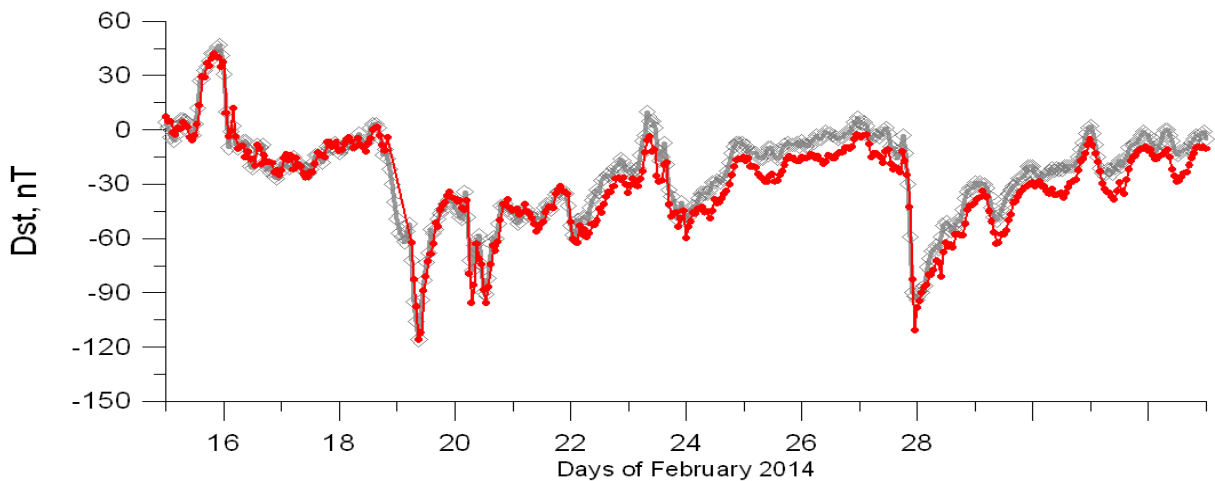


Fig. 68. *Dst* forecast (red) and *Dst* during 16.02-6.03.2014.

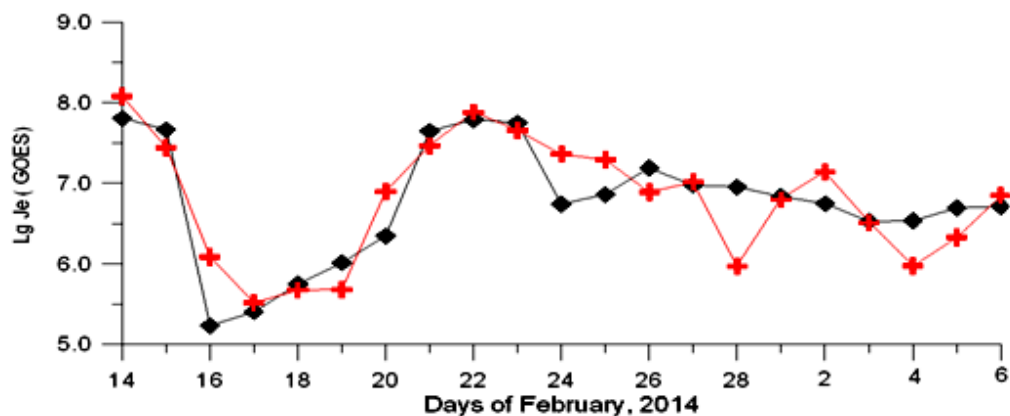


Fig.69. *SEP* fluxes measured by *Electro-L1* during 16.02-6.03.2014.

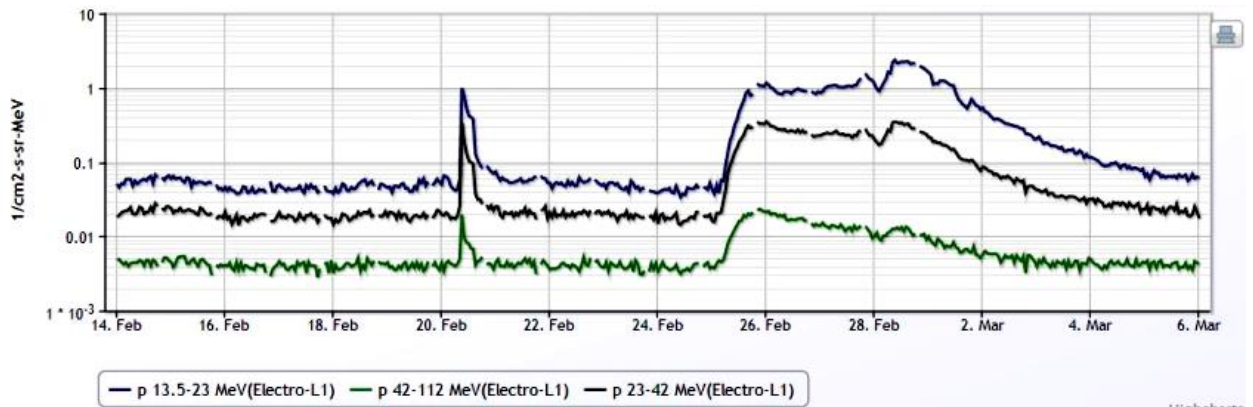


Fig.70. Outer Radiation belt fluences forecasting and GOES measurements (black) during 16.02-6.03.20.

**2.23. The work was continued on developing a new tool for early diagnostics of the geoeffectiveness of solar eruptions based on the magnetic flux from dimmings and post-eruption arcades. The procedure for transition from SOHO to SDO data was worked out.**

(Russian Academy of Sciences, Pushkov Institute of Terrestrial Magnetism, Ionosphere and Radio Wave Propagation (IZMIRAN))

The tool was developed by Chertok *et al.* and was described in (Solar Phys. **282**, 175, 2013 and **290**, 627, 2015; J. Phys.: Conf. Series, **409**, 012150, 2013). The authors analyzed the solar eruptions (Coronal Mass Ejections, CME) and the associated intense non-recurrent geomagnetic storms and Forbush decreases using data from the *Extreme-ultraviolet Imaging Telescope* (EIT) and MDI magnetograph onboard the Solar and Heliospheric Observatory (SOHO) for the period of Cycle 23 (1997–2006). Currently, respective solar observations are carried out with the AIA EUV telescope and HMI magnetograph on board the Solar Dynamic Observatory (SDO).

With the aim of further improvement of the tool and its application, in particular, at the IZMIRAN Space Weather Prediction Center, a comparison was made: (1) of the positions and forms of dimming and arcade areas extracted from SOHO and SDO images and (2) of the total unsigned line-of-sight photospheric magnetic fluxes measured with the MDI and HMI magnetographs in large active regions in the central zone of the solar disk. The data were compared for the period of SOHO and SDO joint observations in 2010–2011.

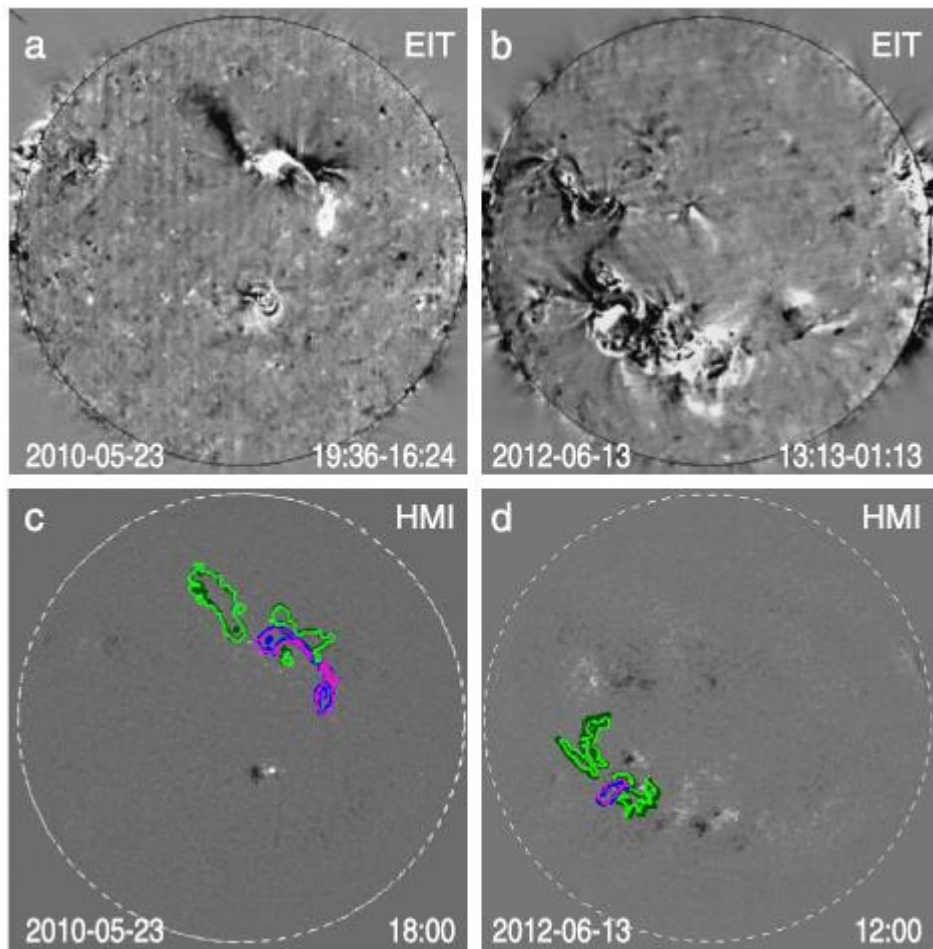


Figure 1. Top: bright post-eruption arcades and dark dimmings on SOHO/EIT 195 Å difference images for eruptions of 23 May 2010 (panel a) and 13 June 2012 (panel b). Bottom: corresponding SDO/HMI pre-event magnetograms (panels c and d) overlaid with the contours of extracted dimmings (dark green for AIA and light green for EIT) and arcades (blue for AIA and pink for EIT). The contours illustrate an acceptable correspondence between the areas selected from the images produced by the two instruments.

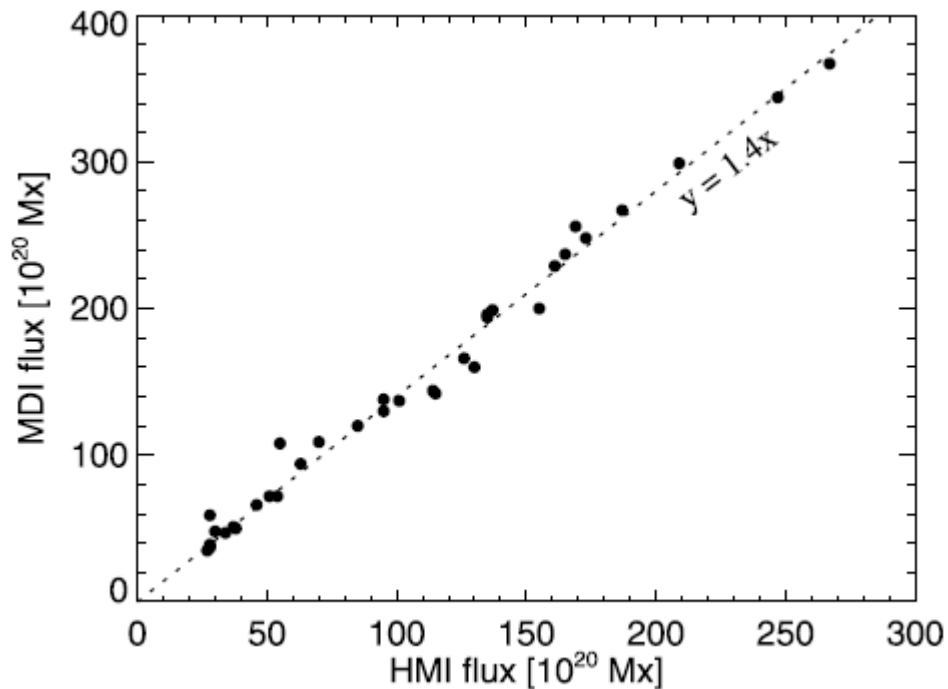


Figure 2. Relationship between the MDI and HMI magnetic fluxes of the largest ARs over the period from May 2010 to April 2011. The dotted line corresponds to  $\Phi_{\text{mdi}} = 1.4 \Phi_{\text{hmi}}$ .

It is established that: (1) with the previously accepted criteria and the correct consideration of differences in the EIT and AIA response, the coinciding dimming and arcade areas can be isolated on the corresponding images (Figure 1), and (2) the MDI magnetic flux systematically exceeds the HMI flux by a factor of 1.4 (Figure 2). It follows that for transition from the SOHO to SDO data it is sufficient to use the ratio  $\Phi_{\text{hmi}} = 1.4 \Phi_{\text{mdi}}$ .

Thus, the improved empirical relationships are obtained which allow the eruptive magnetic flux measured on SDO to be used to estimate the main parameters of the forthcoming space weather disturbances near the Earth, such as the intensity of non-recurrent geomagnetic storms (Dst and Ap indexes), the amplitude of Forbush decreases, as well as their onset and peak times, with a lead time from one to four days. Examples of such post-diagnostics of the largest eruptions in Cycle 24 are presented.

*Chertok I.M., Abunin A.A., Grechnev, V.V. An Early Diagnostics of the Geoeffectiveness of Solar Eruptions from Photospheric Magnetic Flux Observations: Transition from SOHO to SDO. Solar Physics, v. 292, No. 4, paper 62, 2017.*

<https://link.springer.com/article/10.1007%2Fs11207-017-1081-8>

<https://arxiv.org/abs/1702.05905>

**2.24. Routine measurements of solar soft X-rays on board the GOES series satellites during Cycles 21–24 revealed that the relationship between short-duration (SDE) and long-duration (LDE) flares does not change chaotically, but displays regular, stable “quasi-biennial” variations with an amplitude up to 30–40%.**

(Russian Academy of Sciences, Pushkov Institute of Terrestrial Magnetism, Ionosphere and Radio Wave Propagation (IZMIRAN))

GOES satellite data in the 1–8 Å range for Cycles 23 and 24 and part of Cycles 21 and 22 were used to compare the main temporal parameters (rise and decay times, duration) and the relative number of the impulsive (SDE) and gradual (LDE) flares of classes C and  $\geq M1.0$ .

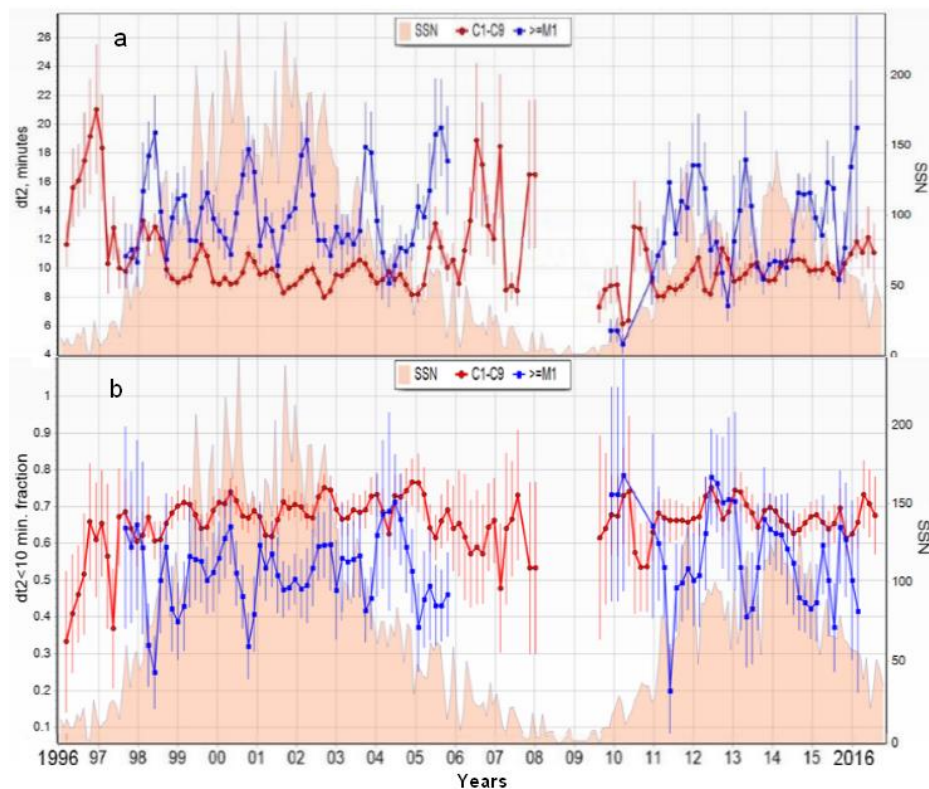


Figure 1. Variations in some parameters of the flares of classes C (red lines and circles) and  $\geq M1.0$  (blue lines and squares) against the monthly sunspot numbers (SSN) during Cycles 23 and 24: (a) the average decay time ( $dt_2$ ); (b) the relative number of SDE flares with  $dt_2 < 10$  min.

It is found, that the fraction of SDE flares of class  $\geq M1.0$  (including spikes) in Cycle 24 exceeded their fraction in Cycle 23 in all three temporal parameters at the cycle maximum and in the decay time, at the cycle ascending branch. As concerns SDE flares of class C, however, their fraction in Cycles 23 and 24 differs insignificantly. The temporal parameters of SDE, their fraction, and, consequently, the relationship between the SDE and LDE flares do not remain constant, but change regularly both within a particular cycle and from one cycle to another. In all phases of all four cycles, these changes have the form of pronounced large-

amplitude “quasi-biennial” oscillations (QBO). In different cycles and in different phases of a particular cycle, these QBO are superimposed on various systematic trends displayed by the analyzed temporal flare parameters. In Cycle 24, the fraction of SDE flares of class  $\geq M1.0$  in the N- and S-hemispheres displays the most pronounced synchronous QBO. The QBO amplitude and general variability of the intense flares of class  $\geq M1.0$  almost always exceeds markedly those of the moderate class C flares. These ordered quantitative and qualitative cycle variations in the type of flares are discussed within the framework of the concept that the SDE flares are associated mainly with small sunspots (including those in developed active regions) and that small and large sunspots behave differently during a cycle and form two distinct populations.

*Chertok I.M., Belov A.V. Long- and Mid-Term Variations of the Soft X-ray Flare Character in Solar Cycles. Solar Physics, v. 292, No. , paper 144, 2017. DOI: 10.1007/s11207-017-1169-1.*

<https://link.springer.com/article/10.1007%2Fs11207-017-1169-1>

<https://arxiv.org/abs/1710.06837>

<http://www.izmiran.ru/~ichertok/FlareVariations/preprint.pdf>

**2.25. The data of ground-based and satellite measurements taken during the outstanding burst of the solar flare activity in early September 2017 confirmed the qualitative and quantitative correspondence between the flux and frequency spectra of microwave radio bursts, on the one hand, and the intensity and energy spectra of protons with energies of tens of MeV coming to the Earth, on the other.**

(Russian Academy of Sciences, Pushkov Institute of Terrestrial Magnetism, Ionosphere and Radio Wave Propagation (IZMIRAN))

Intensive flares that occurred in the Sun during September 4–10, 2017 were analyzed using the technique developed at IZMIRAN in the 1970ies–1980ies for quantitative diagnostics of proton flares. It was shown that the fluxes and energy spectra of protons with energies of tens of MeV coming to the Earth correspond qualitatively and quantitatively to the intensity and frequency spectra of microwave radio bursts in the range of 2.7–15.4 GHz. For example, the flare of 4 Sept. with the peak radio flux  $S \sim 2000$  sfu at the frequency  $f \sim 3$  GHz (soft radio spectrum) was accompanied by a significant proton flux  $J (> 10 \text{ MeV}) \sim 100$  pfu and a soft energy spectrum with index  $\gamma \sim 3.0$ ; and the major flare of 10 Sept. with  $S \sim 21000$  sfu at  $f \sim 15$  GHz (hard radio spectrum) resulted in a very intense proton event with  $J (> 10 \text{ MeV}) \sim 1000$  pfu with a hard energy spectrum ( $\gamma \sim 1.4$ ), including a ground level enhancement (GLE72). This is another evidence that data on microwave radio bursts can be successfully used (in particular, with application of the IZMIRAN method) to diagnose proton flares, regardless of the specific source of particle acceleration on the Sun.

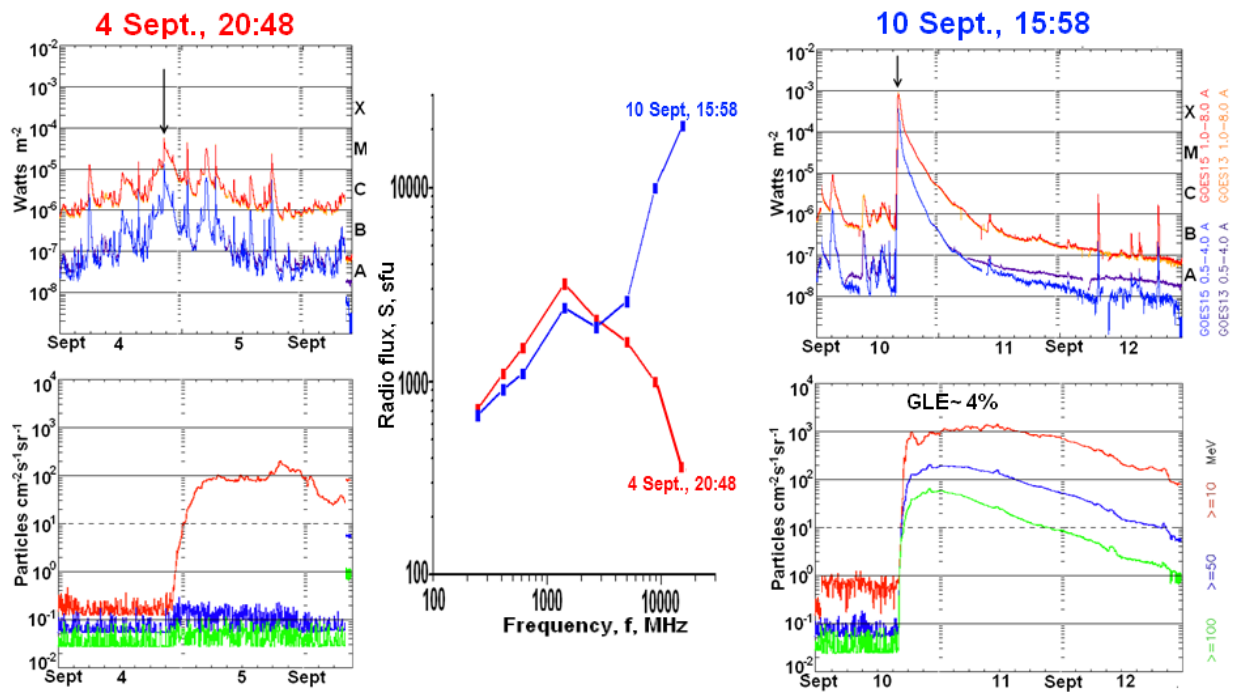


Fig. 1. Time profiles of soft X-ray flares and proton fluxes near the Earth for the post-eruption event of 4 Sept. 2017 with soft radio and energy spectra (left) and for the major long-duration flare of 10 Sept. 2017 with hard radio and energy proton spectra (right). The plot at the center is the frequency spectrum of microwave bursts from these two flares.

Chertok I.M. *Powerful Solar Flares of 2017 September: Correspondence between Parameters of Microwave Bursts and Proton Fluxes near Earth. Research Notes of the American Astronomical Society. V. 2. Id. 20. 2018. DOI: 10.3847/2515-5172/aaaab7*

<http://iopscience.iop.org/article/10.3847/2515-5172/aaaab7>

<https://doi.org/10.3847/2515-5172/aaaab7>

<https://arxiv.org/ftp/arxiv/papers/1802/1802.00191.pdf>

Chertok I.M. *Diagnostic analysis of solar proton flares of September 2017 by their radio bursts. Geomagnetism and Aeronomy, V. 58, No. 4, 2018.*

## 2.26. Analysis of the spatial electric field distribution over Alpha net transmitters based on Demeter satellite records.

(Russian Academy of Sciences, Pushkov Institute of Terrestrial Magnetism, Ionosphere and Radio Wave Propagation (IZMIRAN))

The spatial distribution of the electric field over three Alpha transmitters in Russia were analyzed using the DEMETER satellite records taken at local nighttime during the solar minimum in December 2008. The three transmitters had the same radiation power of 500 kW and emitted radio waves at the same frequencies of 11.9 kHz, 12.6 kHz, and 14.9 kHz. The results of observations showed that the maximum electric field reached A80 to A70 dB (hereafter referred to as V/m) at 670 km altitude. The horizontal covered area even exceeded 80° in longitude with



electric field above A100 dB at 14.9 kHz. The lowest electric field and the smallest longitude scale were detected over Krasnodar (KRA), which implied that the lower ionosphere plays an important role in attenuating the energy as suggested by the simulation results from the full-wave propagation model. Another particularity observed over KRA was a significant decrease in electromagnetic field strength at 11.9 kHz and 12.6 kHz, being one order of magnitude lower than the other two transmitters, where the lower hybrid resonance waves affected severely the whistler mode wave mode propagation.

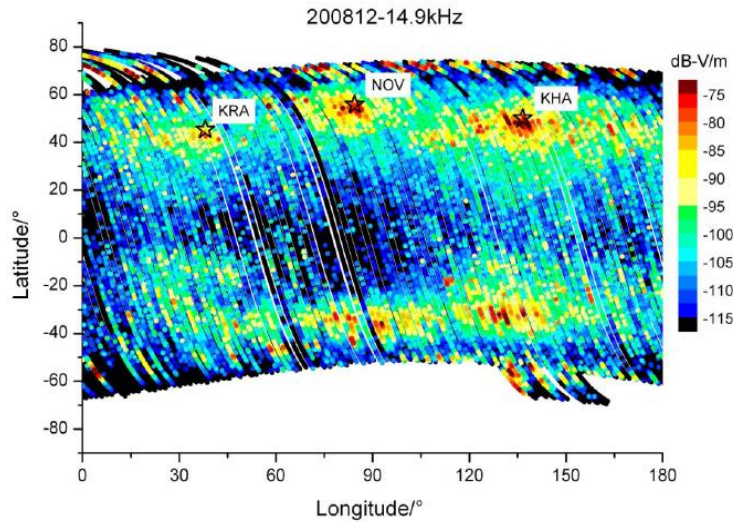


Figure 1. Spatial distribution of electric field at 14.9 kHz of three Alpha navigators (yellow stars) in the topside ionosphere in December 2008

Zhang, X., S. F. Zhao, Y. Ruzhin, J. Liu, and R. Song (2017). The spatial distribution features of three Alpha transmitter signals at the topside ionosphere. *Radio Sci.*, 52, 653–662, doi:10.1002/2016RS006219.

X. Zhang, S. F. Zhao, Y. Ruzhin, R. Song. The VLF emissions over Russian ALPHA transmitters by DEMETER observations. Abstracts 12th conference “Physics of plasma in the Solar system” IKI, Moscow, 6-10.02\_2017, P.283. <http://plasma2017.cosmos.ru>

## 2.27. SURA HF heating induced plasma perturbations analysis based on satellite records.

(Russian Academy of Sciences, Pushkov Institute of Terrestrial Magnetism, Ionosphere and Radio Wave Propagation (IZMIRAN))

Three typical plasma perturbations induced by SURA HF heating were selected and analyzed in detail using the DEMETER/ ISL and IAP observation data. Some common features were revealed: (1) both electron density and electron temperature increased during the heating period; (2) both O<sup>+</sup> density and ion temperature also increased, while H<sup>+</sup> varied negatively with O<sup>+</sup> density; (3) the ions moved upwards in the process of heating and were accelerated upward and northward from the thermal pressure gradient, which also caused the variations in ULF

electric field due to  $V \times B$  effects; (4) the results of simulation corroborate the enhancement of electron density and temperature in the topside ionosphere due to the ohmic heating and thermal self-focusing instability over the heating region, which is consistent with the phenomena observed on board the DEMETER satellite.

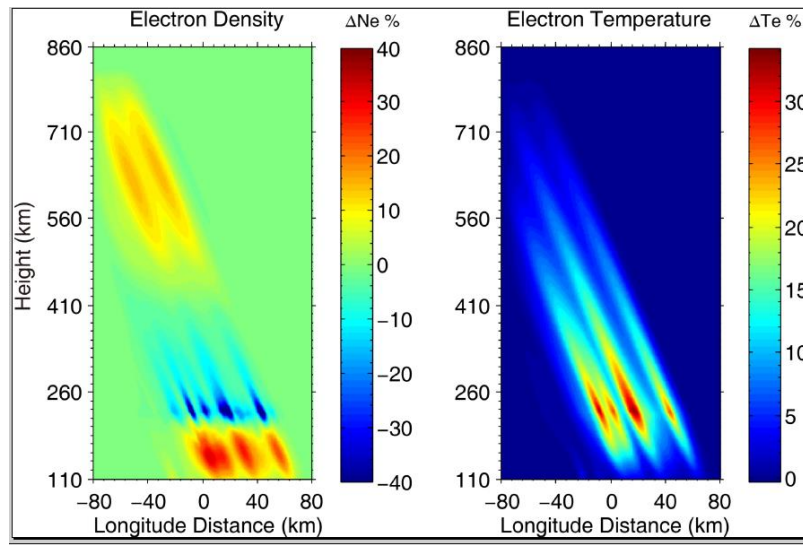


Figure 1. The numerical simulation of HF-induced Ne (a) and Te (b) perturbations at UT 18:16 on May 2008 over SURA facility.

Zhang, X., V. Frolov, C. Zhou, S. Zhao, Y. Ruzhin, X. Shen, Z. Zhima, and J. Liu (2016), Plasma perturbations HF-induced in the topside ionosphere, *J. Geophys. Res. Space Physics*, 121, doi:10.1002/2016JA022484

## 2.28. Satellite $f_oF2$ model in the high-latitude winter ionosphere of the North and South hemispheres

(Russian Academy of Sciences, Pushkov Institute of Terrestrial Magnetism, Ionosphere and Radio Wave Propagation (IZMIRAN))

A new precise empirical model of  $f_oF2$  in the high-latitude winter ionosphere of the North and South hemispheres was constructed. The data of topside sounding onboard the Interkosmos-19 satellite, radio-occultation data, and in-situ measurements onboard the CHAMP satellite were used. The new model covers the geographic latitude range of  $40-85^\circ$  and all hours of local time. It is valid for quiet geomagnetic conditions ( $K_p = 2$ ) and for all levels of solar activity in the range  $F10.7 = 70-200$ . The model covers the period from November to February in the North hemisphere and from May to August in the South hemisphere. The new model was the first to reproduce the structure of the ionospheric trough, its position and shape. Therefore, it can be effectively used to solve the task of high-latitude radio propagation. The new model describes  $f_oF2$  longitudinal and latitudinal variations in the winter ionosphere much more accurately than IRI 2016. Its on-line version is available for use on the IZMIRAN website:

<http://www.izmiran.ru/ionosphere/sm-mit/>. Fig. 1 shows an example of  $foF2$  distribution in the North hemisphere at 00 LT and 12 LT.

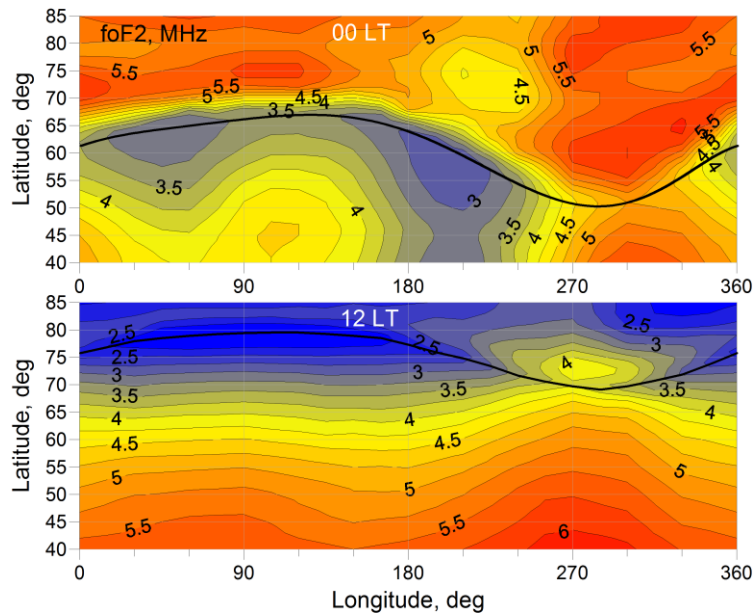


Figure 1. Distribution of  $foF2$  in the North hemisphere for HSA, 00LT (top) and for LSA, 12 LT (bottom). The thick black line shows the through minimum position.

*Karpachev A.T., Klimenko M.V., Klimenko V.V., Pustovalova L.V. Empirical model of the main ionospheric trough for the nighttime winter conditions. // J. Atmos. Sol-Terr. Phys. v.146, pp.149–159. doi:10.1016/j.jastp.2016.05.008. 2016.*

*Klimenko V.V., Karpachev A.T., Klimenko M.V., Ratovskii K.G., Korenkova N.A. Latitudinal structure of the longitudinal effect in the nighttime ionosphere during the summer and winter solstice // Russian J. of Physical Chemistry B, v.10, No 1, pp.91–99. 2016.*

## **2.29. Diurnal and Longitudinal Variations In the Structure of the Equatorial Anomaly During the Equinoxes According to Intercosmos-19 Satellite Data** (Russian Academy of Sciences, Pushkov Institute of Terrestrial Magnetism, Ionosphere and Radio Wave Propagation (IZMIRAN))

A comprehensive pattern of longitudinal and local-time variations in the structure of the equatorial anomaly (EA) at the equinox under high solar activity was obtained for the first time. The data of the Interkosmos-19 topside sounding were used. It was shown that the anomaly arises at 08 LT as the southern crest is formed. The development of EA is due to the change in the electric field direction from west to east, which causes a vertical plasma drift  $W$  (directed upward) and a fountain effect. At 10 LT, both anomaly crests appear, but they become completely

symmetric only by 14 LT. The mean position of the crests increases from  $I = 20^\circ$  at 10 LT to  $I = 28^\circ$  at 14 LT. The position of the crests changes significantly (sometimes up to  $15^\circ$ ) with longitude. The  $foF2$  value over the equator and the EA intensity (EAI) at 12–14 LT vary with longitude in accordance with the changing velocity of the vertical plasma drift  $W$ . At this time, four harmonics are observed in longitudinal variations of  $W$ ,  $foF2$ , and EAI. The EA intensity increases to the maximum 1.5–2 h after the evening burst in the vertical plasma drift velocity. The longitudinal variations in  $foF2$  in the period of 20–22 LT are also associated with corresponding variations in the vertical plasma drift velocity. The EAI decreases after the maximum at 20 LT, and the crests decrease in size and shift towards the equator, but the anomaly is still well developed at midnight. After the midnight, the  $foF2$  maxima in the region of the anomaly crests move away from the equator, but this is obviously associated with the action of the neutral wind. At 02 LT, in contrast to the morning hours, only the northern crest of the anomaly is clearly pronounced. Thus, at high solar activity during the equinoxes, a well-developed EA is observed from 10 to 24 LT. It reaches the maximum at 20 LT. Fig.4 shows an example of  $foF2$  variations during the development of EA.

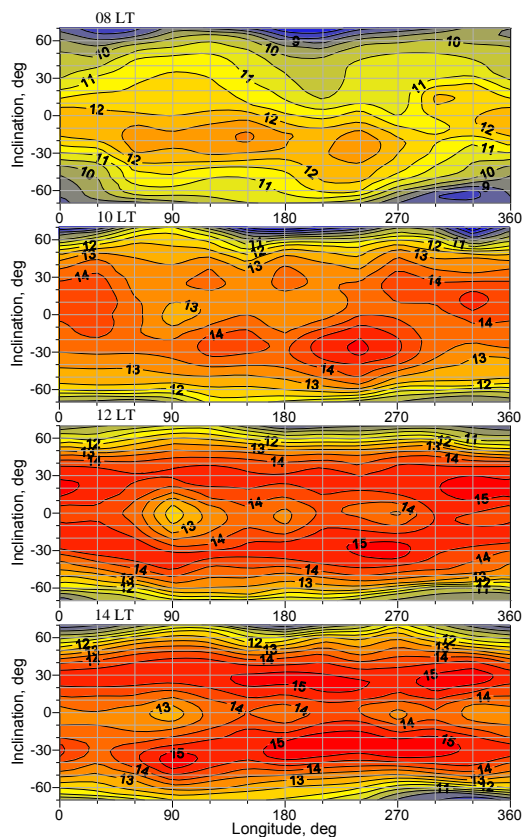


Figure 4. Distributions of  $foF2$  at the equinox during the development of equatorial anomaly for 08, 10, 12, and 14 LT.

*Karpachev A.T. Diurnal and longitudinal variations of the structure of an Equatorial Anomaly during equinoxes according to Interkosmos-19 satellite data // Geomagnetism and Aeronomy. v.58. No 3. pp. 407-419. 2018.*

### 2.30. The first observations of super plasma bubbles in Europe

(Russian Academy of Sciences, Pushkov Institute of Terrestrial Magnetism, Ionosphere and Radio Wave Propagation (IZMIRAN))

It is well known that ionospheric plasma bubbles of equatorial origin have never been recorded at mid latitudes in Europe. During the geomagnetic storm of 22–23 June 2015, the penetration of electric fields directly from high latitudes to the equator accompanied by the nighttime enhancement of equatorial zonal electric fields caused plasma bite-outs ( $\sim 15^\circ$ – $20^\circ$  in latitude) in the post-sunset sector over low latitudes of the West Africa and resulted in the occurrence of large-scale plasma bubbles extended along the magnetic field toward Europe. For the first time, super plasma bubble effects were recorded in Europe using multisite GPS and GLONASS observations ( $\sim 1500$  stations). They were observed during more than 8h (20–04 UT) and covered a broad area within  $30^\circ$ – $40^\circ$ N and  $20^\circ$ W– $10^\circ$ E. These unique results were confirmed by total electron content measurements on board the Swarm and DMSP satellites and by ground-based observations. The occurrence of super plasma bubbles in Europe affected the operation of the Global Navigation Satellite Systems in Spain, Portugal, southern France, and Italy and led to degradation of the European Geostationary Navigation Overlay Service.

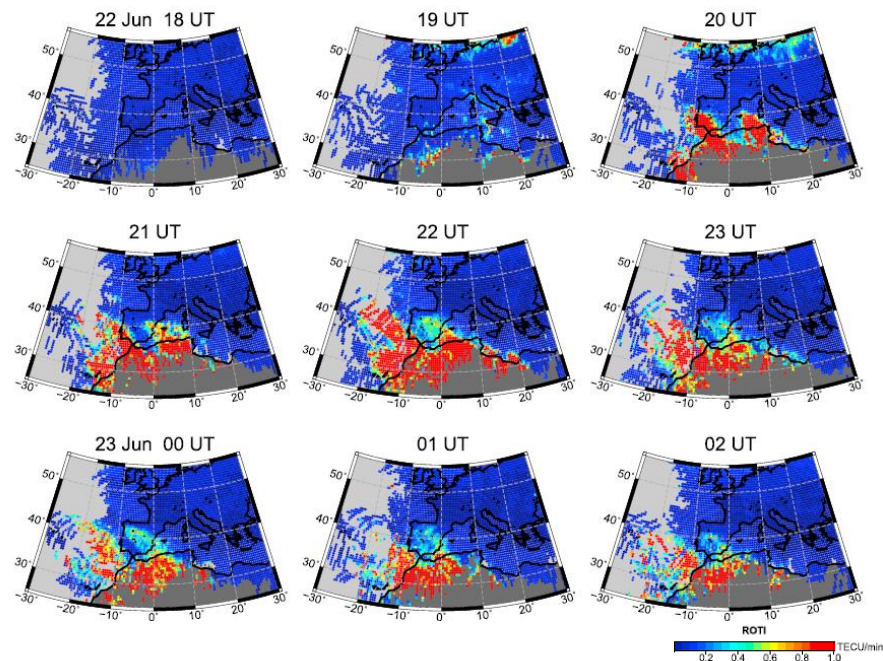


**Fig.1.** Two-dimensional maps of ROTI (Rate of TEC changes Index), constructed with the use of multi-station GPS and GLONASS observations over the European region for 22–23 June 2015. Red areas (high ROTI values) show the appearance and evolution of three plasma bubbles over the European territory.

*Cherniak, I., and Zakharenkova, I. (2016). First observations of super plasma bubbles in Europe. Geophys. Res. Lett. 43(21), 11137–11145. doi:10.1002/2016GL071421.*

### 2.31. Signatures of the Weddell Sea Anomaly in the ground-based and satellite-borne GPS TEC observations

(Russian Academy of Sciences, Pushkov Institute of Terrestrial Magnetism, Ionosphere and Radio Wave Propagation (IZMIRAN))

It is known that the Weddell Sea Anomaly (WSA) is a summer ionospheric anomaly, which is characterized by increased nighttime ionospheric density in the Weddell Sea region compared to the daytime values. The ionospheric signatures of WSA are mainly recorded at the F2-layer peak altitudes (200-300 km). We examined the WSA signatures in the topside ionosphere using GPS measurements with the aid of the zenith-looking GPS antenna on board three Swarm satellites to determine topside TEC (above ~500 km) in the topside ionosphere-plasmasphere system. Global maps of the topside TEC distribution show that the zone with a significant WSA effect (TEC increase by a factor of ~2-4 compared to the noon level) extends far over the Southern Pacific and Atlantic Oceans. For the first time, the WSA signatures were revealed in the topside TEC data derived from GPS measurements onboard the Swarm satellite constellation.

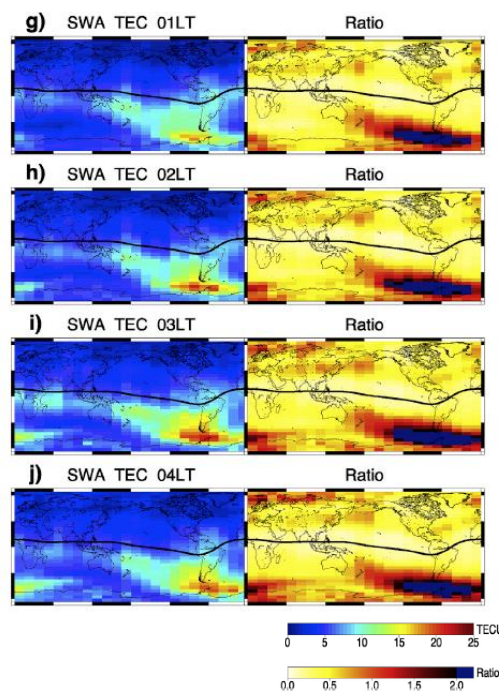


**Figure 1.** Global maps of the topside TEC values as derived from GPS observations onboard the Swarm A (SWA) satellite in the altitude range of 500-20000 km (left), and global maps of the normalized TEC (ratio to the noon-values) for specific night local times in December 2014-January 2015 (right). Ionospheric signatures of WSA are seen over the Southern Pacific close mainly to the South America.

Zakharenkova, I., Cherniak, I., & Shagimuratov, I. (2017). Observations of the Weddell Sea Anomaly in the ground-based and space-borne TEC measurements. *Journal of Atmospheric and Solar-Terrestrial Physics*, 161, 105–117.  
<https://doi.org/10.1016/j.jastp.2017.06.014>

### 2.32. Estimation of the efficiency of representing the topside total electron content with the NeQuick 2 and IRI-Plas empirical ionospheric models with plasmaspheric extension

(Russian Academy of Sciences, Pushkov Institute of Terrestrial Magnetism, Ionosphere and Radio Wave Propagation (IZMIRAN))

An adequate representation of the topside ionosphere by empirical ionospheric models is still an open question. New results were provided by a joint analysis of the total electron content (TEC) as inferred from GPS measurements on board the GOCE and TerraSAR-X satellites with the orbital altitudes of 250 km and 500 km, respectively, and calculated within two empirical ionospheric models with plasmaspheric extension: NeQuick 2 and IRI-Plas (developed at IZMIRAN). Two periods of low (2009/2010) and moderate (2012) solar activity were analyzed. The IRI-Plas model was found to overestimate the electron content in the altitude range of 250–500 km at low solar activity and the topside total electron content (TEC) at the altitudes of 500–20,000 km during the local daytime at low and moderate solar activity. The NeQuick 2 model demonstrates similar results in the altitude range of 250–500 km and opposite results, i.e., underestimated values for all seasons and local times under examination, at the altitudes above 500 km. The difference between the models is most significant within the altitude range of 500–2000 km. The observed underestimation of the topside TEC value in the NeQuick 2 model can be due to a simplified extension of the electron density profile toward the GPS orbit altitude without connection with a specific plasmasphere model. However, the plasmasphere model included into IRI-Plas leads to a noticeable overestimation of the TEC values derived from the space-borne GPS measurements.

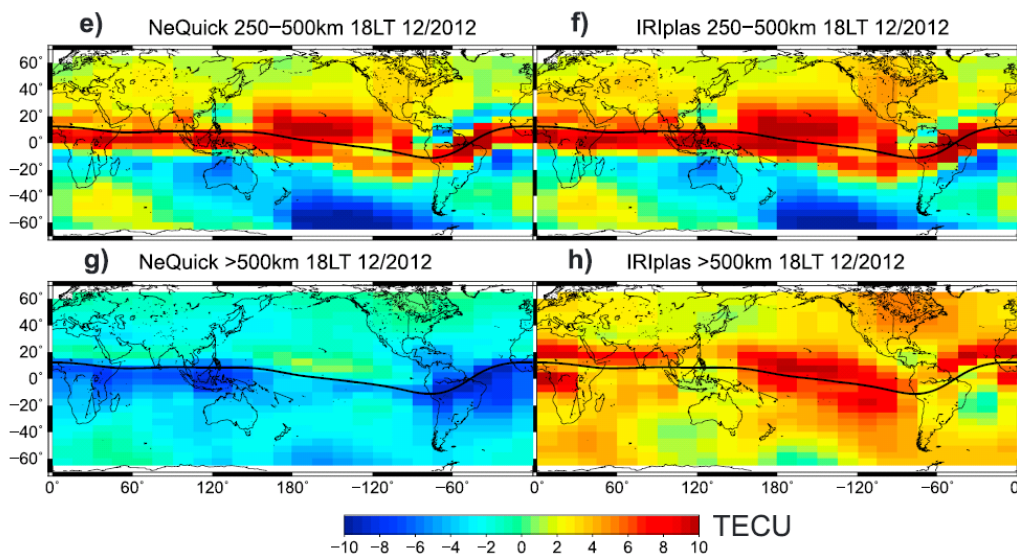


Figure 1. Global maps of differences in the model data in the altitude range of 250–500 km and above 500 km for the December 2009 solstice: results of the NeQuick 2 model (left) and IRI-Plas model (right). One can see that in the altitudinal range of 250–500 km (top panel), both models give similar results with

differences from real observations; at altitudes above 500 km (bottom panel), the NeQuick 2 model underestimates TEC, while the IRI-Plas model provides overestimated TEC values in the topside ionosphere/plasmasphere virtually all over the globe.

*Cherniak, I., & Zakharenkova, I. (2016). NeQuick and IRI-Plas model performance on topside electron content representation: Spaceborne GPS measurements. Radio Science, 51, 752–766.*  
<https://doi.org/10.1002/2015RS005905>

### 2.33. Advantages of the combined use of GPS and GLONASS observations for monitoring the high-latitude ionospheric irregularities

(Russian Academy of Sciences, Pushkov Institute of Terrestrial Magnetism, Ionosphere and Radio Wave Propagation (IZMIRAN))

The occurrence of irregularities in the high-latitude ionospheric plasma density during the geomagnetic storm of June 22–23, 2015 was studied using a representative database of ~5800 worldwide ground-based GNSS stations. For the first time, high-resolution two-dimensional maps of ROTI (Rate of TEC changes Index) used as an indicator of the presence and intensity of ionospheric irregularities were constructed on the basis of both GPS and GLONASS measurements. It was demonstrated that additional use of GLONASS observations when monitoring ionospheric irregularities increases significantly the data coverage over the regions with sparse distribution of GNSS stations (Northern Canada, Russia, Antarctic). In the regions with high data coverage (USA, Europe) the use of GLONASS increases the number of observations available by 1.5-2 times.

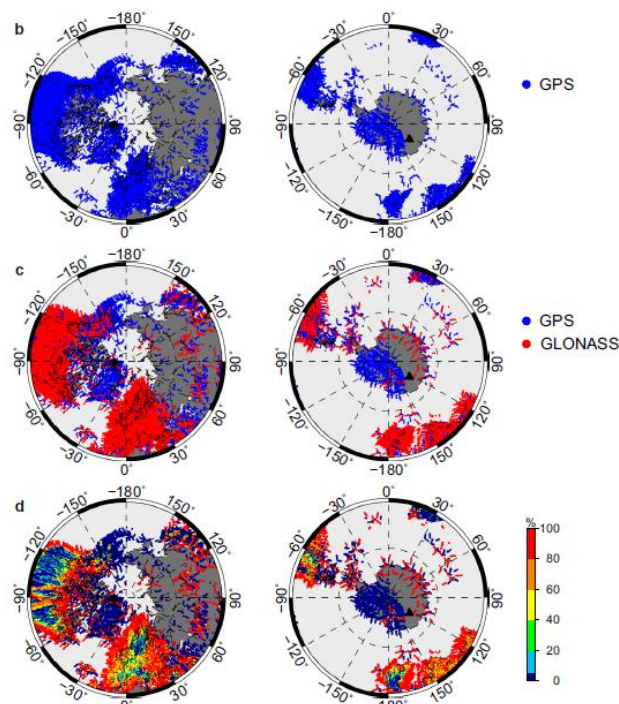




Figure 1. Example of data coverage over the North and South Hemispheres in the latitude range of 30°-90° during 1 hour: (b) GPS observations alone; (c) combined GPS and GLONASS observations; (d) percentage contribution of GLONASS data to each 1° cell.

*Cherniak I., Zakharenkova, I. (2017) New advantages of the combined GPS and GLONASS observations for high-latitude ionospheric irregularities monitoring: Case study of June 2015 geomagnetic storm. Earth, Planets and Space, 69:66. doi:10.1186/s40623-017-0652-0*

## RadioAstron Space VLBI Interferometer project: scientific results achieved in 2016-2018

### 2.34. Project description

(Russian Academy of Sciences, Astrospace Centre of Lebedev Physical Institute)

RadioAstron is a space VLBI Mission aimed at achieving the highest angular resolution of radio observations at centimeter wavelengths through ground-space interferometric measurements on baselines of up to  $\sim 360,000$  km. The Mission consists of a 10-metre space-borne radio telescope (SRT), Spektr-R, operating at wavelengths of 92, 18, 6.2, and 1.2–1.6 cm and supported by a range of ground-based facilities.

The basic parameters of the SRT and RadioAstron observations are summarized in Table 1. RadioAstron provides observations of radio sources at ultra-high angular resolution, with ground-space baselines of up to 360,000 km reaching a resolution of about 7 microarcseconds at the wavelength of 1.3 cm. These observations enable accurate measurements of structural properties and evolution on sub-milliarcsecond scales in galactic and extragalactic radio sources. At intermediate baselines, high quality imaging of radio sources with moderate resolution can be obtained for objects located near the orbital plane or observed near perigee passages of the satellite.

**Table 1**

Observing bands (cm)	Frequency range (MHz)	Smallest spacing (uas)	SEFD (kJy) LCPRCP		Baseline Sensitivity (mJy)
92 (P)	316–332	530	13.3	13.5	14
18 (L)	1636–1692	100	2.76	2.93	3
6.2 (C)	4804–4860	35	11.6	–	5
1.2 – 1.6 (K)	18372–25132	7	46.7	36.8	16

*K-band observing can be done at one of the eight central frequencies: 18392, 19352, 20312, 21272, 22232, 23192, 24152, 25112 MHz. The fringe spacing is calculated for the longest possible baseline. The one-sigma baseline sensitivity is estimated for the RadioAstron-GBT pair for a 300 s integration time and 16 MHz bandwidth of a single polarization, single frequency channel (IF).*

The *RadioAstron* project is led by the Astro Space Center of the Lebedev Physical Institute of the Russian Academy of Sciences and the Lavochkin Scientific and Production Association under a contract with the State Space Corporation ROSCOSMOS, in collaboration with partner organizations in Russia and other countries. Orbit determination measurements and analysis are performed by the Ballistics Group at the Keldysh Institute of Applied Mathematics (KIAM) in Moscow. Data from the SRT are received at the Pushchino Tracking Station operated by the ASC or the Green Bank Tracking Station operated by NRAO. The data from the SRT are recorded in the *RadioAstron* Data Format (RDF) specially developed for the Mission operations. Data correlation from *RadioAstron* observations is conducted primarily at the RadioAstron Correlator Facility designed and operated at the Data Processing Department of the ASC. The MPIR-DiFX software correlator and the EVN software correlator at JIVE (SFXC) are also being used to correlate RadioAstron experiments. Block time commitments to RadioAstron observations are being organized or considered at many ground radio telescope (GRT) facilities.

Scientific operations of the RadioAstron Mission are conducted by the ASC and the radio interferometric networks. The RadioAstron International Science Council (RISC), which is comprised of representatives from the ASC, major GRT facilities, and the radio astronomical community, provides overall policy definitions for the Mission, and discusses scientific issues and priorities.

There are a number of different ground facilities participating in operation, tracking, data transfer and observations with the radio antenna on board Spektr-R. These include the Flight Control Center (FCC) at the Lavochkin Association; the Deep Space Network Communication (DSNC) antennas in Ussurijsk and Bear Lakes employed for the uplink and telemetry communications with the satellite; the Satellite Tracking Station (STS) in Pushchino, Russia, and Green Bank, USA, used for telemetry and data acquisition from the Spektr-R satellite; the laser ranging stations (LRS) used for orbit determination measurements; and the ground radio telescopes (GRTs) taking part in Very Long Baseline Interferometry (VLBI) observations with the Spektr-R antenna (hereafter, RadioAstron observations). VLBI methods are being utilized to determine the spacecraft state vector for orbit reconstruction.

The scientific program of RadioAstron consists of three major parts: the Early Science Program (ESP), Key Science Program (KSP), and General Observing Time (GOT) projects. The Early Science Program, which finished in June 2013, explored the main scientific capabilities of RadioAstron observations and paved the way for the subsequent KSP and GOT programs. RadioAstron KSP observations commenced in July 2013. The KSP is aimed specifically at focusing

on the areas of strongest scientific impact of RadioAstron and ensuring a long-lasting scientific impact for the Mission.

In the years 2016–2018 the RadioAstron mission carried out scientific programs under the AO-4 and AO-5 Announcement of Opportunity cycles.

These cycles consist of 25 scientific projects selected by RadioAstron Program Evaluation Committee (RPEC) on a competitive basis.

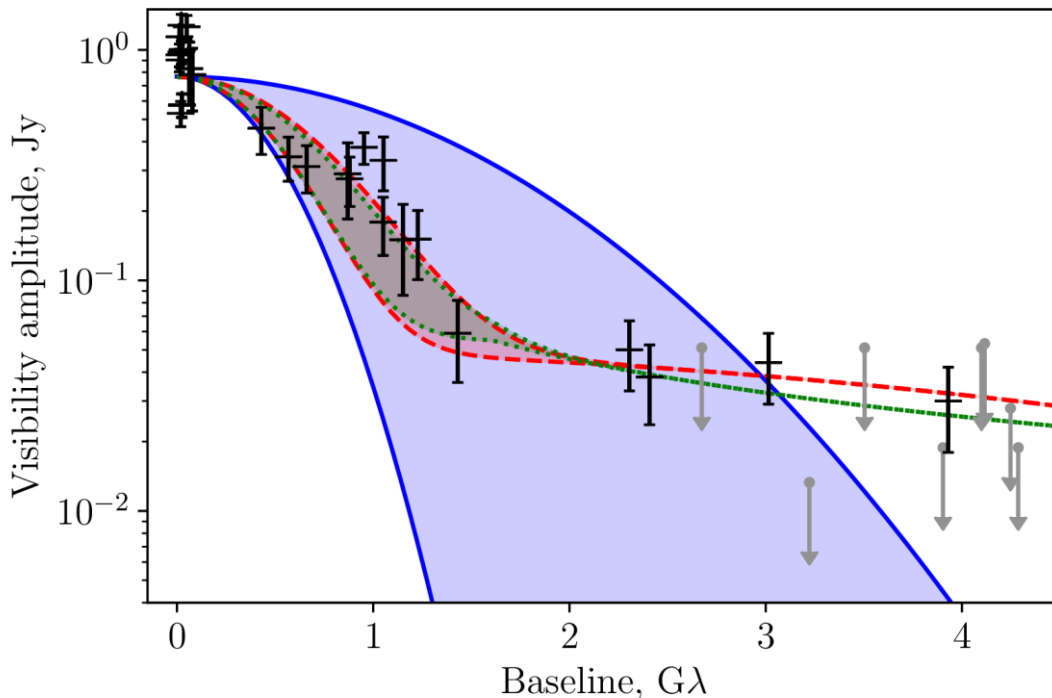
Scientists from about twenty countries took part in these investigations. Below we present selected scientific results obtained and published in the period 2016–2018. The full list of RadioAstron publications can be found at <http://www.asc.rssi.ru/radioastron/publications/publ.html>

## AGN studies

### 2.35. The high brightness temperature of B0529+483 revealed by RadioAstron and implications for interstellar scattering

(Russian Academy of Sciences, Astrospace Centre of Lebedev Physical Institute)

The high brightness temperatures,  $T_b > 10^{13}$  K, detected in several active galactic nuclei by *RadioAstron* space VLBI observations challenge theoretical limits. Refractive scattering by the interstellar medium may affect such measurements. We quantify the scattering properties and the sub-mas scale source parameters for the quasar B0529+483. Using *RadioAstron* correlated flux density measurements



at 1.7, 4.8, and 22 GHz on projected baselines up to 240 000 km we find two characteristic angular scales in the quasar core, about 100 and 10  $\mu$ as. Some indications of scattering substructure are found. Very high brightness temperatures,  $T_b > 10^{13}$  K, are estimated at 4.8 and 22 GHz even taking into account the

refractive scattering. Our findings suggest a clear dominance of the particle energy density over the magnetic field energy density in the core of this quasar.

**Figure 1.** The visibility amplitude as a function of baseline length at 4.8 GHz. Error bars represent RadioAstron data, blue shaded region between solid lines – single elliptical Gaussian model, red region between dashed lines – double Gaussian model, green region between dotted lines – model with refractive substructure. Borders of the shaded regions correspond to minor and major axes of the model, the regions itself cover visibility amplitude values for various position angles.

### 2.36. The extreme blazar AO 0235+164 as seen by extensive ground and space radio observations

(Russian Academy of Sciences, Astrospace Centre of Lebedev Physical Institute)

Clues to the physical conditions in radio cores of blazars come from measurements of brightness temperatures as well as effects produced by intrinsic opacity. We study the properties of the ultra-compact blazar AO 0235+164 with the RadioAstron ground-space radio interferometer, multifrequency VLBA, EVN, and single-dish radio observations. We employ visibility modelling and image stacking for deriving structure and kinematics of the source, and use Gaussian process regression to find the relative multiband time delays of the flares. The multifrequency core size and time lags support prevailing synchrotron self-absorption. The intrinsic brightness temperature of the core derived from ground-based very long baseline interferometry (VLBI) is close to the equipartition regime value. In the same time, there is evidence for ultra-compact features of the size of less than  $10 \mu\text{as}$  in the source, which might be responsible for the extreme apparent brightness temperatures of up to  $10^{14}$  K as measured by RadioAstron. In 2007 – 2016 the VLBI components in the source at 43 GHz are found predominantly in two directions, suggesting a bend of the outflow from southern to northern direction. The apparent opening angle of the jet seen in the stacked image at 43 GHz is two times wider than that at 15 GHz, indicating a collimation of the flow within the central 1.5 mas. We estimate the Lorentz factor  $\Gamma = 14$ , the Doppler factor  $\delta = 21$ , and the viewing angle  $\theta = 1.7$  of the apparent jet base, derive the gradients of magnetic field strength and electron density in the outflow, and the distance between jet apex and the core at each frequency.

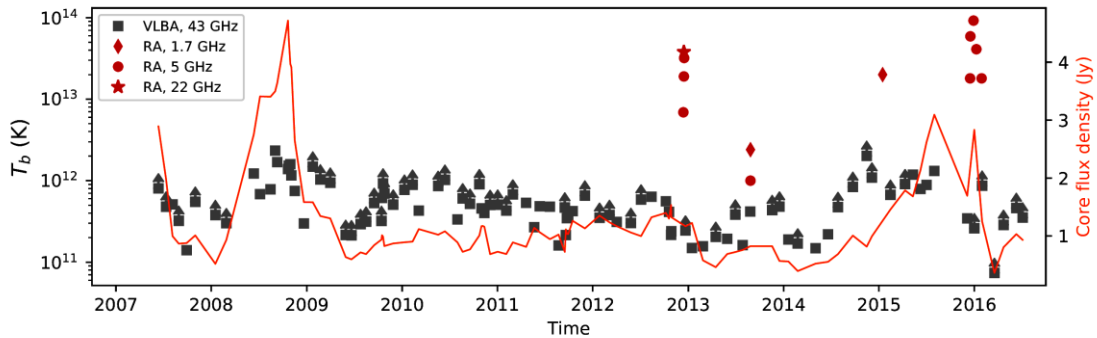


**Figure 2.** The apparent brightness temperature by VLBA at 43 GHz and RadioAstron at 1.7, 5 and 22 GHz. Arrows mark  $T_b$  estimated using the resolution limits. The curve shows core flux density at 43 GHz (right axis).

### 2.37. Probing the innermost regions of AGN jets and their magnetic fields with RadioAstron: Observations of 3C 273 at minimum activity

(Russian Academy of Sciences, AstropSpace Centre of Lebedev Physical Institute)

The RadioAstron active galactic nuclei (AGN) polarization Key Science Project (KSP) aims at exploiting the unprecedented angular resolution provided by RadioAstron to study jet launching/collimation and magnetic-field configuration in AGN jets. The targets of our KSP are some of the most powerful blazars in the sky. We present observations at 22 GHz of 3C 273, performed in 2014, designed to reach a maximum baseline of approximately nine Earth diameters. Reaching an angular resolution of 0.3 mas, we study a particularly low-activity state of the source, and estimate the nuclear region brightness temperature, comparing with the extreme one detected one year before during the RadioAstron early science period. We also make use of the VLBA-BU-BLAZAR survey data, at 43 GHz, to study the kinematics of the jet in a 1.5-yr time window.

We find that the nuclear brightness temperature is two orders of magnitude lower than the exceptionally high value detected in 2013 with RadioAstron at the same frequency ( $1.4 \times 10^{13}$  K, source-frame), and even one order of magnitude lower than the equipartition value. The kinematics analysis at 43 GHz shows that a new component was ejected 2 months after the 2013 epoch, visible also in our 22 GHz map presented here. Consequently this was located upstream of the core during the brightness temperature peak. Fermi-LAT observations for the period 2010 – 2014 do not show any gamma-ray flare in conjunction with the passage of the new component through the core at 43 GHz.

These observations confirm that the previously detected extreme brightness temperature in 3C 273, exceeding the inverse Compton limit, is a short-lived phenomenon caused by a temporary departure from equipartition.

Thus, the availability of interferometric baselines capable of providing as angular resolution does not systematically imply measured brightness temperatures over the known physical limits for astrophysical sources.

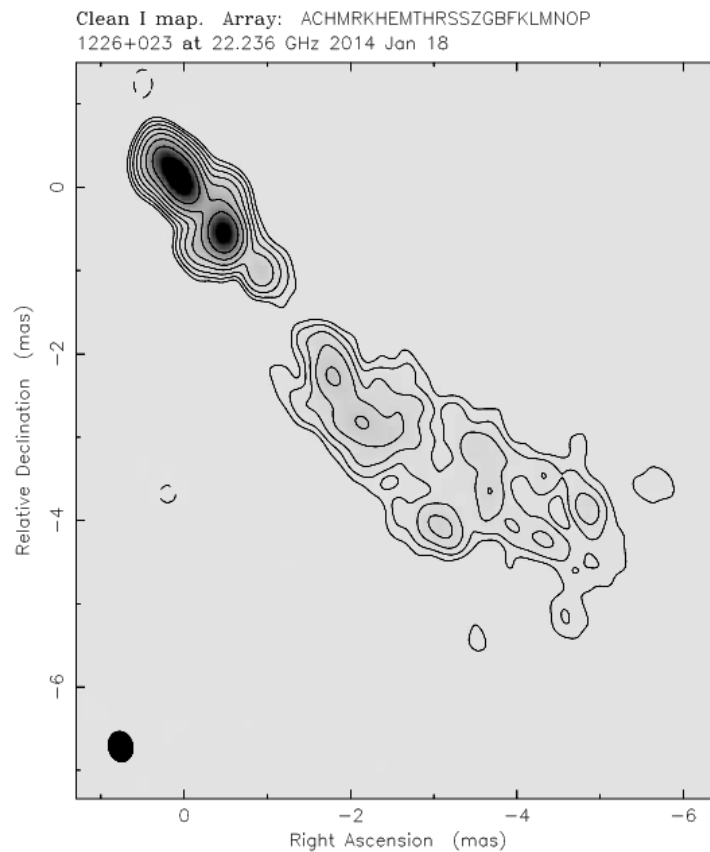


**Figure 3.** Map of 3C 273 at 22 GHz obtained with the global ground array plus RadioAstron, using uniform weighting. The lowest contour significance is 5-sigma.

### 2.38. RadioAstron image of NGC 1275 reveals a wide and collimated jet structure on the scale of a few hundred gravitational radii

(Russian Academy of Sciences, Astrospace Centre of Lebedev Physical Institute)

The RadioAstron Nearby AGN Key Science Program has published its first results in *Nature Astronomy* (Giovannini et al. 2018). A 22 GHz space-VLBI image of the recently restarted parsec scale jet in 3C 84, a radio source located in the giant elliptical galaxy NGC 1275 in the Perseus Cluster, transversely resolves the strongly edge-brightened young jet just 30 microarcseconds from the core – ten times closer to the central engine than in the previous ground-based studies. This corresponds to a de-projected linear distance of just a few hundred gravitational radii. Being able to resolve the jet and measure its collimation profile inside the acceleration region is important for testing the current jet formation models.

It was found that the jet in 3C 84 is surprisingly wide (Fig. 8), with a transverse radius greater than 250 gravitational radii. This implies that either the bright outer layer rapidly expands closer to the black hole or that this “sheath” is launched from the accretion disk.

Another major result of the paper is that the previously found, almost cylindrical collimation profile on the scales larger a few thousand gravitational radii extends down to a scale of a few hundred gravitational radii. It indicates a flat density profile of the external confining medium. The authors propose that the recently restarted jet in 3C84 is shaped by shocked material of a cocoon forming around the jet – just like the kiloparsec scale jets are recollimated in a cylindrical shape before they enter the leading hot spot.

The observations were made during a perigee passage in September 2013. In addition to Space Radio Telescope, more than two dozen ground radio telescopes, including the European VLBI Network together with the Russian Kvazar network, the Korean VLBI Network, Kalyazin and the NRAO telescopes Very Long Baseline Array, the Green Bank Telescope, and the phased Very Large Array, participated in the experiment.

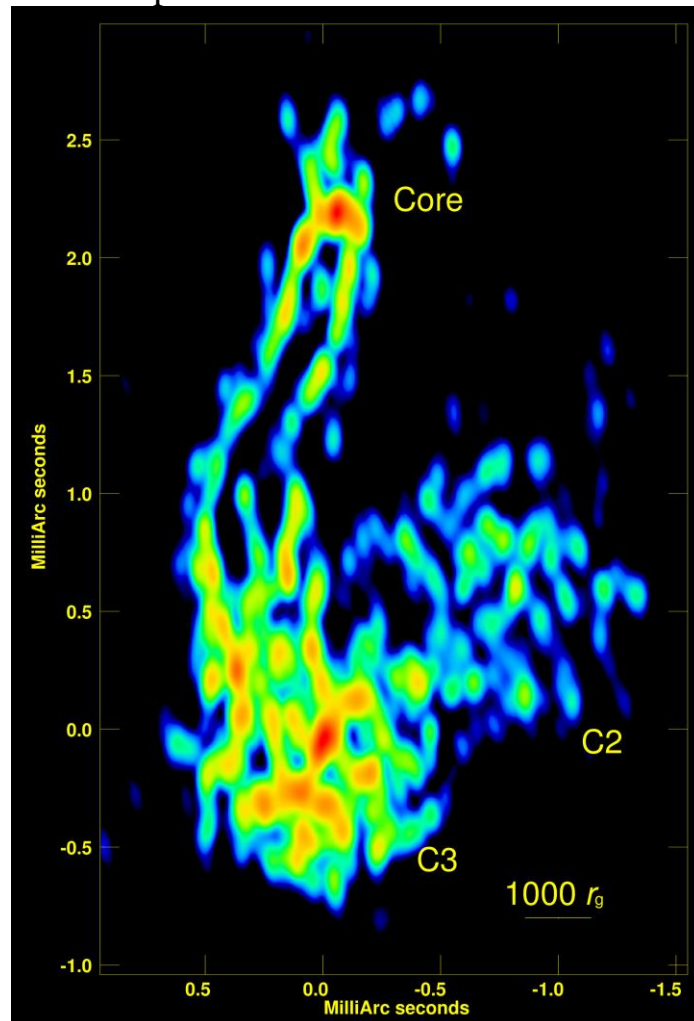


**Figure 4.** Radio image of the central parsec in 3C84 obtained with RadioAstron at 1.3 cm.

## **RadioAstron study of galactic and extragalactic water masers**

### **2.39. H<sub>2</sub>O MegaMaser in NGC4258**

(Russian Academy of Sciences, Astrospace Centre of Lebedev Physical Institute)

The H<sub>2</sub>O MegaMaser emission regions in NGC 4258 are confined to a nearly edge-on disk of 0.5 pc surrounding the nuclear AGN (Herrnstein et al. 1998), also qualified as a CSO. The orbiting molecular regions within the disk drift in front of the southern part of the CSO radio continuum and amplify this continuum. Because of the orbital motion in the disk, the maser components drift across the spectrum from low velocity to high, at approximately 8.1 km/s/yr across the velocity range 440 – 550 km/s (Haschick, Baan and Peng 1994, Humphreys et al. 2008). The systemic velocity of NGC 4258 is 472 km/s at a distance of (approximately) 7 Mpc.

At the time of this writing, the H<sub>2</sub>O mega-maser emission in NGC 4258 has been detected with 11 RadioAstron experiments, the first dating back to 2014. While fringes were initially found in observational data at a baseline of 1.9 Earth diameters (ED), the updated orbital model of the SRT at the ASC correlator resulted in subsequent detection of fringes up to baselines of 26.7 ED (corresponding to 340,000 km). The detection of fringes of the H<sub>2</sub>O mega-maser emission on this long SRT-GBT baseline constitutes an absolute record of 8  $\mu$ s in angular resolution.

At higher resolution an increasing part of the diffuse maser components in NGC 4258 will be resolved, and only more compact components will remain unresolved. This is evident in the fringe amplitude plot of the detection with the 26.7 Earth diameter SRT-Medicina baseline displayed in Figure 5. Several individual components may be identified with a spatial resolution of  $\sim$ 56 AU at the distance of NGC 4258. The mere detection of such compact maser components in NGC 4258 provides stringent limits on the degree of saturation and the excitation process. In addition, these more compact masering regions are likely to have less tangled magnetic fields and may allow detection of the magnetic field strength by its polarization properties.



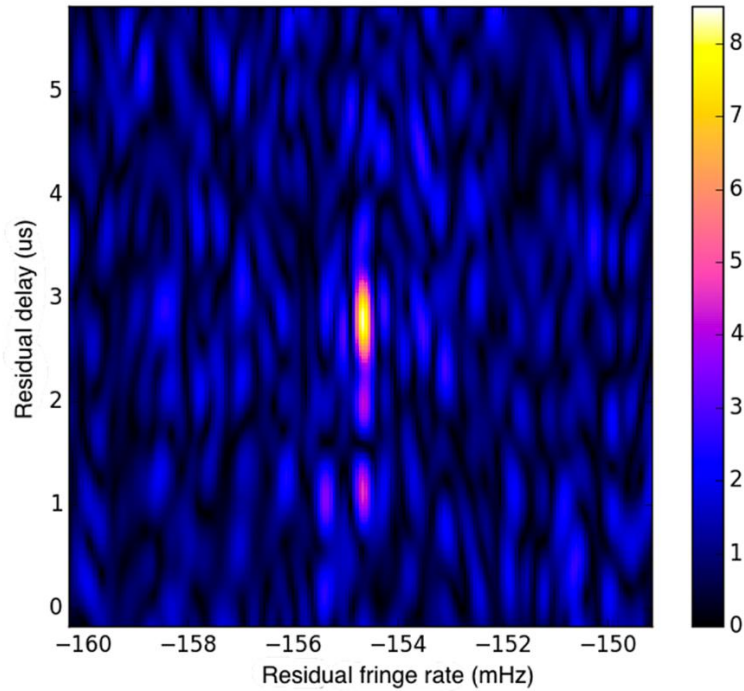


**Figure 5.** The fringe amplitude plot of the SRT-Medicina detection of NGC 4258 at 26.7 Earth diameters. The ratio of the interferometer fringe amplitude to the average noise amplitude is plotted against residual delay and fringe rate.

#### 2.40. Sun-sized Water Vapor Masers in Cepheus A

(Russian Academy of Sciences, Astrospace Centre of Lebedev Physical Institute)

VLBI observations of a Galactic water maser (in Cepheus A) made with a very long baseline interferometric array involving the RadioAstron Earth-orbiting satellite station as one of its elements. Two distinct components at  $-16.9$  and  $0.6$  km/s were detected with a fringe spacing of  $66 \mu\text{as}$ . In total power, the  $0.6$  km/s component appears to be a single Gaussian component of strength  $580$  Jy and width of  $0.7$  km/s. Single-telescope monitoring showed that its lifetime was only eight months. The absence of a Zeeman pattern implies the longitudinal magnetic field component is weaker than  $120$  mG. The space–Earth cross power spectrum shows two unresolved components smaller than  $15 \mu\text{as}$ , corresponding to a linear scale of  $1.6 \times 10^{11}$  cm, about the diameter of the Sun, for a distance of  $700$  pc, separated by  $0.54$  km/s in velocity and by  $160 \pm 35 \mu\text{as}$  in angle. This is the smallest structure ever observed in a Galactic maser. The brightness temperatures are greater than  $2 \times 10^{14}$  K, and the line widths are  $0.5$  km/s. Most of the flux (about 87%) is contained in a halo of angular size of  $400 \pm 150 \mu\text{as}$ . This structure is associated with the compact H II region HW3diii. We have probably picked up the most prominent peaks in the angular size range of our interferometer. We discuss three dynamical models: (1) Keplerian motion around a central object, (2) two chance overlapping clouds, and (3) vortices caused by flow around an obstacle (i.e., von Kármán vortex street) with a Strouhal number

of about 0.3. The observed structure most likely can be explained in the model of turbulent vortices shed by an obstacle in a flow.

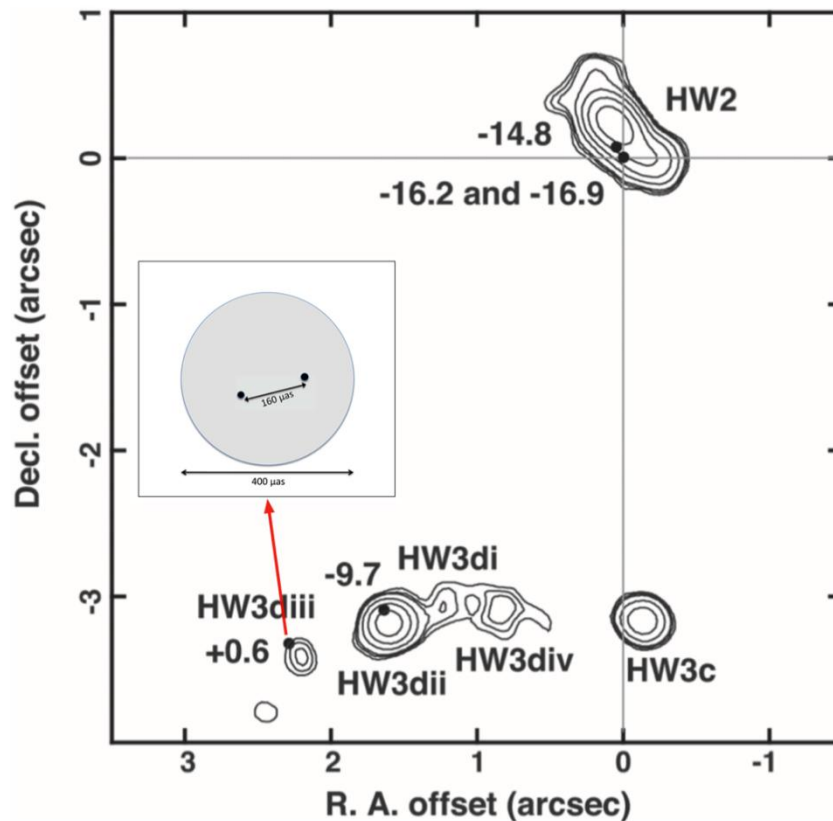


**Figure 6:** The central part of the star-forming region Cepheus A. The contours show the extent of the continuum components taken from the 1.3 cm VLA image (adapted from Torrelles et al. 1998). The dots mark the positions of masers labeled by their velocities. Inset: a cartoon of the maser emission from the 0.6 km/s feature which show two sub-components separated by 160  $\mu\text{s}$ . They are aligned with the axis of the outflow from Hd3ii.

#### 2.41. Thin Spatial Structure of the H<sub>2</sub>O maser in the Globule IC 1396 N (Russian Academy of Sciences, AstropSpace Centre of Lebedev Physical Institute)

The globule IC 1396 N, located at a distance of 750 pc, was chosen for investigation at the ultrahigh resolution with RadioAstron. In this region, the active formation of intermediate-mass stars is observed, and several young stellar objects and molecular outflows are detected. In the direction of the brightest young stellar object IRAS 21391+5802 (460L<sub>O</sub>), the strong H<sub>2</sub>O maser is observed, the monitoring of which has been carried out for more than 20 years.

In 2014, five observations of IC 1396 N were performed with the RadioAstron space telescope and a network of ground telescopes from several countries.

The source was not detected on the ground-space baselines. This set the lower limit on the maser spot size  $> 0.3$  AU, and the upper limit of brightness temperature of  $6.25 \times 10^{12}$  K.

A regular structure which was observed in 1996 and previously was interpreted as a Keplerian disk (Slysh et al., 1999) also have been detected in ground-based baselines in 2014, but has a smaller flux. In other words, after 18 years, the spatial

maser structure, which is matched by the central spectrum part with the velocity spacing of nearly 1.5 km/s, is sustained on the scale of less than 20 mas, which at a distance of 750 pc, corresponds to a linear size of about 15 AU.

#### **2.42. Study of H<sub>2</sub>O maser bursts in high-mass star formation regions with ultimate angular resolution.**

(Russian Academy of Sciences, Astrospace Centre of Lebedev Physical Institute)

Successful detection of interferometric fringes from very compact water maser feature associated with the flaring maser in high-mass star-forming region G25.65+1.05 is reported.

Maser emission has been successfully detected in two RadioAstron sessions, carried out on August and September 2017 with the VLBA (USA), Torun (Poland), Hartebeesthoek (South Africa) telescopes on the ground. The projected baseline length reached 9.3 Earth diameters, corresponding to an angular resolution of  $\sim 24 \mu\text{as}$  or a linear size for the emitting region of about 0.05 AU assuming a source distance of 2.08 kpc.

This nearly repeats the record of the angular resolution obtained earlier in observations of another water maser in W49N.

### **Pulsar studies**

#### **2.43. Giant Pulses of the Crab Nebula Pulsar as an Indicator of a Strong Electromagnetic Wave**

(Russian Academy of Sciences, Astrospace Centre of Lebedev Physical Institute)

The observed quasi-regular visibility functions of individual giant pulses indicate the presence of strong, unresolved components in the structure of these pulses at 1668 MHz. Similar components were observed earlier only at frequencies above 5 GHz, in the frequency range where they are not blurred by scattering. Thus, VLBI observations of giant pulses from the Crab Nebula pulsar indicate the presence of fine structure in the pulses at 1668 MHz – unresolved peaks with duration  $\tau \leq 30 \text{ ns}$  and brightness temperature  $T_b \geq 10^{39} \text{ K}$ . Thus, we concluded that unresolved components with such high brightness temperatures shall propagate as strong electromagnetic waves that accelerate particles in the ambient plasma. This gives rise to new components in the pulsar pulse profile (HFC1, HFC2) at frequencies above 4 GHz.

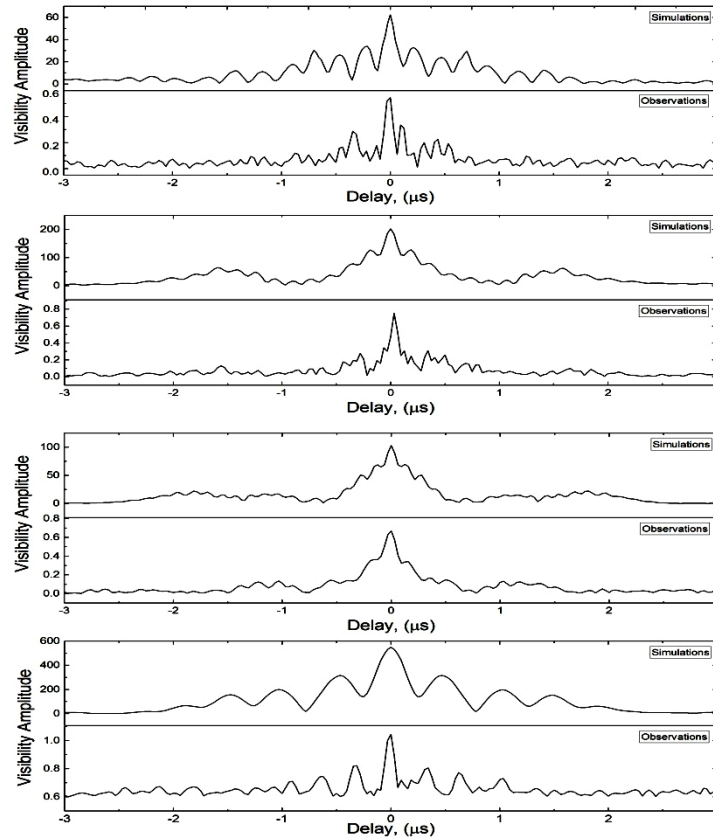


**Figure 7.** Examples of visibility functions obtained in observations (lower part of every figure), and in our simulation (upper part). They prove that giant pulses contain super compact components.

#### **2.44. Distribution of Interstellar Plasma in the Direction of PSR B0525+21 from Data Obtained on a Ground-space Interferometer**

(Russian Academy of Sciences, Astrospace Centre of Lebedev Physical Institute)

Observations on the RadioAstron ground-space interferometer with the participation of the Green Bank and Arecibo ground telescopes at 1668 MHz have enabled studies of the characteristics of the interstellar plasma in the direction of the pulsar PSR B0525+21. The maximum projected baseline for the ground-space interferometer was 233 600 km. The scintillations in these observations were strong, and the spectrum of inhomogeneties in the interstellar plasma was a power law with index  $n = 3.74$ , corresponding to a Kolmogorov spectrum. A new method for estimating the size of the scattering disk was applied to estimate the scattering angle (scattering disk radius) in the direction toward PSR B0525+21,  $\theta_{\text{scat}} = 0.028 \pm 0.002$  milliarcsecond. The scattering in this direction occurs in a plasma layer located at a distance of  $0.1 Z$  from the pulsar, where  $Z$  is the distance from the pulsar to the observer. For the adopted distance  $Z = 1.6$  kpc, the screen is located at a distance of 1.44 kpc from the observer.

## 2.45. Revealing compact structures of interstellar plasma in the Galaxy with RadioAstron

(Russian Academy of Sciences, Astrospace Centre of Lebedev Physical Institute)

We have observed five pulsars with RadioAstron ground-space radio interferometer and measured angular sizes of scattering disks. In order to determine the location of the scattering region we used thin screen model. That model was proposed right after the discovery of pulsars (Scheuer 1968; Rickett 1977, 1990) and despite its simplicity it sufficiently describes the results of our observations. The uniform model of scattering medium distribution along the line of sight can not be reconciled with the experimental data of the observed pulsars. Therefore the observational evidence favours the conclusion that the scattering is mainly produced by relatively compact plasma layers.

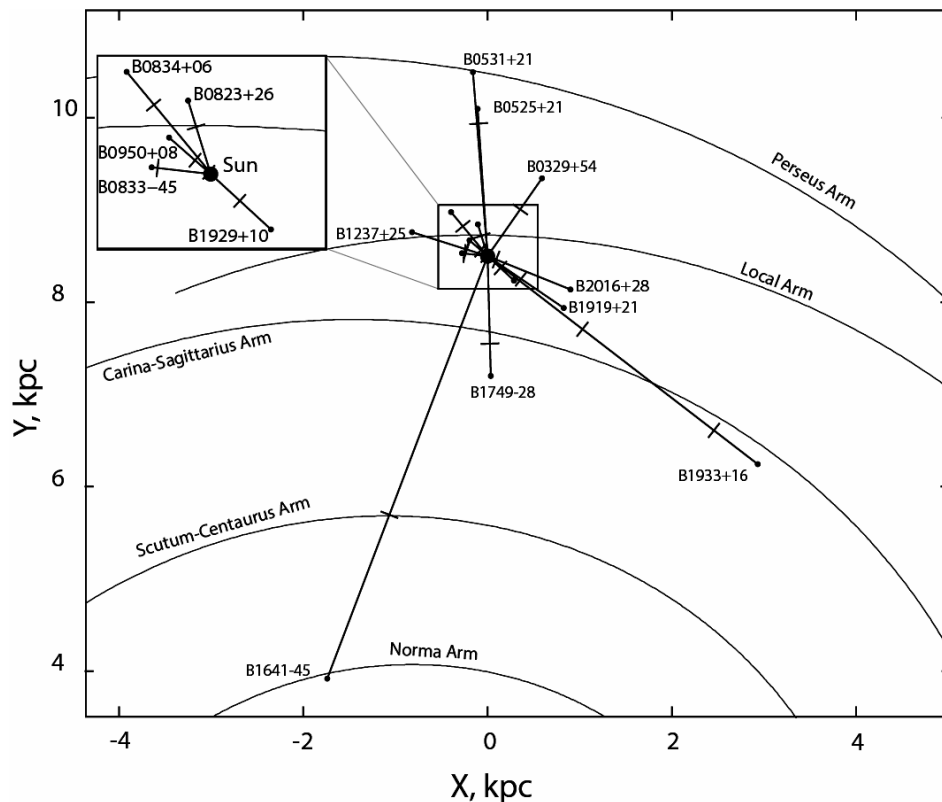


**Figure 8.** Location of pulsars and detected scattering screens relative to the spiral arms of the Galaxy. The position of screens are indicated by the short bars along the line connected every pulsar

## 2.46. Testing Einstein's general relativity

(Russian Academy of Sciences, Astrospace Centre of Lebedev Physical Institute)

The RadioAstron Key Science Program on the gravitational redshift experiment has completed its data collection stage. The observations for the experiment were supported by EVN, NRAO, and several geodetic radio telescopes (Badary –

Russia, Effelsberg – Germany, GBT – USA, Hartebeesthoek – South Africa, Onsala – Sweden, Svetloe – Russia, VLBA – USA, Wettzell – Germany, Yarragadee – Australia, Yebes – Spain, Zelenchukskaya – Russia). The goal of the project is to test Einstein's Equivalence Principle – the basis of general relativity. Specifically, the team aims to verify Einstein's formula for the gravitational redshift effect or, equivalently, the gravitational time dilation due to a nearby massive body. For the RadioAstron spacecraft the effect due to the Earth is about -58 microseconds per day relative to an observer at the Earth's surface – time actually flows faster aboard the spacecraft hence the minus sign. The most accurate test of this kind to date was performed in 1976 by the NASA-SAO Gravity Probe A mission. That experiment proved the validity of Einstein's formula with an accuracy of about 0.01% using a suborbital probe equipped with a hydrogen maser frequency standard. The experiment with RadioAstron is based on a similar approach but benefitted from a better performing hydrogen maser and a favorable highly eccentric orbit, which allowed the team to perform their measurements multiple times. All this, coupled with an evaluation of the quality of the collected data, make the team believe they'll be able to supersede the result of their renowned predecessor by an order of magnitude. This anticipated result will mark an important milestone in our challenge to find the level at which general relativity breaks down and a more general theory, such as string theory, is beginning to reveal its subtle features. The team have recently published a paper, presenting their techniques and giving a status update of the experiment. Figure 9 illustrates the results of preliminary data processing of one of the experiments. While the data processing is far from finished, the currently achieved accuracy is already at the level of that of Gravity Probe A.

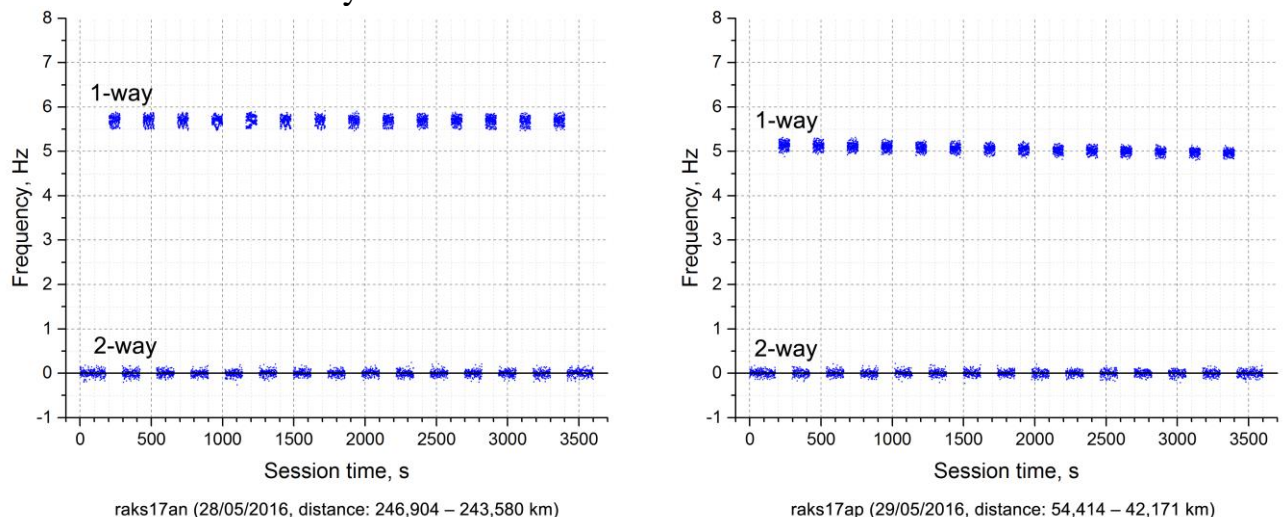


**Figure 9.** Results of the data processing of an experiment performed in May 2016. The experiment consisted of three observations at greatly varying distances, each  $\sim 1$  hour long, supported by the Effelsberg, Onsala, Svetloe, Wettzell (Wz and Wn) telescopes. The two panes of the figure depict the residual frequencies of the 1- and 2-way 8.4 GHz downlink signals from the RadioAstron spacecraft measured with the Onsala 20-m telescope, for the two outermost observations. The 1-way signal contains the useful gravitational redshift, while the 2-way signal is used to suppress the contribution of the nonrelativistic Doppler shift. The observations were

performed using the interleaved measurements approach, with a switching cycle of 4 min. The 1-way frequency residuals are not corrected for the gravitational redshift. This makes the variation of the gravitational redshift between the two outermost observations clearly visible (varying from 5.69 Hz to 4.96 Hz).

#### **2.47. Ballistics-navigation support of the spacecraft flight control and implementation of «Radioastron» project scientific program.**

(Russian Academy of Sciences, Keldysh Institute for Applied Mathematics)

The ballistic-navigation support for «Radioastron» program is performing. In the frame of this program the space radio telescope accommodated onboard of «SPEKTR-R» spacecraft jointly with ground radio telescopes allow observations of radio sources with very high angular resolution. Issues of performance of ground trajectory measurements, navigation support of flight control, scientific experiments support as well as correction of motion trajectories are considered.

The correction of the trajectory of spacecraft "Spectrum-R" SC was calculated and successfully realized. Correction ensured the fulfillment of the required conditions for the time of ballistic existence and illumination of the Sun by the spacecraft over the end of 2019.

The ballistic-navigation support for «Radioastron» program for the space radio telescope accommodated onboard of «SPEKTR-R» spacecraft jointly with ground radio telescopes allow observations of radio sources with very high angular resolution. The space radio telescope installed aboard the "Spektr-R" spacecraft is an element of a terrestrial-space interferometer rendered relative to terrestrial radio telescopes for a distance which limited by the spacecraft's apogee 300,000 km. This allows to achieve a high resolution of the observed objects. The processing of data obtained by the terrestrial-space interferometer is impossible without precise parameters determination of the "Spectr-R" orbit. The restoration of the parameters of the motion of the "Spectr-R" spacecraft with the accuracy necessary for the processing of scientific information, according to trajectory measurements, is a difficult task. Its complexity, including that due to the fact that during the daily sessions of unloading flywheel engines, perturbations of the motion of the center of mass arise. To restore the motion parameters of the "Spectr-R" spacecraft, a special technique has been developed and realised for simultaneous processing of trajectory measurements and data on the inclusion of engines coming into telemetry.

Spektr-R's tracking was to be handled by the RT-22 radio telescope in Pushchino, Russia. Flight control would be operated by ground stations in MedvezhiOzera, near Moscow, and Ussuriysk in Russia's Far East, measurements of laser ranging stations, as well as non-query radial velocity measurements in the X-band realized in VIRK-stations in Puchino and Green Bank.

This allowed the navigation support of the international research program to be successfully carried out by a ground-space interferometer: to perform measurements of interferometric responses from two pulsars and several

extragalactic sources with a record angular resolution. The results of the refinement of the parameters of the "Spektr-R" spacecraft trajectory made in 2016 showed that with a probability close to unity, in January 2018 the condition of its stay in the shadow of the Earth is violated, and in May of the same year its ballistic existence. The correction of the trajectory of spacecraft "Spectrum-R" SC was calculated and successfully realized in 16 July 2016. Correction ensured the fulfillment of the required conditions for the time of ballistic existence and illumination of the Sun by the spacecraft over the end of 2019.

Performed results are displayed in publications

1. Zaslavskii, G.S., Zakhvatkin, M.V., Kardashev, N.S., Stepan'yants, V.A., Tuchin, A.G., e.a. Ballistics-navigation support of the spacecraft flight control and implementation of «Radioastron» project scientific program. 5 yearsofflight// VestnikNPO im. S.A. Lavochkina. 2016, v.33. №3. pp. 25-37.
2. Zaslavskii, G.S., Zakhvatkin, M.V., Kardashev, N.S., Stepan'yants, V.A., Tuchin, A.G.,e.a. Designing corrections for the trajectory of the Spektr-R spacecraft in the event of immersions into the Moon's sphere of influence // Cosmic Research. 2017. v. 55, № 4. pp. 305-320.